独立行政法人港湾空港技術研究所

港湾空港技術研究所報告

REPORT OF
THE PORT AND AIRPORT RESEARCH
INSTITUTE

港湾空港技術研究所報告 (REPORT OF PARI)

第 47 巻　第 1 号 (Vol. 47,　No.1),　2008 年 3 月 (March 2008)

目　　　次 (CONTENTS)

Stability of Group Column Type DM Improved Ground under Embankment Loading Behavior of Sheet Pile Quay Wall

Masaki KITAZUME *

Synopsis

The Deep Mixing Method (DMM), a deep in-situ soil stabilization technique using cement and/or lime as a binder, has been often applied to improve soft soils. Group column type improvement has been extensively applied to foundations of embankment or lightweight structures. A design procedure for the improved ground has been established in Japan mainly for application of embankment, in which two stability analyses are evaluated: external stability and internal stability. For the external stability, it is known that a collapse failure pattern, in which the DM columns tilt like dominos, could take place instead of a sliding failure when the column strength is relatively high. The current design method, which does not take into account this failure pattern, might overestimate the external stability. For the internal stability, it is found that the DM column shows various failure modes: shear, bending and tensile failure, depending not only on the ground and external loading conditions but also on the location of each column. However, the current design does not incorporate the effect of these failure modes, but only the shear failure mode.

In this study, a series of centrifuge model tests and elasto-plastic FEM analyses were performed to investigate the external and internal stabilities of group column type improved ground under embankment loading. The study revealed that the improved ground does not fail with a sliding failure pattern but rather with a collapse failure pattern in the external stability, and does not fail with a shear failure pattern but rather with a bending failure pattern in the internal stability. Proposed simple calculations incorporating the failure patterns give reasonable estimation of the embankment pressure at ground failure for external and internal stabilities. A parametric study was carried out to investigate the characteristics of the current and the proposed design method.

Key Words: Deep Mixing Method, embankment, stability, failure, centrifuge model, numerical analysis

* Director of Special Research (formerly, Head, Soil Stabilization Division, Geotechnical and Structural Engineering Division) 3-1-1 Nagase,
  Yokosuka, 239-0826 Japan
  Phone : +81-46-844-5055   Fax : +81-46-841-8307   e-mail:kitazume@pari.go.jp

盛土荷重下の杭式深層混合処理地盤の安定性に関する研究

北詰　昌樹*

要　旨

　深層混合処理工法（DMM）は，これまで軟弱地盤の改良に広く適用されてきている。深層混合処理工法による改良パターンの中で，杭式改良地盤は盛土や比較的軽量の構造物の基礎地盤の改良などに用いられている。杭式改良地盤に関する現行設計法では，外部安定および内部安定の検討を行っている。外部安定性の検討においては，個々の杭が一体として支持砂層上面を水平方向に変位する滑動破壊を検討している。一方，内部安定性の検討では，円弧すべり解析によって改良杭自体の安定性を検討している。外部安定性に関して，滑動破壊ではなく改良杭が将棋倒しのように倒れる倒れ込み破壊が生じることが指摘されている。しかし，現行設計法ではこの様な破壊パターンを考慮しておらず，外部安定性に関して過大評価している可能性が高いと思われる。一方，内部安定性の検討では，円弧すべり解析によって改良杭自体の安定性を検討している。しかし，内部安定性に関して，円弧滑りやせん断破壊ではなく改良杭は曲げ破壊が生じることが指摘されている。しかし，現行設計法ではこの様な破壊パターンを考慮しておらず，内部安定性に関しても過大評価している可能性が高いと思われる。

　そこで，本研究では盛土荷重下の杭式改良地盤の外部安定性と内部安定性に着目し，改良地盤の改良幅，改良率および改良杭の強度を変化させた遠心模型実験を行った。特に内部安定性に関する実験では，盛土載荷中の改良杭の破壊時点を特定できるように工夫し，改良杭の破壊と地盤の変形挙動との関係を調べた。実験で得られた改良地盤の破壊パターンを基に簡単な安定計算法を提案し，その妥当性を示すとともに改良地盤の破壊メカニズムについて検討した。さらに，盛土荷重下の杭式改良地盤の安定性に関する数値計算を行い，現行設計法の特性，これまでの研究で得られた破壊モードを考慮した設計法の特性を検討した。

キーワード：深層混合処理工法，盛土，安定性，破壊，遠心模型実験，数値解析

＊　特別研究官（前：地盤・構造部地盤改良研究室長）

〒239-0826　横須賀市長瀬3-1-1　独立行政法人港湾空港技術研究所

　　　電話：046-844-5055　Fax：046-841-8098　　e-mail:kitazume@pari.go.jp

Contents

1. INTRODUCTION

Soft soil deposits are often encountered in construction projects. Accordingly, a large number of soil improvement techniques have been developed in order to provide reinforcement of these soft soil deposits. The Deep Mixing Method (DMM), a deep in-situ soil stabilization technique using cement and/or lime as a binder, which was developed in Japan and in the Nordic countries, has been often applied to improve soft soils (Coastal Development Institute of Technology, 2002). Numerous research efforts have been made to investigate various aspects of the DMM in these countries. Terashi et al. (1979, 1980) and Kawasaki et al. (1981) conducted extensive investigations on the mechanical properties of soil treated with cement or lime and found that the compressive strength of cement treated soil was much higher than that of soft soil; its elastic modulus was also high, usually of the order of several thousands MN/m^2, and the strain at failure has a very small range. In contrast to the compressive strength, the bending and tensile strengths had a relatively small value.

A special deep mixing machine used to treat soft soil in-situ is basically composed of several mixing shafts and blades and a system supplying binder. By one operation, a column shaped treated soil is constructed in the ground. Group column type improvement, where many columns are constructed in rows with rectangular or triangular arrangements, has been extensively applied to foundations of embankment or lightweight structures. A design procedure for the group column type DM improved ground has been established in Japan mainly for application of embankment foundation (Public Work Research Center, 2004). Two stability analyses are evaluated in the design method as shown in **Fig. 1**: external and internal stabilities. In the external stability, the possibility of sliding failure is calculated, in which the DM columns and the clay between move horizontally on a stiff layer without any rearrangement of columns. In the internal stability analysis, rupture breaking failure is calculated by a slip circle analysis, in which the shear failure of DM columns is assumed.

For the external stability, Kitazume et al. (1991 and 2000) performed a series of centrifuge model tests on the stability of a breakwater on a column type DM improved ground reaching a stiff layer, and showed that a collapse failure pattern could take place instead of a sliding failure pattern. In this case, the DM columns tilt like dominos at the bottom, as shown in **Fig. 2(a)**. This means that the collapse failure pattern is less stable than the sliding failure pattern. The current design method, which does not take into account this failure pattern, might overestimate the external stability. Kitazume and Maruyama (2005 and 2006) performed another series of centrifuge model tests and proposed a design method on external stability by incorporating the collapse failure pattern.
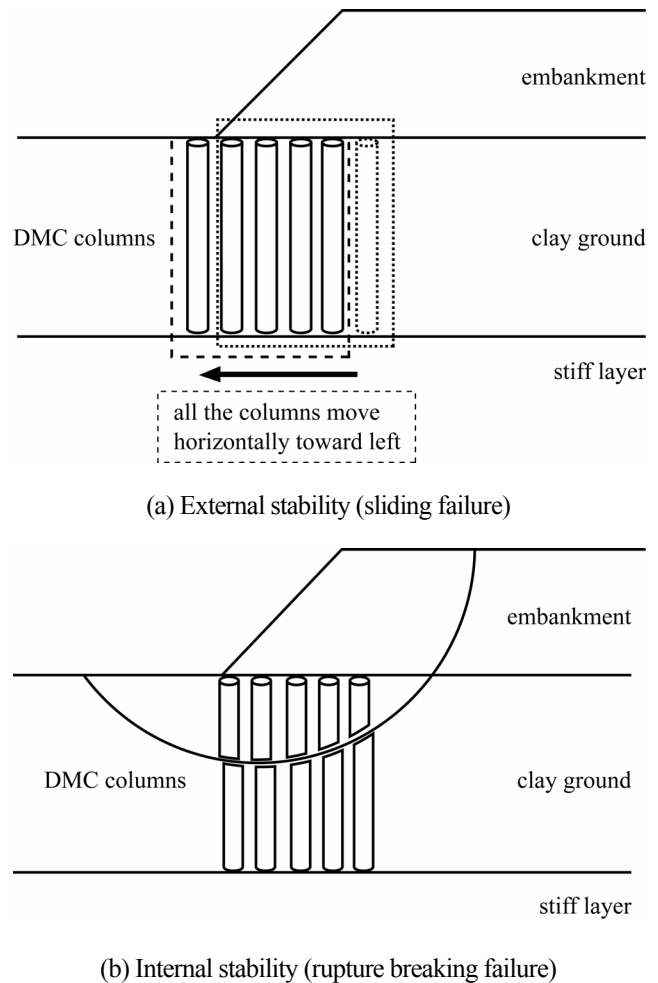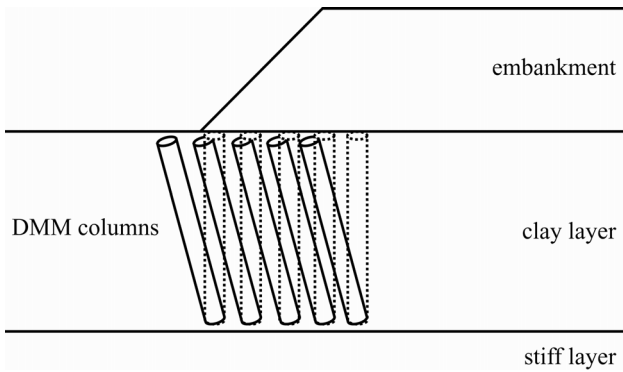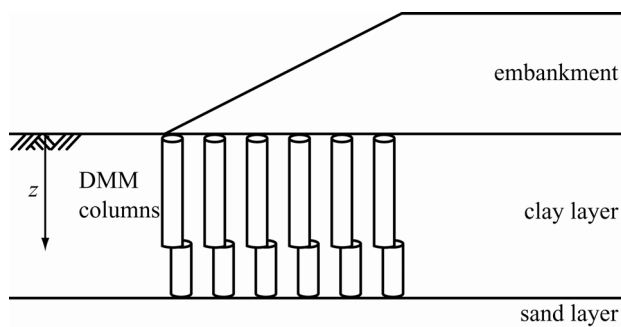

(a) External stability (sliding failure)

(b) Internal stability (rupture breaking failure)
Fig. 1. Assumed failure patterns of DM improved ground in the current design method

For the internal stability, Terashi and Tanaka (1983), Miyake et al. (1991), Karastanev et al. (1997), Hashizume et al. (1998) and Kitazume et al. (1996, 1999) carried out model tests revealing that the DM columns show various failure modes: shear, bending and tensile failure modes, depending not only on the ground and external loading conditions but also on the location of each column, as shown in **Figs. 2(b)** and **2(c)**. However, the current design method does not incorporate the effect of these failure modes, but only the shear failure mode. As the bending and tensile strengths of treated soil are much lower than the compressive strength (Terashi et al., 1980), the current design method based on shear strength alone might overestimate the internal stability (Kitazume and Maruyama, 2007). Kivelo (1998) and Broms (2004) proposed a new design method for the group column type improved ground, in which several failure modes of DM columns are taken into account.

(a) Collapse failure mode in external stability

(b) Shear failure mode in internal stability
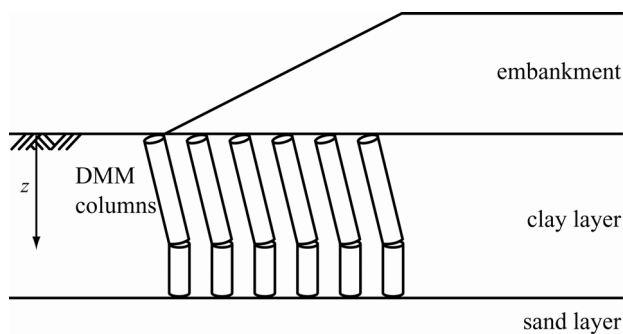
(c) Bending failure mode in internal stability
Fig. 2. Failure modes

Obviously, the improved ground could fail by one of various failure patterns depending on the ground and loading conditions. Each failure pattern is characterized by a particular failure envelope in a loading plane. It is reasonable that the ground should fail by one of the failure patterns that gives a minimum capacity under certain condition. As mentioned above, the current design method does not assume appropriate failure pattern and failure mode that could give the minimum capacity.

However, as far as the author knows, there is few case record of serious failure or large deformation in the group column type improved ground under embankment loading. This is a discrepancy against the overestimation in the current design method. It has been well known that field

column strength is usually much higher than the design strength in Japan, which can bring an additional safety margin in the internal stability, but not in the external stability. Further researches on the failure mechanism and evaluation of stability of each failure pattern and failure mode are required in order to improve the current design method more accurately.

This study targets at the external and internal stabilities of the improved ground in which a series of centrifuge model tests and numerical calculations were carried out to investigate the effect of width, improvement area ratio and column strength of improved ground on the stability of embankment. In the external stability, the deformation of improved ground was discussed in detail. In the model tests, the development of bending moment distribution in the DM columns due to embankment loading was measured in detail. In the internal stability, a series of centrifuge model tests and numerical calculations were also carried out to investigate the effect of DM column strength and improved ground width. In addition to the centrifuge model tests and simple calculations, a parametric calculation on evaluation of stability of column type DM improved ground was carried out to investigate the characteristics of the current design method and the proposed design method. The effect of ground consolidation due to embankment weight, underestimation of ground strength and surface crust are discussed to determine if these factors could serve as an unwritten safety margin and to investigate the applicability of the current design method to evaluation of stability of DM improved ground.

Parts of the study, the external and the internal stabilities, were already presented (Kitazume and Maruyama, 2006 and 2007). In this paper, the above two papers are cited to discuss the external and the internal stabilities as well as a parametric calculation on evaluation of stability of column type DM improved ground to investigate the characteristics of the current design method and the proposed design method.

2. CENTRIFUGE MODEL TESTS

2.1 Apparatus

A series of model tests was carried out in the Mark II Geotechnical Centrifuge at the Port and Airport Research Institute. The centrifuge has a radius of 3.8 m, a maximum payload of 2.7 tons, a maximum acceleration of 113 g and a maximum capacity of 300 g-tons. Details of the centrifuge and the surrounding equipment were described by Kitazume and Miyajima (1995).

All the model tests were performed in a strong specimen box under plane strain condition whose inside dimensions were 70 cm in length, 20 cm in width and 60 cm in depth. One side of the specimen box was made of glass to allow photographic measurements during the flight.

2.2 Model ground preparation

Figure 3 schematically shows a typical example of model ground setup, where a normally consolidated clay ground with 20 cm thick and five rows of DM columns were modeled in Cases 7 and 10. An embankment was constructed on the model ground by means of an in-flight sand raining device in a 50 g acceleration field.
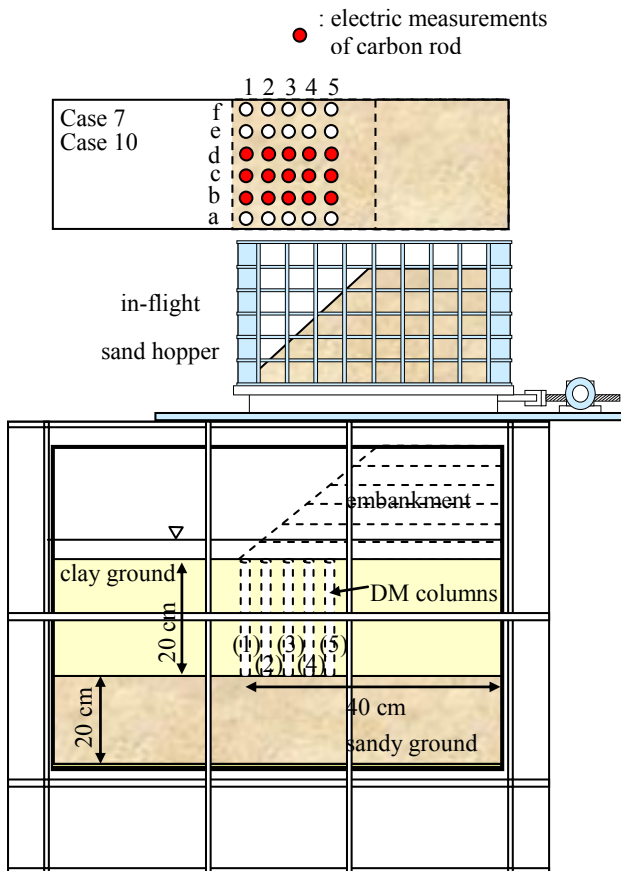

Fig. 3. Model ground setup for Cases 7 and 10

The model ground for all the tests was prepared by the following procedure. A drainage layer of Toyoura sand was placed at the bottom of specimen box. This is fine, uniform sand with a uniformity coefficient, U_c, of 1.38 and an effective grain size, D_{10}, of 0.13 mm. The clay used in the tests was Kaolin clay: its major mechanical properties are summarized in **Table 1**. Kaolin powder was mixed with tap water in a vacuum mixer to produce uniform slurry with water content of 120%. The clay slurry was poured into the specimen box, and then pre-consolidated one dimensionally by vertical pressure of 9.8 kN/m^2 on the laboratory floor to produce 22 cm thick clay ground. After completing the preliminary consolidation, the model clay ground was subjected to centrifugal acceleration of 50 g to allow consolidation by enhanced self-weight and then the thickness of ground became 20 cm.

Table 1. Engineering properties of Kaolin clay

Property	Value
Specific gravity (g/cm^3)	2.721
Liquid limit (%)	59.3
Plastic limit (%)	26.3
Plasticity index	33.0
Coefficient of compression	0.49
Coefficient of consolidation (cm^2/min)	0.15
Strength increment ratio, c_u/p	0.314

Due to the pre-consolidation on the laboratory floor and the self-weight consolidation in the centrifuge, the model ground had a thin layer of over consolidated clay underlain by the thick normally consolidated clay layer. The undrained shear strength profile of the normally consolidated layer was directly measured by an in-flight vane apparatus at a 50 g field, and was $c_u = 1.14 \times z$ (kN/m^2) where c_u and z were undrained shear strength in kN/m^2 and depth in cm, respectively (see **Fig. 4**).

After the self-weight consolidation, the centrifuge was stopped once for preparation of improved ground on laboratory floor. A thin walled tube with an outer diameter of 20 mm was penetrated into the clay ground. The clay inside the tube was then carefully removed using a tiny auger to make a hole, and a model DM column was inserted into the hole after removing the tube. This procedure was repeated to produce the improved ground in a square pattern with an interval of 33 mm in Cases 2 through 11, or in an equilateral triangular pattern with an interval of 23 mm in Case 5. The improvement area ratio, a_s, was defined as the ratio of sectional area of DM column to the hypothetical cylindrical area (CDIT, 2002), and was 0.28 and 0.56 for the former and latter cases, respectively.
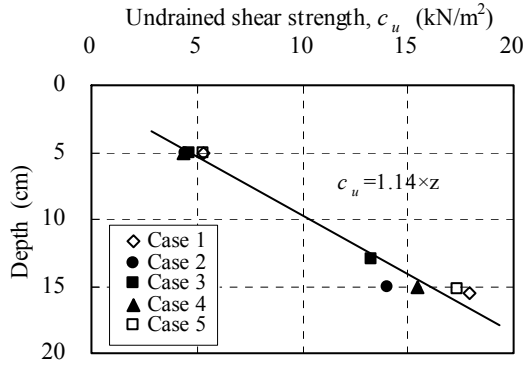
Fig. 4. Undrained shear strength profile with depth

After completing the soil improvement work, the front glass window of specimen box was disassembled and target markers were placed on the side surface of clay ground in a square pattern of 2 cm intervals for photographic measurement. The coordinates of target markers were digitized after the test to obtain the ground deformation in detail. In Cases 2 to 11 as later shown in **Table 3**, several earth pressure gauges are placed on the top surface of the model column and of the clay between in order to investigate the stress concentration phenomenon during the embankment loading.

2.3 Model DM columns

In the present model tests, three types of DM columns were used: an acrylic pipe and cement treated columns, as shown in **Table 2**. A total of 11 model tests was carried out as summarized in **Table 3**. The former model column (A-column) was used in Cases 2 to 5 for investigating the external stability with bending moment measurements, while the latter two (Tl-column and Th-column) were used in Cases 6 to 11 for investigating the internal stability by simulating rupture breaking failure of DM columns.

For the A-column, the acrylic pipe used in the model tests had an inner diameter of 1.6 cm, an outer diameter of 1.9 cm and a length of 20 cm. The flexural rigidity of the pipe, EI, was measured by a loading test as a simple beam and was obtained as 9.3 Nm^2. This was corresponded to the unconfined compressive strength of a treated column of the order of 2 MN/m^2, if the elastic modulus of treated soil was assumed to be 500 ×

q_u. The FEM analyses showed that the flexural rigidity of acrylic pipe was high enough not to influence the stability of ground (Kitazume and Maruyama, 2006). Five sets of two strain gauges were installed on the outer surface of some of the pipes to measure the bending moment distribution (see **Fig. 5**). Fine cables connected to the strain gauges were passed through the inside of pipe so as not to disturb the pipe surface. The outer surface of all the pipes was treated to rough conditions by sand blasting technique. Additional tests were performed after the centrifuge tests, in which the model columns were pulled out from the clay ground on the laboratory floor. According to the test results, the average adhesion mobilized along the cement treated column was almost same as the undrained shear strength of clay ground, while that along the acrylic pipe was about 70% of the clay ground. This difference in the adhesion had negligible effect on the collapse failure (Kitazume and Maruyama, 2006). The self-weight of pipes was controlled to 1.43 g/cm^3 by filling the pipe with a small steel rod and chemical silicone, which corresponded to almost the same order as cement treated soil.

The Tl- and Th-columns, 2 cm in diameter and 20 cm in length, were manufactured using a mixture of Kawasaki clay and normal Portland cement. The mixture was poured into a acrylic mold of 2 cm of inner diameter and 25 cm in length. After curing, the column was extracted from the mold by means of a motor jack for installing into the model ground. The adhesion mobilized along the cement treated column was measured by pulling the column out from the clay ground on the laboratory floor. The test revealed that the average adhesion was almost same as the undrained shear strength of clay ground, although the outer surface of the column was not course condition (Kitazume and Maruyama, 2006).

Table 2. Engineering properties of model columns

name	material	carbon rod		model column			
				mixing condition		strength	
		diameter	strength	w_i	aw	q_u	σ_b
		(mm)	(MN/m²)	(%)	(%)	(kN/m²)	(kN/m²)
A	acrylic	-	-	-	-	-	-
Tl	treated soil	2	62.6	160	12.5	409	132
Th	treated soil	3.2	34.5	160	10.0	1332	331

Table 3. Test conditions and major test results

	Improvement condition						Test result
	Width	No. of rows	Imp. area ratio, a_s	material	q_u	σ_b	Embk. press. at failure, p_{ef}
	(cm)				(kN/m^2)	(kN/m^2)	(kN/m^2)
Case 1	0	-	-	-	-		10.8*
Case 2	8.6	3	0.28	A	-		26.5*
Case 3	15.2	5	0.28	A	-		42.2*
Case 4	21.8	7	0.28	A	-		50.0*
Case 6	8.6	3	0.28	Tl	425	122	16.9 - 23.7
Case 7	15.2	5	0.28	Tl	411	131	26.2 - 35.3
Case 8	21.8	7	0.28	Tl	391	142	25.4 - 32.6
Case 9	8.6	3	0.28	Th	1271	312	33.3 - 49.7
Case 10	15.2	5	0.28	Th	1290	367	34.2 - 50.2
Case 11	21.8	7	0.28	Th	1434	316	47.9 - 68.5

* defined by curve fitting

Fig. 5. Model column made of acrylic pipe

Fig. 6. Model column and carbon rods

In order to detect the model column failure during embankment loading, a carbon rod was embedded into each column before hardening, as shown in **Fig. 6**. Both ends of the carbon rod were connected to a thin cable to measure electric resistance during the test. As the carbon has high electrical transfer, its electric resistance is quite low; however, when the carbon rod is broken due to the rupture breaking failure of the column, the electric resistance jumps to infinity. Accordingly, the measurement of electric resistance can be an indicator for detecting the point in time of column failure, although the location of the failure point would not be detected until after the test. In Cases 6 to 11, all the columns embedded in the model ground had a carbon rod, while the electric measurements were conducted in the b, c and d column lines (see **Fig. 3**).

The mixing conditions for the two model columns are summarized in **Table 2** together with the characteristics of the carbon rod. Both columns had an initial water content, w_i, of 160%, but the amount of cement, aw defined as the dry weight of cement against that of soil, differed. Two types of carbon rod were used. As no suitable carbon rod had been found on the market at beginning, high strength carbon rod was obliged to be used for Th-column, which influenced the treated soil column property dominantely. After then, low strength carbon rod, which didn't influence the column property so much, was found on the market and used for Tl-column. All the columns necessary for the entire model test series, about 300 columns for each, were manufactured at the same time to obtained same column property through the test series as much as possible and cured under moist conditions for more than three months to prevent strength increase during the model test series. The unconfined compressive strength, q_u, and the bending strength, σ_b, of Tl- and Th-columns in **Table 2** were obtained after curing the reference specimens of 2 cm in diameter and 4 cm

in height, and of 2 cm in diameter and 20 cm in length, respectively. As the carbon rod has high strength, its characteristics strongly influence the characteristics of the model column. The large diameter of the carbon rod provides the high column strength of Th-column compared to Tl-column even with a smaller amount of cement mixed. The columns embedded in the model ground were measured for strength after being excavated, and the results are summarized in **Table 2**.

Figure 7 shows the stress strain curves of the model columns with the carbon rod measured in unconfined compression tests, in which the model column was trimmed to 2 cm in diameter and 4 cm in height. The curves clearly show a rapid increase in axial stress and quite a sharp peak at a very small axial strain, followed by a rapid decrease in stress. In the figure, laboratory data of cement treated soil having similar magnitude of strength and different mixing conditions without any carbon rod are plotted together with the data on the model columns simply to show the effect of the embedded carbon rod. By comparing the data with and without the carbon rod, a similar stress strain phenomenon can be seen prior to the peak while a sharper decrease in the axial stress can be seen in the column with the carbon rod. This indicates that the model columns with the carbon rod are more brittle compared to those of the treated soil without any carbon rod.

Fig. 8. Vertical load and deflection curves in bending test

Figure 9 shows the relationship between q_u and σ_b, measured on the reference columns trimmed to 4 cm in length for the q_u test and 20 cm for the σ_b test. Although there is a lot of scatter in the measured data for Th-column, an average strength ratio of 0.28 was obtained, which is within the range of previous research (Terashi et al., 1980).

Fig. 7. Stress strain curves of model columns

Fig. 9. Strength ratio of model columns

Figure 8 shows typical bending test data on the model columns of 2 cm in diameter and 20 cm in length. The tests were conducted in a similar manner to those in concrete engineering (Japan Society of Civil Engineers, 2002). The vertical load increases with increasing vertical deflection, δ, and shows a sudden drop in the vertical load, irrespective of the type of model column. The Tl-column shows a lower peak value at smaller δ values compared to Th-column. In the figure, the electric resistance of the carbon rod, which is converted to a micro unit, is plotted together. The resistance of each column increases gradually with little scattering until the peak vertical load. However, it jumps to infinity at the peak vertical load, which indicates the high applicability of the carbon rod for detecting the point in time of column failure.
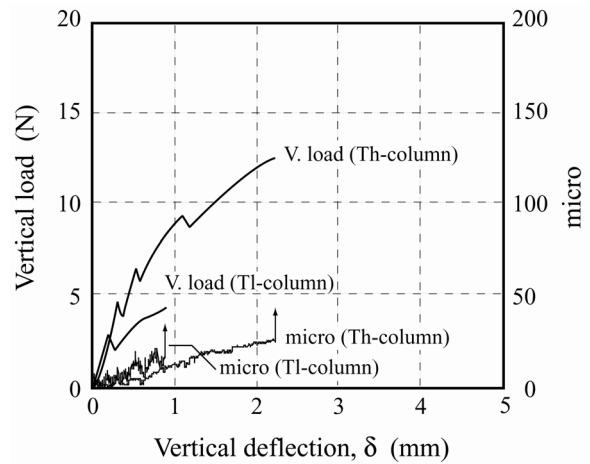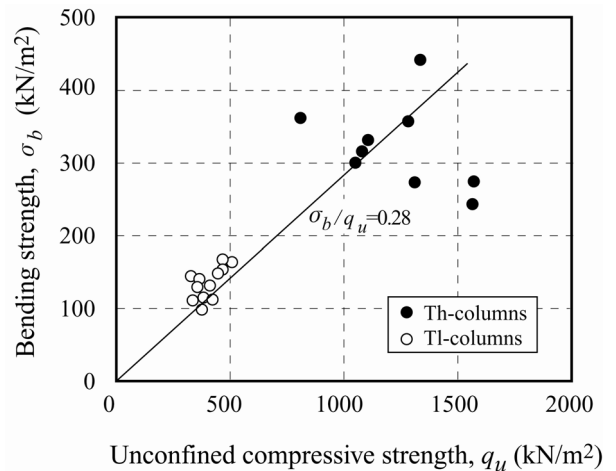
2.4 Embankment loading procedure

The model ground constructed was brought up to a 50 g acceleration field, which corresponded to a 10 m thick soft clay layer improved by DM columns of 1 m in diameter in prototype scale. The model ground was allowed to consolidate by enhanced self-weight to minimize any soil disturbance effect that might be induced during the ground preparation. Next, the model embankment was constructed stepwise under almost undrained conditions using an in-flight sand-raining device: about 1 cm in height per 30 seconds interval until the ground failed. During the embankment loading, the vertical stress increments at the ground surface and at the top of the model columns were measured as well as the electric resis-

tance of the model columns, and the model ground deformation was photographed. After the loading test, the specimen box was disassembled and deformation of the model columns was observed directly.
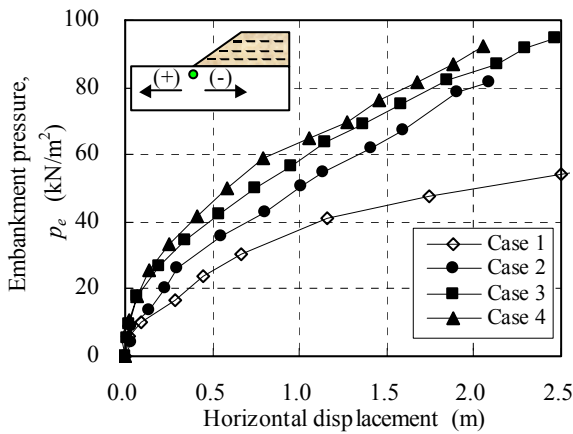
A total of 11 model tests were performed using different materials and a varying number of columns. The test conditions and test results are summarized in **Table 3**. In the test series, Cases 2 to 5 deal with the external stability with the bending moment measurements. Five model tests were performed under various numbers of DM column rows together with an unimproved ground. In the test series, the number of column rows was changed between 3, 5 and 7 rows. In Cases 2 through 4, the number of column rows was changed while the value of a_s remains constant as 0.28. In Case 5, the value of a_s is 0.56 with 5 column rows. The improvement width, D, is defined as a distance between the outer surfaces of forefront and rearmost columns in this study. Cases 6 to 11 deal with the internal stability. The improvement width is defined here as the distance between the outer surfaces of the forefront and rearmost columns.

3. EXTERNAL STABILITY

3.1 Test results

(1) Embankment pressure and displacement

The measured embankment pressure and displacement curves are shown in **Fig. 10(a)** for the improved ground with $a_s = 0.28$, together with the unimproved ground. In the figure, the vertical axis shows the embankment pressure measured at the ground surface, p_e, and the horizontal axis shows the horizontal displacement at the toe of embankment slope, δ_h, that is converted to a prototype scale by multiplying the centrifuge acceleration. In the unimproved ground (Case 1), a relatively small horizontal displacement takes place as long as p_e remains at a very low level, but δ_h increases rapidly with further increase of p_e. In the improved grounds (Cases 2 through 4), however, δ_h increases with increasing p_e, but the magnitude of δ_h is small compared to that in the unimproved ground. The magnitude of δ_h becomes smaller when D increases.

Figure 10(b) shows the effect of a_s on the relationship between p_e and δ_h. The p_e and δ_h curves for Cases 3 and 5 almost coincide with each other, which indicates that there is no significant difference between $a_s = 0.28$ and 0.56 in the case of $D = 7.7$ m in a prototype scale.

(2) Embankment pressure at ground failure and improvement width

As neither a clear peak nor constant value can be seen in p_e and δ_h curves, the measured relations are re-plotted in a semi-logarithmic scale to detect ground failure as shown in **Fig. 11** for Case 3. A clear bending point can be detected in the figure. By fitting the initial and final parts of the curve by two straight lines, the embankment pressure at ground failure, p_{ef}, is defined as a pressure at the intersection of the two straight lines as shown in the figure, and is summarized in **Table 3**. The relationship between p_{ef} and D is plotted in **Fig. 12** for all the test cases. It can be seen that p_{ef} increases gradually with increasing D. As mentioned above, p_{ef} of the improved ground with $a_s = 0.56$ is almost the same as that with $a_s = 0.28$.

(a) Effect of improvement width

(b) Effect of improvement area ratio

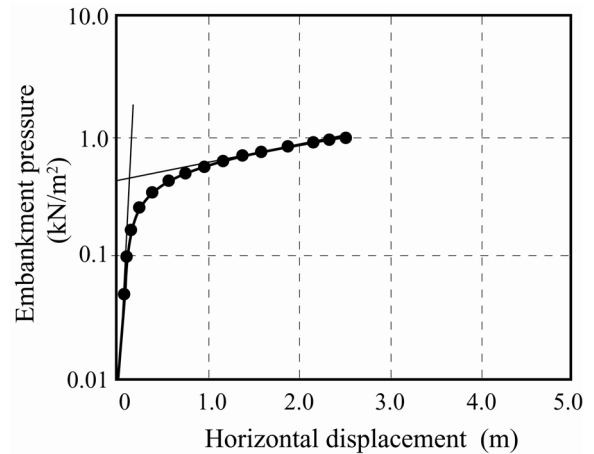**Fig. 10**. Embankment pressure and horizontal displacement curves

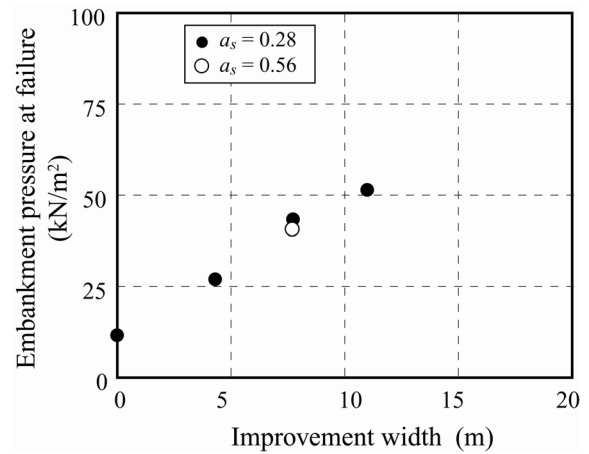**Fig. 11**. Embankment pressure and horizontal displacement curve in a semi-logarithmic scale

Fig. 12. Relationship between embankment pressure at ground failure and width of improved area
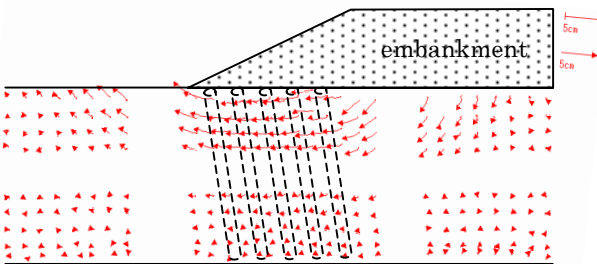
(3) Ground deformation

The ground deformation obtained after embankment loading is shown in **Fig. 13** for the unimproved ground and for the improved grounds with $a_s = 0.28$. This was obtained by digitizing the coordinates of target markers placed on the side surface of model ground. In the case of the unimproved ground (Case 1), a sort of slip circle deformation can be seen at a shallow depth close to the embankment slope. After the ground failure, a large horizontal ground displacement is typically observed for further embankment loading.
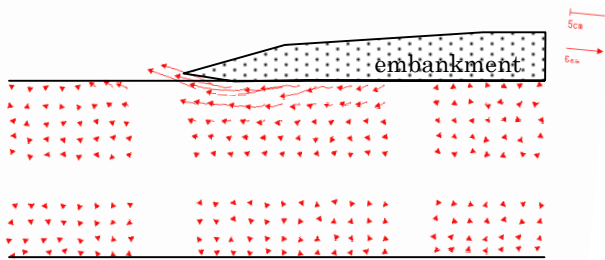
(a) Unimproved ground (Case 1)
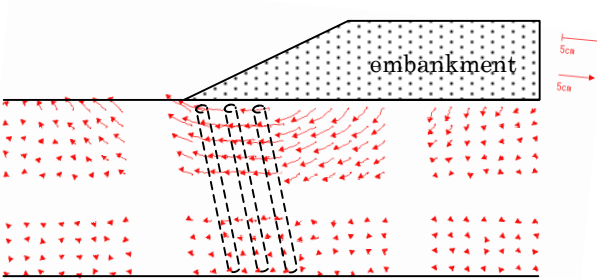
(b) Improved ground (Case 2)

(c) Improved ground (Case 3)
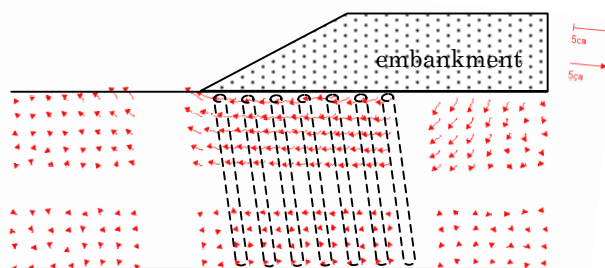
(d) Improved ground (Case 4)
Fig. 13. Ground deformation

In the case of the improved ground with $D = 4.3$ m (Case 2), a relatively large ground deformation can be seen in the shallow and middle depths of the ground. As embankment loading, the ground displacement increases but no slip circle failure takes place. The ground deformation observed in Cases 3 and 4 (**Figs. 13(c)** and **13(d)**), are very similar to that of Case 2. The ground deformation will be discussed later in detail.

(4) DM column displacement

The DM columns after embankment loading in Case 3 are shown in **Fig. 14**. All the columns tilt like dominos at the toe with negligible settlement. The inclination angle is almost the same throughout the columns, indicating that the improved area deforms uniformly as a simple shear failure. This phenomenon was observed throughout the improved grounds irrespective of D and a_s.
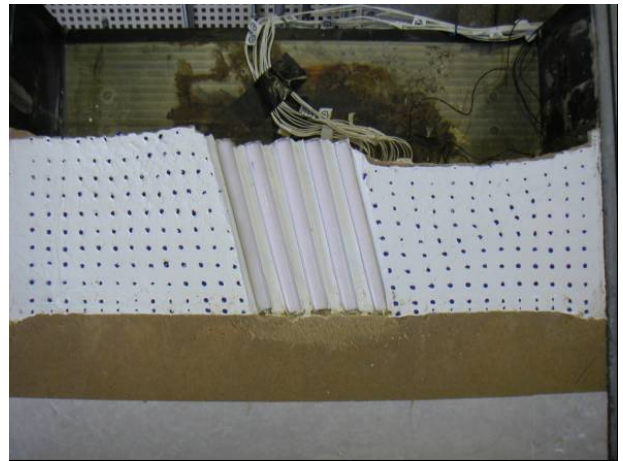

Fig. 14. Column displacement (Case 3)

(5) Horizontal displacement distribution

In order to investigate the ground deformation in detail, the horizontal displacement distributions with depth measured at the toe of embankment slope are shown in **Fig. 15** for the unimproved and improved grounds, in which the horizontal displacements measured at various loading stages are plotted in a prototype scale. It can be seen in the unimproved ground (**Fig. 15(a)**), that a relatively small displacement takes place at a shallow depth at ground failure (p_{ef} = 10.8 kN/m^2). After the ground failure, an large horizontal deformation takes place with further filling especially at a shallow depth of ground, while small displacement takes place at a deep layer. The difference in magnitude of horizontal displacement clearly indicates that the ground fail with a slip circle failure pattern passing through the shallow layer.

In the case of the improved ground (**Figs.15(b)** to **15(d)**), however, horizontal displacement at the toe of embankment slope, corresponding to the forefront column, develops with increasing p_e, but its distribution is almost linear with depth throughout the embankment loading. This phenomenon can also be seen at the vertical line of the rearmost column. The

horizontal displacement at the bottom of all the columns is negligible. This displacement distribution can be seen throughout the improved grounds. As the front surface of ground on which the target markers are placed corresponds to the intermediate between the columns, it is found that the clay there does not slip through the columns but displaces together with the columns. These observations indicate that the improved area does not fail with a sliding failure pattern but with a collapse failure pattern, a sort of domino failure, irrespective of D and a_s. A similar phenomenon has been observed in the group column type improved grounds subjected to vertical and horizontal loads (Kitazume et al., 2000).

It can be concluded from **Figs. 13** to **15** that the DM column has the effect of changing the ground failure pattern from the slip circle failure to the collapse failure. As far as the model test conditions concerned, the collapse failure pattern is less stable than the sliding failure pattern in the group column type DM improved ground, irrespective of the loading conditions.
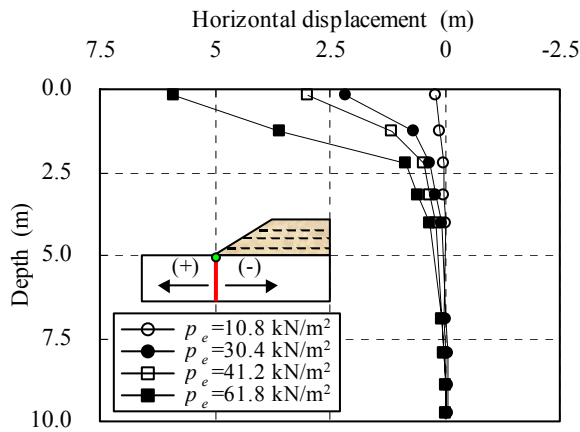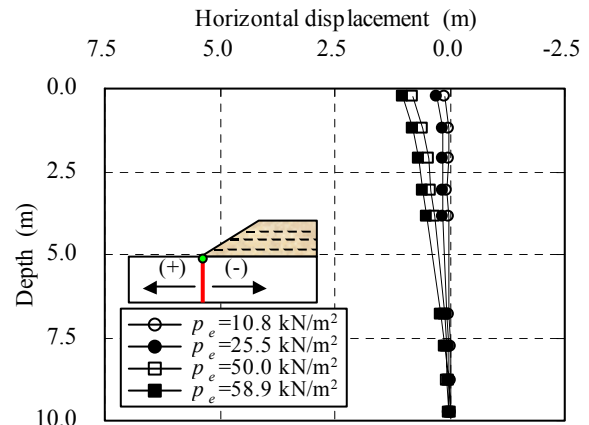

(a) Unimproved ground (Case 1)
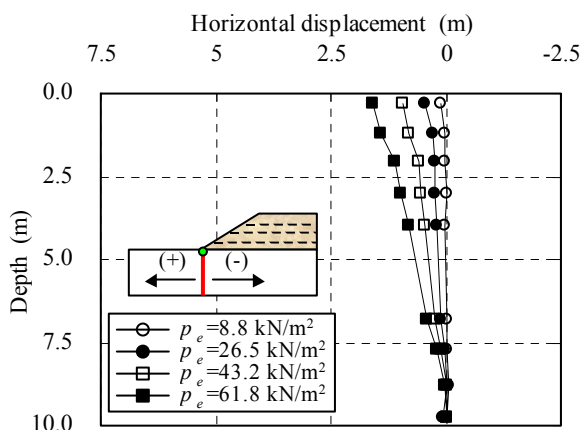
(b) Improved ground (Case 2)
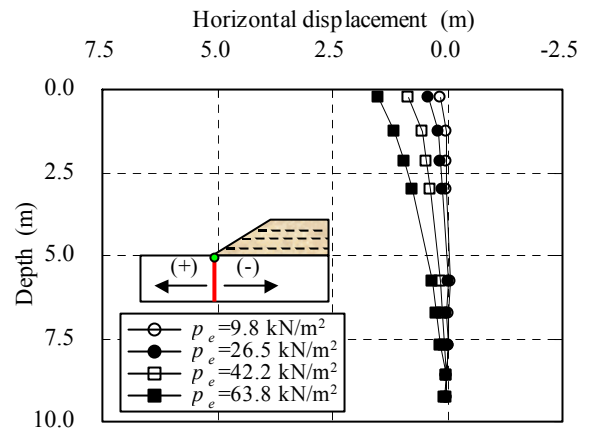
(c) Improved ground (Case 3)

(d) Improved ground (Case 4)

**Fig. 15**. Horizontal displacement distribution with depth

3.2 Discussion

(1) Evaluation of stability for unimproved ground

The stability of the unimproved ground (Case 1) is evaluated by Fellenius slip circle analysis. In the slip circle analysis, the value of p_{ef} is calculated by changing the embankment height until the safety factor becomes unity and is obtained as 15.7 kN/m². The calculated value is about 45% higher than the model test result of p_{ef} = 10.8 kN/m².

(2) Evaluation of sliding failure for improved ground

The external stability of the improved ground is evaluated by the current design method first (PWRC, 2004), in which the sliding failure pattern is assumed, as shown in **Fig. 16**. The formulations for the sliding failure are expressed as Eqs. (1) to (6), which are based on the horizontal load equilibrium of active and passive earth pressures acting on the side boundaries of improved area and the shear strength mobilizing at the bottom of improved area. The ultimate active and passive earth pressures according to Rankin's theory are adopted in the calculation.
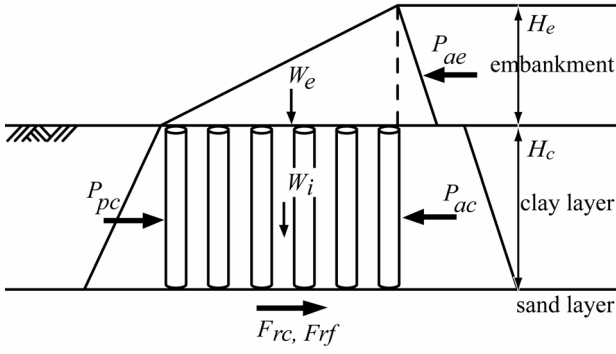
Fig. 16. Sliding failure analysis in the current design

$$Fs = \frac{P_{pc} + F_{rf} + F_{rc}}{P_{ae} + P_{ac}} \tag{1}$$

$$P_{ae} = \int_0^{He} \gamma_e \cdot z \cdot \tan^2\left(\frac{\pi}{4} - \frac{\phi_e}{2}\right) dz \tag{2}$$

$$= \gamma_e \cdot H_e \cdot \tan^2\left(\frac{\pi}{4} - \frac{\phi_e}{2}\right) \cdot \frac{H_e}{2}$$

$$P_{ac} = \int_0^{Hc} \gamma_e \cdot H_e + \gamma_c \cdot z - 2 \cdot (c_{u0} + k \cdot z) dz \tag{3}$$

$$= \left\{ 2 \cdot \gamma_e \cdot H_e - 2 \cdot (2 \cdot c_{u0} + k \cdot H_c) + \gamma_c \cdot H_c \right\} \cdot \frac{H_c}{2}$$

$$P_{pc} = \int_0^{Hc} \gamma_c \cdot z + 2 \cdot (2 \cdot c_{u0} + k \cdot z) dz \tag{4}$$

$$= \left\{ \gamma_c \cdot H_c + 2 \cdot (2 \cdot c_{u0} + k \cdot H_c) \right\} \cdot \frac{H_c}{2}$$

$$F_{rf} = \left\{ \gamma_t \cdot H_t + \gamma_e \cdot H_e \cdot \frac{n}{1 + (n+1) \cdot a_s} \right\} \cdot a_s \cdot \tan\phi_s \cdot D \tag{5}$$

$$F_{rc} = (c_{u0} + k \cdot H_c) \cdot (1 - a_s) \cdot D \tag{6}$$

After substituting Eqs. (2) to (6) into Eq. (1), the following quadratic equation with respect to the embankment height, H_e, is obtained. As the magnitude of the left hand terms is always negative when $H_e = 0$, two real number solutions are obtained while the meaningful solution is the positive one.

$$\frac{\gamma_e}{2} \cdot \tan^2\left(\frac{\pi}{4} - \frac{\phi_e}{2}\right) \cdot H_e^2 + \left\{ \gamma_e \cdot H_c - \gamma_e \cdot \frac{n}{1 + (n+1) \cdot a_s} \cdot a_s \cdot \tan\phi_s \cdot D \right\} \cdot H_e$$

$$- \left[\begin{array}{c} 2 \cdot (2 \cdot c_{u0} + k \cdot H_c) \cdot H_c \\ + \left\{ \gamma_t \cdot H_c \cdot a_s \cdot \tan\phi_s + (c_{u0} + k \cdot H_c) \cdot (1 - a_s) \right\} \cdot D \end{array} \right] = 0 \tag{7}$$

The embankment pressure at sliding failure, $p_{ef,sliding}$, is calculated by the following equation:

$$p_{ef,sliding} = \gamma_e \cdot H_{ef,sliding} \tag{8}$$

According to the formulations, the magnitude of $p_{ef,sliding}$ is influenced by the internal friction angle of base sandy ground, ϕ_s, and the stress concentration ratio, n. As the embankment pressure concentrates on the DM columns due to their high rigidity, the stress concentration ratio, n, is defined by a stress acting on the DM columns against that on clay between the columns (CDIT, 2002). A series of parametric calculations was

conducted changing the magnitude of ϕ_s and n to investigate their effect on $p_{ef, sliding}$. In order to perform the parametric calculations, the shape of embankment is assumed as a trapezoid extending from the forefront column to the rearmost column, as shown in **Fig. 16**. The inclination angle of embankment slope increases with increasing the embankment height. This assumption does not coincide with the model test conditions, where the inclination angle of embankment slope is controlled at an almost constant 35° throughout the embankment construction. The undrained shear strength of clay ground and the internal friction angles of bottom sand layer and the embankment are set at the same magnitude as in the FEM analysis (Kitazume and Maruyama, 2006). According to Eq. (7), the stress concentration ratio influences the stability calculation. However, as its value was not obtained in this study, parametric calculations were carried out in the cases of $n = 3$, 5 and 10 to investigate its effect on $p_{ef,sliding}$. The calculated embankment pressures are plotted in **Fig. 17** along D. The $p_{ef,sliding}$ increases with increasing D. The n and ϕ_s slightly influence $p_{ef,sliding}$.
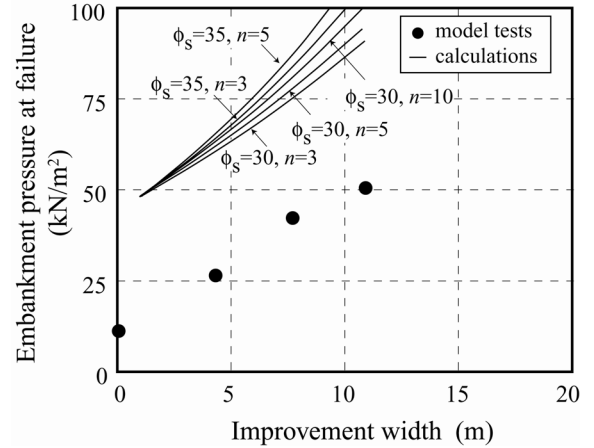

Fig. 17. Comparison of calculations for sliding failure with model test results

Figure 17 also plots the model test results, which are the same as those in **Fig. 12**. In comparison with the model test results, the calculated $p_{ef,sliding}$ are about two times higher irrespective of any combination of n and ϕ_s. In order to investigate the cause of the overestimation in detail, the resistance force components in the calculation are shown in **Fig. 18**. It is found that the passive earth pressure component of resistance force, P_{pc}, is constant irrespective of D, but the shear strength components at the bottom of improved area, F_{rf} and F_{rc}, increase with increasing D. Furthermore, the P_{pc} has a dominant role in the total resistance force, which means that the accuracy of evaluation greatly depends upon the accuracy of estimating P_{pc}.
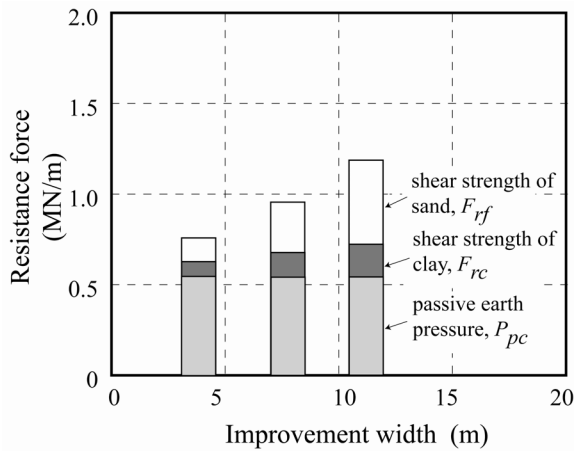
Fig. 18. Resistance force components for sliding failure

Trial calculations were conducted to investigate the effect of the mobilization degree of passive earth pressure on $p_{ef,sliding}$, and the results are shown in **Fig. 19**. In the calculation, the magnitude of the passive earth pressure is simply reduced to 75%, 50% and 25% while its distribution shape with depth remains constant. The figure clearly shows that $p_{ef,sliding}$ decreases almost in parallel with decreasing P_{pc}. As far as investigating the ground condition in this study, a reduction in the mobilization degree of P_{pc} to a very low value of about 25% to 50% is sufficient for evaluating the experiment with high accuracy. However, it is obvious that this correction cannot be always applied for all the conditions.

According to these parametric calculations, the overestimation by the current design method cannot be explained by the accuracy of soil parameters, but should be explained by the difference of failure pattern: a sliding failure pattern instead of a collapse failure pattern is assumed in the current design method.
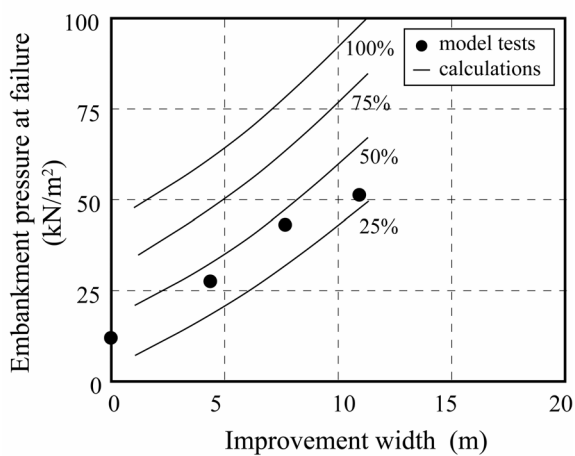
Fig. 19. Effect of mobilization degree of passive earth pressure on embankment at ground failure

(3) Evaluation of collapse failure for improved ground

According to the failure pattern observed in the model tests (collapse failure), a simple stability calculation was carried out next. In the calculation, the improved area was assumed to deform as a simple shear as shown in **Figs. 2(a)** and **20** due to the unbalanced pressure of active and passive earth pressures acting on the side boundaries of improved area. In the calculation, three tilting patterns of DM column can be assumed as shown in **Fig. 21**: (a) at the toe of column, (b) at the center of column and (c) at the heel of column. Tilting pattern (a) was adopted in this calculation, because the base sandy layer was well densified and can be assumed to have sufficient bearing capacity as discussed in **Fig. 14**. For the floating type improvement pattern, however, where the DM columns do not reach the stiff sandy layer but penetrate partially in the clay ground, tilting pattern (b) or (c) should be adopted in the calculation when the clay ground does not have enough bearing capacity. According to the model test results, the clay ground between the DM columns is assumed to deform as a simple shear. However, this assumption is not consistent with the failure pattern (a) of DM columns, because the displacement consistency is not satisfied at the edges of columns. This inconsistency does not have a significant influence on the stability analysis because the resistance moment of clay between the DM columns has a small role in the stability as discussed later. For the calculation with the collapse failure pattern, the moment equilibrium at the bottom of improved area is analyzed as follows:
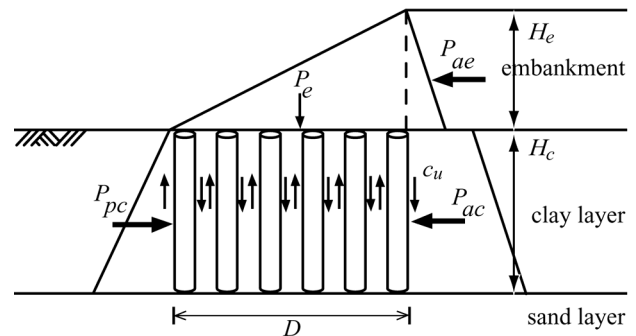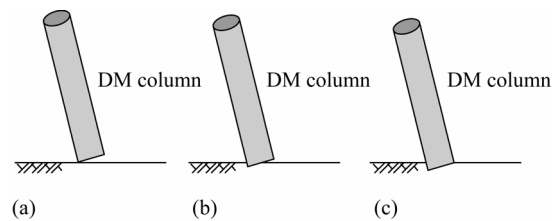

Fig. 20. Collapse failure pattern

Fig. 21. Estimated tilting pattern of DM columns

The driving moments per unit breadth by the active earth pressure of the embankment, M_{ae}, and of the clay ground, M_{ac},

are expressed as Eqs. (9) and (10), respectively, according to Rankin's earth pressure theory.

$$M_{ae} = \int_0^{He} \gamma_e \cdot z \cdot \tan(\frac{\pi}{4} - \frac{\phi_e}{2}) \cdot (H_e + H_c - z)\,dz \qquad (9)$$

$$= \gamma_e \cdot H_e \cdot \tan(\frac{\pi}{4} - \frac{\phi_e}{2}) \cdot \frac{H_e^2 + 3 \cdot H_e \cdot H_c}{6}$$

$$M_{ac} = \int_0^{Hc} \{\gamma_e \cdot H_e + \gamma_c \cdot z - 2 \cdot (c_{u0} - k \cdot z)\} \cdot (H_c - z)\,dz \qquad (10)$$

$$= \frac{H_c^2}{6} \cdot (3 \cdot \gamma_e \cdot H_e + \gamma_c \cdot H_c - 6 \cdot c_{u0} - 2 \cdot k \cdot H_c)$$

Similar to the sliding failure calculation, the shape of embankment is assumed as a trapezoid extending from the forefront DM column to the rearmost DM column as shown in **Fig. 20**, for ease of parametric calculation. The resistance moment components per unit breadth by the adhesion mobilizing at the side surface of DM column, M_{rc}, the weight of DM columns, M_{rt}, the weight of embankment on DM columns, M_{re}, the shear strength of clay between DM columns, M_{sc}, and the passive earth pressure of clay ground, M_{pc}, are expressed as Eqs. (11) to (15), respectively.

$$M_{rc} = \int_0^{Ht} \int_0^{2\pi} \left(\frac{B}{2} \cdot \cos\theta + \frac{B}{2}\right) \cdot \frac{B}{2} \cdot (c_{u0} + k \cdot z) \cdot N \cdot \frac{1}{S}\,d\theta \cdot dz$$

$$= B^2 \cdot H_c \cdot \frac{2 \cdot c_{u0} + k \cdot H_c}{2} \cdot N \cdot \frac{1}{S} \qquad (11)$$

$$M_{rt} = \frac{\pi}{8} B^3 \cdot \gamma_t \cdot H_t \cdot N \cdot \frac{1}{S} \qquad (12)$$

$$M_{re} = \frac{\pi}{8} B^3 \cdot \gamma_e \cdot H_e \cdot \frac{n}{1 + (n+1) \cdot a_s} \cdot N \cdot \frac{1}{S} \qquad (13)$$

$$M_{sc} = \int_0^{Hc} S \cdot (1 - a_s) \cdot H_c \cdot (c_{u0} + k \cdot z) \cdot \frac{z}{H_c} \cdot (N - 1)\,dz$$

$$= S^2 \cdot (1 - a_s) \cdot H_c \cdot \frac{2 \cdot c_{u0} + k \cdot H_c}{2} \cdot (N - 1) \qquad (14)$$

$$M_{pc} = \int_0^{Hc} \{\gamma_c \cdot z + 2 \cdot (c_{u0} + k \cdot z)\} \cdot (H_c - z)\,dz$$

$$= \frac{H_c^2}{6} \cdot (\gamma_c \cdot H_c + 6 \cdot c_{u0} + 2 \cdot k \cdot H_c) \qquad (15)$$

According to the moment equilibrium at the bottom of DM column, the following equation can be satisfied:

$$M_{ae} + M_{ac} = M_{rc} + M_{rt} + M_{re} + M_{sc} + M_{pc} \qquad (16)$$

After substituting Eqs. (9) to (15) into Eq. (16) and expanding the equation, the following cubic equation with respect to the embankment height, H_e, is obtained:

$$-\frac{\gamma_e}{6} \cdot \tan(\frac{\pi}{4} - \frac{\phi_e}{2}) \cdot H_e^3 - \frac{\gamma_e}{2} \cdot \tan(\frac{\pi}{4} - \frac{\phi_e}{2}) \cdot H_c \cdot H_e^2$$

$$+ \left\{ \frac{\gamma_e}{2} \cdot H_c + \frac{\pi}{4} \cdot \sqrt{\frac{a_s}{\pi}} \cdot B^2 \cdot \gamma_e \cdot \frac{n}{1 + (n+1) \cdot a_s} \cdot N \right\} \cdot H_e$$

$$+ \{-\frac{H_c^2}{6}(\gamma_c \cdot H_c - 6 \cdot c_{u0} - 2 \cdot k \cdot H_c)$$

$$+ \sqrt{\frac{a_s}{\pi}} \cdot B \cdot H_c \cdot (2 \cdot c_{u0} + k \cdot H_c) \cdot N$$

$$+ \frac{\pi}{4} \cdot \sqrt{\frac{a_s}{\pi}} \cdot B^2 \cdot \gamma_t \cdot H_t \cdot N$$

$$+ \frac{B}{2} \cdot \sqrt{\frac{\pi}{a_s}} \cdot (1 - a_s) \cdot H_c \cdot \frac{2 \cdot c_{u0} + k \cdot H_c}{2} \cdot (N - 1)$$

$$+ \frac{H_c^2}{6}(\gamma_c \cdot H_c + 6 \cdot c_{u0} + 2 \cdot k \cdot H_c)\} = 0 \qquad (17)$$

Three solutions, either three real numbers or one real and two imaginary numbers, are obtained by Cardano's formula. The meaningful solution for this study should be a real number and positive value. As there are many variables in the equation, a solution, $H_{ef,collapse}$, is obtained numerically for specific ground conditions. The embankment pressure at collapse failure, $p_{ef,collapse}$, is calculated by Eq. (8).

The calculated $p_{ef,collapse}$ for various n and ϕ_e are plotted in **Fig. 22** along D. The $p_{ef,collapse}$ increase almost linearly with D for all cases. The effects of ϕ_e and n are quite small on $p_{ef,collapse}$: the stress concentration ratio in particular has a negligible effect. In the figure, the model test results are also plotted. Although the calculated $p_{ef,collapse}$ still overestimate the model test results for small improvement width but is well coincided for large improvement width. The calculation provides more reasonable values compared with the current design, as shown in **Fig. 17**.

In order to investigate the cause of the overestimation, the resistance moment components for the collapse failure are shown in **Fig. 23**, which are calculated by the proposed calculation for the case of $D = 7.7$ m with $\phi_e = 35$ and $n = 5$. The resistance moment by passive earth pressure, M_{pc}, has a dominant role on $p_{ef,collapse}$, while the other resistance moment components, M_{re}, M_{rt} and M_{rc}, have a comparatively small role. This indicates that the accuracy of evaluating $p_{ef,collapse}$ is strongly governed by the accuracy of estimating the passive earth pressure, similar to the findings in the sliding failure pattern. As the resistance moment component due to the adhesion on the periphery of DM column, M_{rc}, is of the order of 4 to 6 % in the whole resistance moments, it can be concluded that the mobilization degree of the adhesion on the periphery of acrylic pipe, about 70% of treated column, has little effect on the collapse failure.
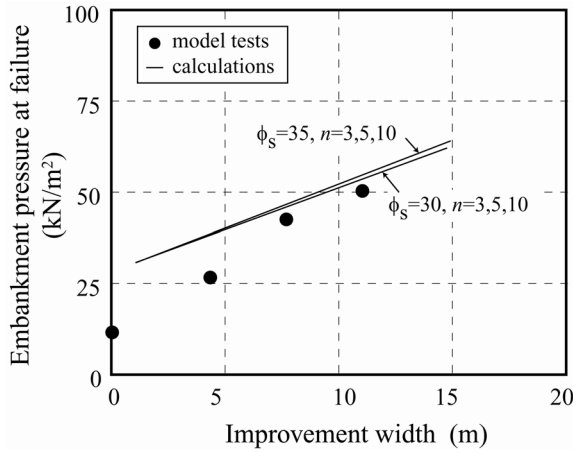
Fig. 22. Comparison of calculations for collapse failure with model test results
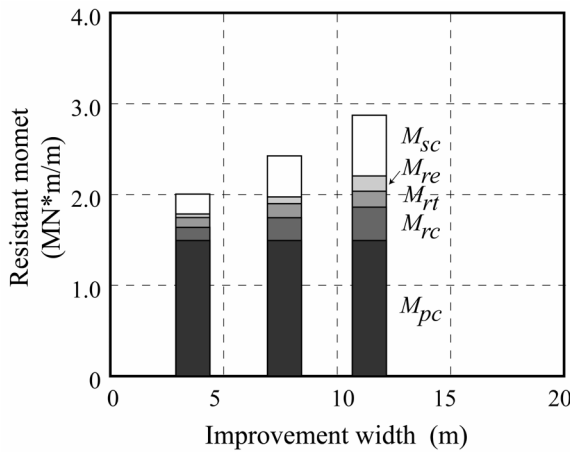

Fig. 23. Resistance moment components for the case of $\phi_e = 35°$ and $n = 5$

This demonstrates the importance of simulating failure patterns similar to the actual behavior in the calculation.
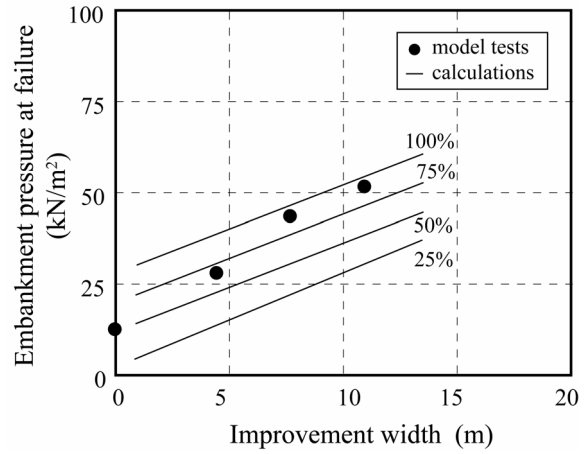

Fig. 24. Effect of mobilization degree of passive earth pressure on embankment pressure at ground failure for collapse failure pattern in the case of $\phi_e = 35°$ and $n = 5$

(4) Effect of improvement area ratio

According to the model tests as shown in **Fig. 10(b)**, the value of $p_{ef,collapse}$ is almost the same even when a_s increases from 0.28 to 0.56. Here, the effect of a_s on $p_{ef,collapse}$ is discussed. In order to investigate the effect in detail, additional parametric calculations of the proposed calculation and FEM analyses were conducted for various a_s values. After defining the ground failure by curve fitting in the FEM analyses, the relationship between $p_{ef,collapse}$ and D is shown in **Fig. 25** for $a_s = 0.28, 0.56$ and 0.75.

It is found that $p_{ef,collapse}$ calculated in the simple calculation and FEM analysis increase with increasing D irrespective of a_s. Although the magnitude of $p_{ef,collapse}$ differs in the two types of calculation, the effect of a_s on $p_{ef,collapse}$ is not very large in both types of calculation.

The resistance moment components of the improved ground are shown in **Fig. 26** for $D = 7.7$ m and $a_s = 0.28, 0.56$ and 0.75, which are calculated by the proposed calculation for the case of $\phi_e = 35°$. As D in the proposed calculation differs slightly for three a_s values even with the same number of column rows, the resistance moment components M_{rc}, M_{rt}, M_{re} and M_{sc} are converted to those corresponding to the improved ground conditions with $a_s = 0.28$ and are plotted in **Fig. 26**.

The figure clearly shows that the resistance moment component generated by M_{pc} has a dominant role and comes up to about 65% of the whole resistance moment, and remains constant irrespective of a_s. The other resistance moment components, M_{rt}, M_{re} and M_{sc}, provide a relatively small portion in the whole resistance moment. The moment components M_{rc}, M_{rt} and M_{re} increase gradually with increasing a_s. However, M_{sc} decreases with increasing a_s, because the volume of clay between the DM columns decreases. The total magnitude of the resistance moment increases by about 13% even when a_s increases from 0.28 to 0.75.
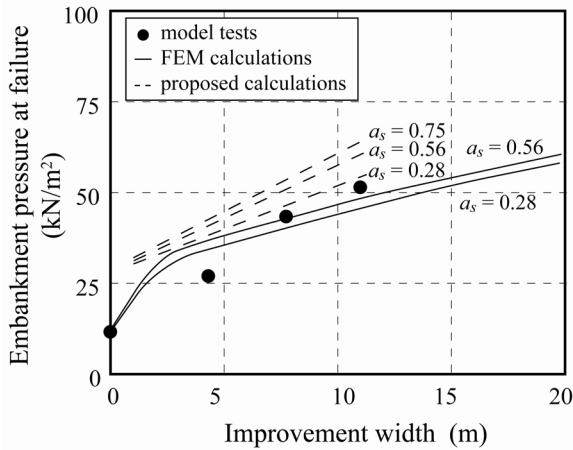
It is well known that the magnitude and shape of passive earth pressure distribution are significantly influenced by many factors such as adhesion and movement of wall, but has not yet been clarified even though extensive research efforts have been made over many years. Here, the effect of passive earth pressure on $p_{ef,collapse}$ is studied by the proposed calculations. **Figure 24** shows the effect of the mobilization degree of passive earth pressure on $p_{ef,collapse}$ for $\phi_e = 35°$ and $n = 5$. In the calculation, the mobilization degree is changed between 75%, 50%, and 25% while its distribution shape is kept constant as a triangle.

It can be seen in the figure that $p_{ef,collapse}$ decreases at about the same magnitude with decreasing the mobilization degree of passive earth pressure. The calculation coincides very well with the model tests when the mobilization degree is about 70% for a relatively small improvement width and 90% for a relatively large improvement width.

Although the proposed calculation is based on the simple assumptions, it has high applicability for evaluating the external stability of the group column type improved ground.

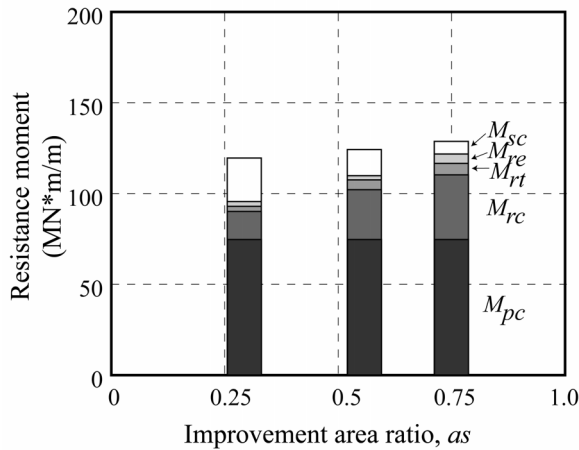**Fig. 25**. Effect of improvement area ratio on embankment pressure at ground failure

Fig. 26. Resistance moment components calculated by the simple calculation for collapse failure pattern in the case of ϕ_e = 35° and n = 5

According to the above discussions, it can be concluded that the improvement area ratio has some effect, but not considerable, on the external stability of improved ground.

Here, the effect of a_s on the internal stability and failure of DM columns is discussed. The DM columns, subjected to compressive and bending force as constructing an embankment, fail with either a shear or bending failure mode when these forces exceed the ultimate strength of DM column. As the bending strength of DM columns is generally much lower than the compressive strength, failure usually occurs with a bending failure mode (Kitazume et al., 2000). Accordingly, the bending failure mode is focused on as follows.

Figure 27 shows the measured bending moment distribution along the columns in a prototype scale for Cases 3 and 5, in which there is the same D but different a_s value. The bending moments in the forefront, middle and rearmost columns measured at ground failure are plotted in the figure. In the forefront column (1) in **Fig. 27(a)**, the bending moment distribution shows a large magnitude in the ground with low a_s (Case 3) but almost zero magnitude in the ground with high a_s

(Case 5). The moment distribution in the middle column (3), as shown in **Fig. 27(b)**, is almost the same distribution shape but the magnitude is larger in low a_s (Case 3) than in high a_s (Case 5), while the moment increases with depth to a maximum at depth of −14 cm. In the rearmost column (5), as shown in **Fig. 27(c)**, negative moment value can be seen at the shallow depth, but positive value at the deeper area. The magnitude of moment is larger in low a_s (Case 3) than in high a_s (Case 5).
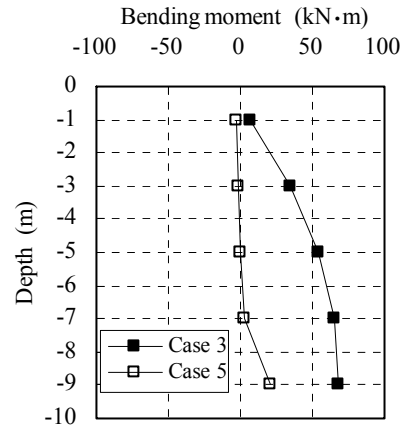
(a) in Column (1), the forefront column
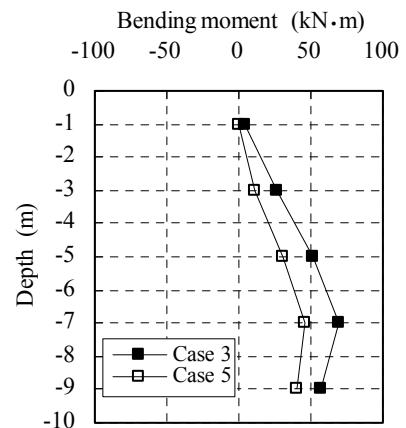
(b) in Column (3), the middle column
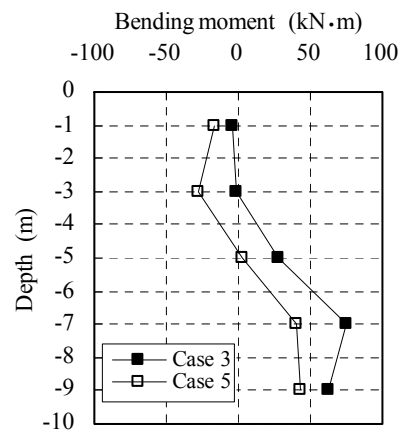
(c) in Column (5), the rearmost column

Fig. 27. Measured bending moment distribution with depth

These figures clearly show that the bending moment distribution in the DM columns is a very similar shape irrespective of a_s except in the forefront column. However, the magnitude of bending moment is small in the improved ground with high a_s. The required DM column strength can be reduced when a_s increases.

This means that according to the test results in this study, the improvement area ratio has a small effect on the external stability but a significant effect on the internal stability of columns.

(5) Effect of DM column diameter

The effect of DM column diameter, B, on the external stability is discussed in this section. **Figure 28** shows the relationship between $p_{ef,collapse}$ and D for various B values, which are calculated by Eqs. (7) and (17). The $p_{ef,collapse}$ increases with increasing D irrespective of B. However, $p_{ef,collapse}$ increases more rapidly with increasing B. According to Eqs. (11) to (13), the resistance moment component due to the adhesion, M_{rc}, increases by a power of two and those due to the weight of column and embankment, M_{rt} and M_{re}, increase by a power of three with increasing B. These increases in the resistance moment bring about $p_{ef,collapse}$ increase with increasing B.

As the diameter of DM column is highly dependent upon the machine capacity and is usually about 1.0 m to 1.5 m in Japan (CDIT, 2002), the calculations for diameter being equal or exceeding 2 m are not realistic. However, it becomes realistic when the columns are overlapped to create treated soil mass having a relatively large sectional area. According to the literatures (e.g. Holm, 1999, Broms, 2004), a column wall type and honeycomb type improved ground are proposed in order to improve the stability of embankment slope, where DM columns are overlapped to produce a sort of treated soil panel. The calculation results confirm that such type of improved ground can efficiently achieve considerable improvement effect in the external stability as far as the treated soil panel behaves as a unity.
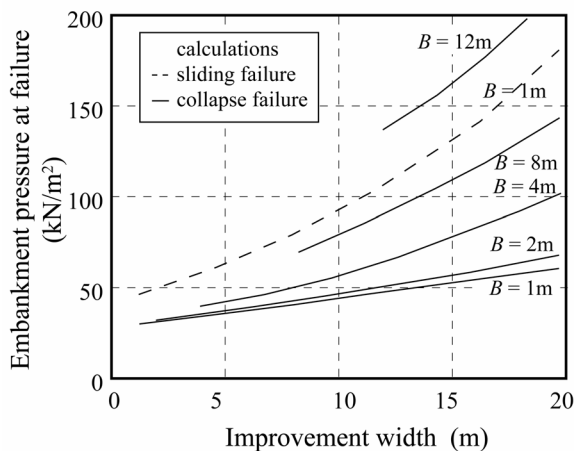
In the figure, the relationship for the sliding failure pattern with $B = 1$ m is also plotted together. It is of interest to note that $p_{ef,sliding}$ almost coincides with $p_{ef,collapse}$ with $B = 10$ m. This indicates that the improved ground may fail with a sliding failure instead of a collapse failure when the DM column diameter or the width of treated soil panel exceeds about 10 m.

3.3 Summary

Failure patterns of the column type DM improved ground were investigated by a series of centrifuge model tests, FEM analyses and simple calculations, in which the improved ground is subjected to embankment loading. The major conclusions derived in this study are as follows:

1) The embankment pressure at ground failure increases gradually with increasing the improvement width. However, the embankment pressure at failure is almost the same in the improved ground with a_s of 0.28 and 0.56.

2) The DM column has the effect of changing the ground failure mode from the slip circle failure to the collapse failure, which provides a relatively large increase of embankment pressure at ground failure. The collapse failure pattern instead of the sliding failure pattern is observed in the model tests.

3) The current design method overestimates the model test results, because a sliding failure pattern is assumed instead of a collapse failure pattern. A proposed calculation based on the collapse failure pattern has relatively high applicability for evaluating the external stability of the group column type DM improved ground.

4) The effect of improvement area ratio is relatively small for the external stability, because the resistance moment does not increase very much even if the improvement area ratio increases. However, the improvement area ratio has a dominant effect on the internal stability of improved ground where the bending moment induced in the DM columns remains a relatively small value as the improvement area ratio increases.

5) The DM column diameter has the effect of improving the external stability of improved ground. The overlapping of DM columns can increase the external stability.

6) The importance of simulating appropriate failure patterns of improved ground is demonstrated for evaluating the external stability accurately.

Fig. 28. Effect of DM column diameter on embankment pressure at ground failure
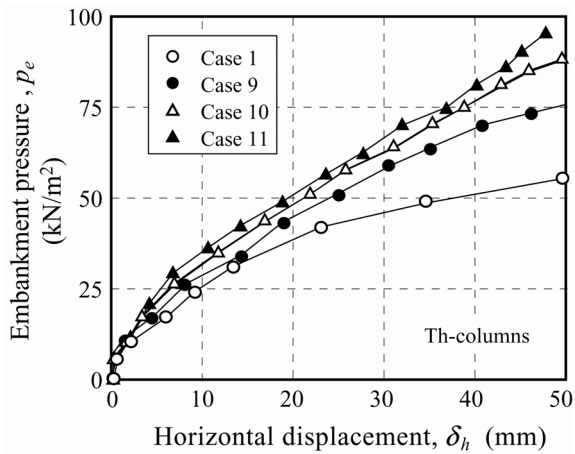
4. INTERNAL STABILITY

4.1 Test results
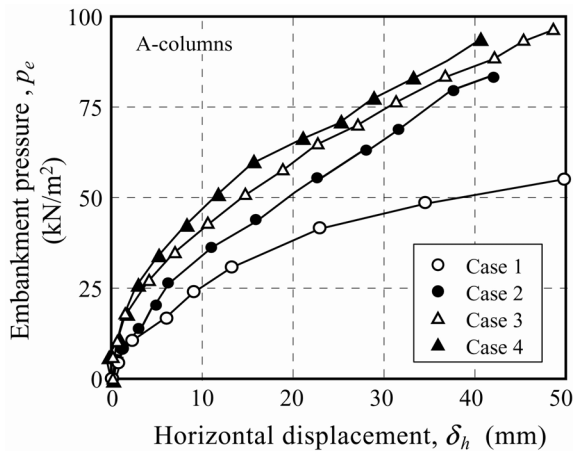
(1) Embankment pressure and displacement

The embankment pressure, p_e, and horizontal displacement, δ_h, curves are shown in **Figs. 29(a)** to **29(c)** for the improved
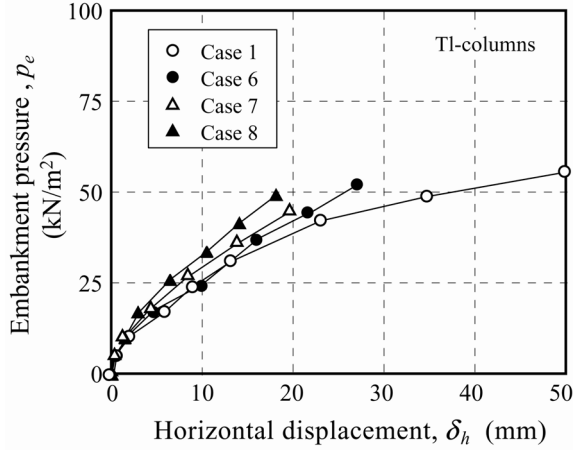
(a) Improved ground with Tl-columns

(b) Improved ground with Th-columns

(c) Improved ground with A-columns

Fig. 29. Embankment pressure and horizontal displacement curves

ground with different column materials, together with the unimproved ground. In the figure, the vertical axis shows the embankment pressure measured at the ground surface, and the horizontal axis shows the horizontal displacement at the toe of the embankment slope.

In the unimproved ground (Case 1), a relatively small horizontal displacement takes place as long as p_e remains at a very low level, but δ_h increases rapidly with further increase of p_e. In the improved ground with Tl-columns (Cases 6 to 8), δ_h increases with increasing p_e (**Fig. 29(a)**), but its magnitude is slightly smaller than that of the unimproved ground. It decreases as the number of columns increases. A similar phenomenon can be seen in the improved ground with Th- and A-columns, as shown in **Figs. 29(b)** and **29(c)**, respectively. As the embankment loading continued to a relatively high value for the ground with Th- and A-columns, it can clearly be seen that the ground improvement effect on the curve becomes more dominate with increasing δ_h. Comparing the figures, the magnitude of δ_h decreases as the column strengh and/or number of columns increases.

In order to investigate the effect of column failure in detail, the δ_h - P_e curves of Cases 6 to 11 are plotted again in **Figs. 30(a)** to **30(f)**. In the figure, the letters beside the curves indicate the point in time and the ID number of the column that shows rupture breaking failure. The column ID is numbered as Row 1, 2, 3 and so on from the forefront column, and Line a, b, c and so on from the window, as shown in **Fig. 3**.

In Case 6 (**Fig. 30(a)**), one of the forefront columns, Tl-1d, failed first at p_e of about 16.9 kN/m². As p_e increased, the other forefront columns, Tl-1b and Tl-1c, failed. The second and third rows of columns failed one by one at p_e of 23.7 and 35.7 kN/m², respectively. It can be concluded that the columns fail in sequence from the forefront to the rearmost column. It is of interest to note that the p_e value continues to increase even after many columns fail.

In Case 9 (**Fig. 30(d)**), with Th-columns, the forefront columns, Th-1b failed first at p_e of 33.3 kN/m², which was higher than that in Case 6 due to the high column strength. Then Th-1d and Th-1c columns failed as increasing embankment loading. The third row columns, Th-3b, failed then.

Figures 30(b) and **30(e)** show the test data of Cases 7 and 10. In Case 7, one of the forefront columns, Tl-1b, failed first at p_e of 26.2 kN/m², and the second and third row columns, Tl-2b, Tl-2d and Tl-3c, failed at the same time. As p_e increased, the columns failed one by one in sequence from the forefront to the rearmost column, which was a similar phenomenon to that observed in Cases 6 and 9. In Case 10, the forefront columns failed one by one at p_e of 34.2 to 50.2 kN/m² (**Fig. 30(e)**). When p_e increased to 79.6 kN/m², the rearmost columns, Th-5b, Th-5c and Th-5d, failed instead of the second, third and fourth row columns. After that, Th-4 and Th-3 failed in reverse sequence from the rearmost to the forefront column. In Case 8, the forefront column, Th-1b, failed first at p_e of 25.4 kN/m² (**Fig. 30(c)**), and the first, second and third row columns failed at the next loading step, similar to Case 6. After the

failure of Tl-3b and Tl-3c, one of the rearmost columns, Tl-7b, failed before Tl-4, Tl-5 and Tl-6 failed. As the embankment loading was terminated at a relatively small embankment pressure in this case to prevent heavy column failure, no failure took place in Tl-4, Tl-5 and Tl-6 during the loading.
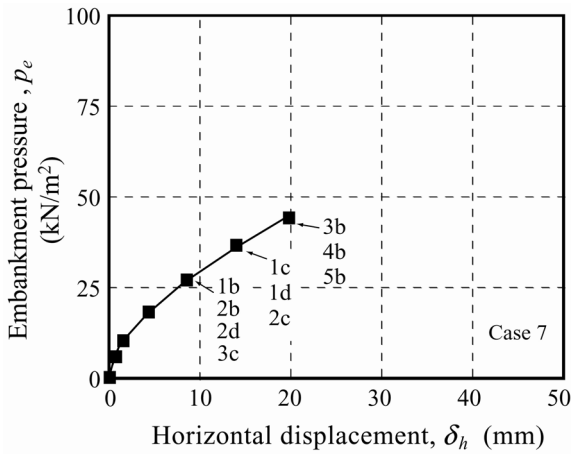
In Case 11, one of the forefront columns, Th-1c, failed first at p_e of 47.9 kN/m^2 (**Fig. 30(f)**). The other two, Th-1 and one of Th-2 columns, failed at the next several loading steps. At p_e of 68.5 and 73.3 kN/m^2, the rearmost columns failed instead of the second and third row columns.
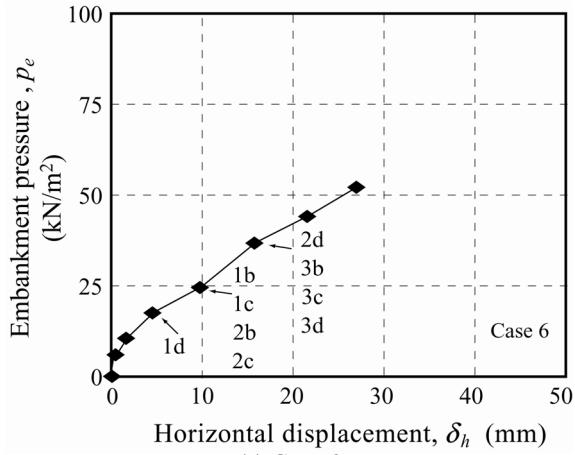
(a) Case 6
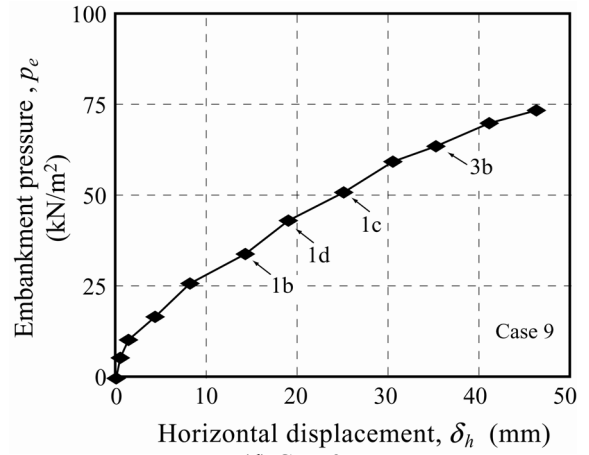
(b) Case 7

(c) Case 8

(d) Case 9
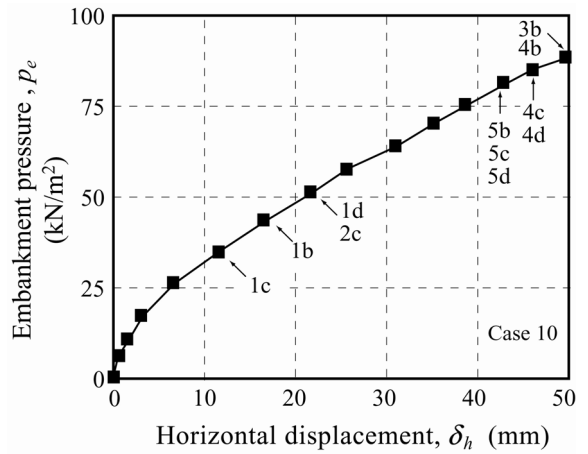
(e) Case 10
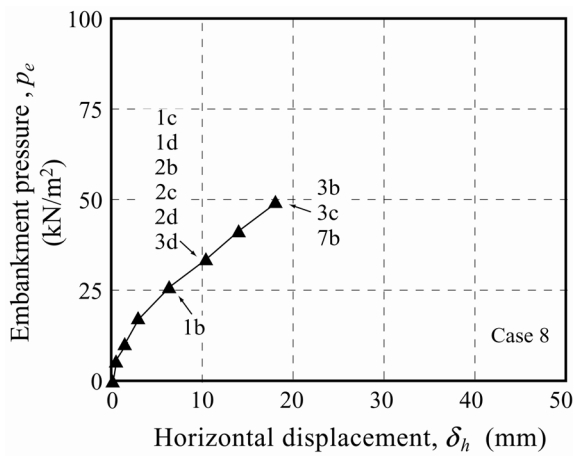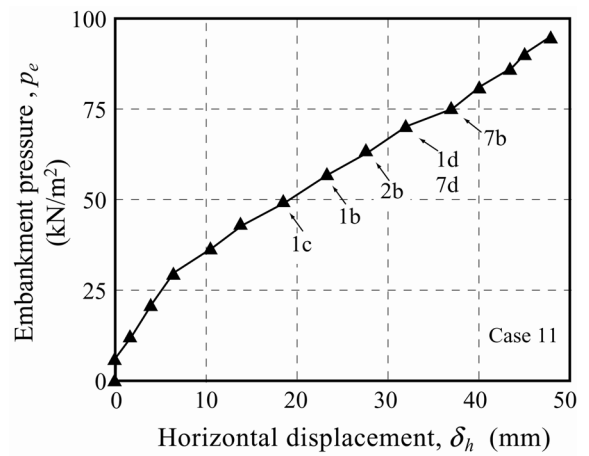
(f) Case 11

Fig. 30. Embankment pressure and horizontal displacement curves together with column failure

It is of interest to note that the embankment pressure continues to increase even after many columns fail. The residual strength of cement treated soil is dependent upon the confining stress, σ_f, and is almost zero in the case of $\sigma_f = 0$, which causes some apprehension about column failure resulting in a sort of catastrophic failure of improved ground. In response, the current design was established based on the "safe side" concept. The test results discussed above provide a possibility for changing the basic concept of the current design method.

(2) Embankment pressure at ground failure and improvement width

As shown in **Fig. 30**, neither a clear peak nor constant value can be seen in the p_e and δ_h curves even after many model columns fail. As far as the model test conditions, the forefront column always fails first, irrespective of the column strength and number of column rows. Here, the ground failure is defined as the rupture breaking failure of the forefront column. The embankment pressure at ground failure, p_{ef}, is summarized in **Table 3**, and the relationship to the improvement width, D, is plotted in **Fig. 31** for Cases 6 to 11. As discussed in **Fig. 30**, the model columns fail one by one at several embankment pressures even in the forefront column. The pressure ranges where the forefront columns fail are plotted as arrows. It can be seen that p_{ef} increases gradually with increasing D, irrespective of column strength.
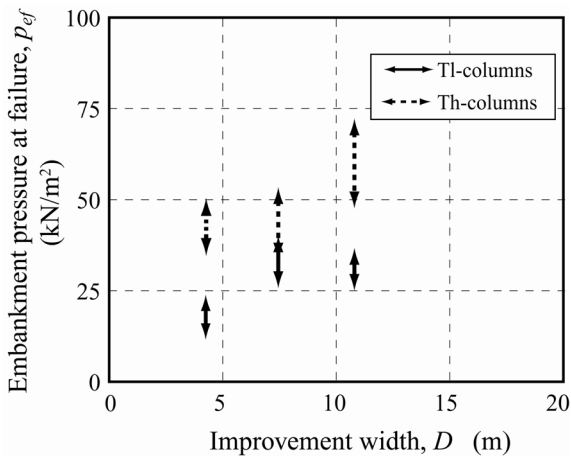
**Fig. 31**. Embankment pressure at ground failure and improvement width

(3) Column failure

Figures 32(a) to **32(f)** show the failure pattern of columns observed after the embankment loading in Cases 6 to 11, respectively. In Case 6, as shown in **Fig. 32(a)**, all the columns tilted counterclockwise with tensile cracks at two depths even when the embankment loading was terminated at a relatively low pressure. The figure clearly shows that the column did not fail by shear failure mode but rather by bending failure mode. As discussed in **Fig. 30(a)**, the forefront column, Tl-1d, failed first and Tl-2d and Tl-3d failed next. Although there is no clear evidence, it is reasonable to assume that bending failure took
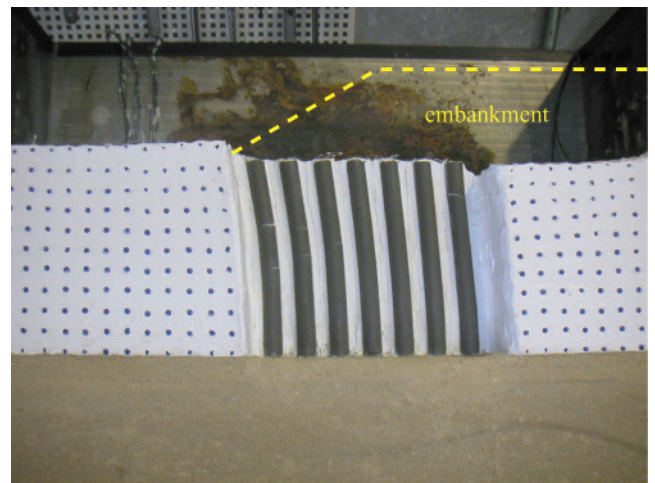
place in each column, one by one. However, the electric measurement of the carbon rod did not show which crack took place first. According to the detailed observation after the test, bending failure took place at a shallow depth first and then at a
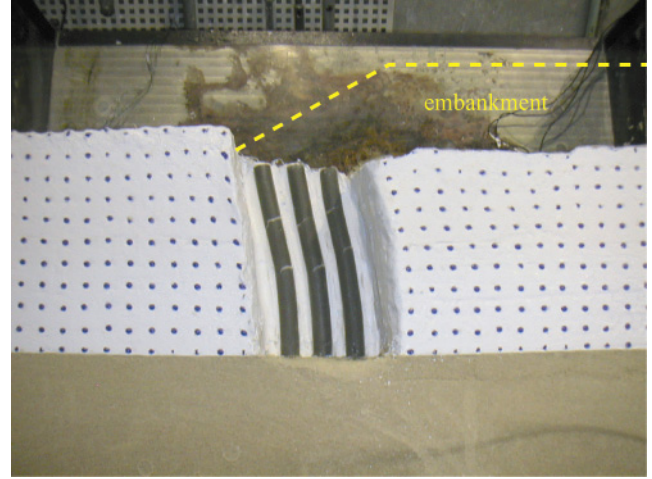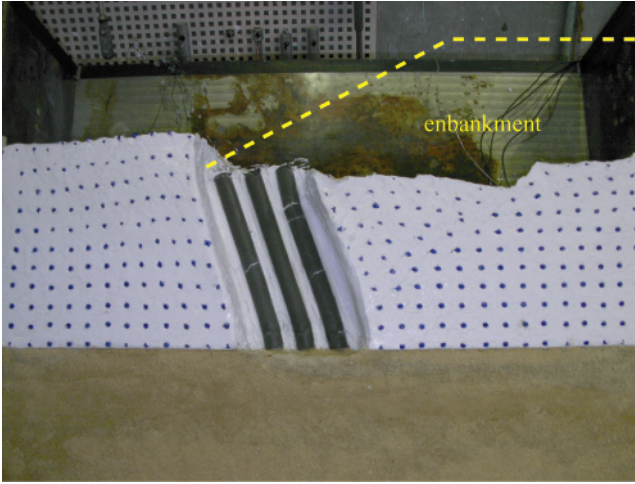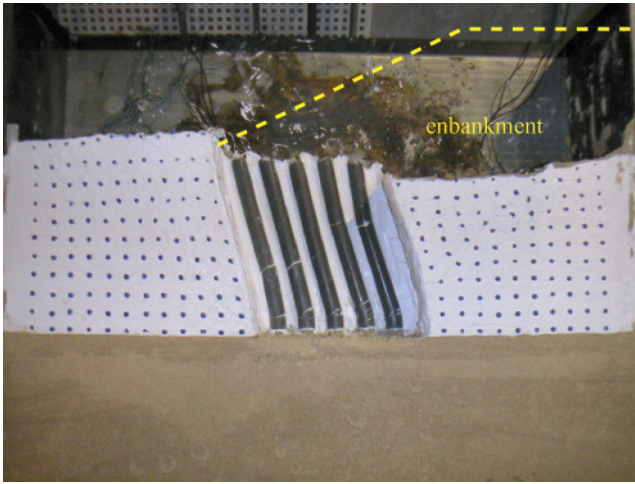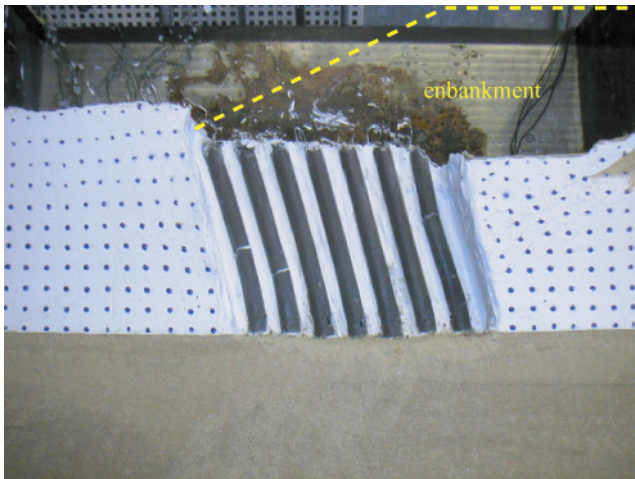
(a) Case 6 (d-line)
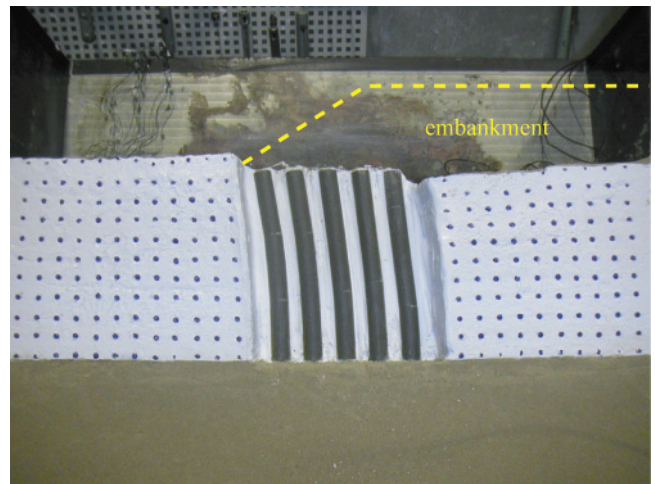
(b) Case 7 (b-line)

(c) Case 8 (b-line)

(d) Case 9 (b-line)

(e) Case 10 (c-line)

(f) Case 11 (b-line)
Fig. 32. Column failure

deep depth. Counterclockwise displacement can be seen in Tl-1d and Tl-2d; however, the top of the rearmost column, Tl-3d, inclined clockwise slightly, due to large ground settle-

ment beneath the embankment (Kitazume and Maruyama, 2005).

In Case 9, the bending failure can be clearly seen in the forefront and rearmost columns (**Fig. 32(d)**). It is of interest to note that the depth at the bending failure in the forefront column is deeper than in Case 6, indicating the influence of column strength, which is explained in detail later.

In Case 7, all the columns titled counterclockwise with bending failure. According to **Fig. 30(b)**, Tl-1b and Tl-2b failed first and then the other three columns, Tl-3b, Tl-4b and Tl-5b, failed at the same p_e of 43.9 kN/m^2. In Case 10, Th-1c and Th-2c failed and tilted counterclockwise, then Th-4c and Th-5c failed and tilted clockwise, as indicated in **Fig. 30(e)**.

Figure 32(c) shows the failure pattern of columns in Case 8. Bending failure took place in Tl-1b, Tl-2b, Tl-3b and Tl-7b. The part of the column shallower than the bending failure point tilted counterclockwise in Tl-1b, Tl-2b and Tl-3b; however, T1-7b titled clockwise. The other columns, Tl-4b, Tl-5b and Tl-6b, tilted counterclockwise without any column failure. A similar phenomenon can be seen in Case 11, as shown in **Fig. 32(f)**. It is interesting to note that the location of bending failure was much deeper in Th-1b and Th-2b than in Th-7b. Again, the location of the breaking failure was much deeper in Case 11 than in Case 8.

Based on the above results, the DM columns do not fail simultaneously but fail one by one by bending failure mode. It is of interest to note that the location of the bending failure is shallower in the low strength column compared to the high strength column, and shallower in the rear side columns compared to the front side columns.

(4) Ground deformation

The ground deformation obtained after the ground failure is shown in **Fig. 33** for the unimproved ground (Case 1) and the improved ground with Th-column (Case 10). The data was obtained by digitizing the coordinates of the target markers placed on the side surface of the model ground. In the case of the unimproved ground (Case 1), a sort of slip circle deformation can be clearly seen at a shallow depth close to the embankment slope. After the ground failure, a large horizontal ground displacement is typically observed with further embankment loading.

In Case 10, a relatively large ground deformation can be seen at a shallow and mid depth. As further embankment loading, the ground displacement increased but no slip circle failure took place. The ground deformation in the other improved ground is very similar to that of Case 10, where no slip circle failure was observed.
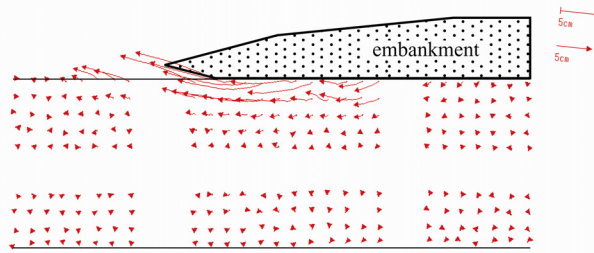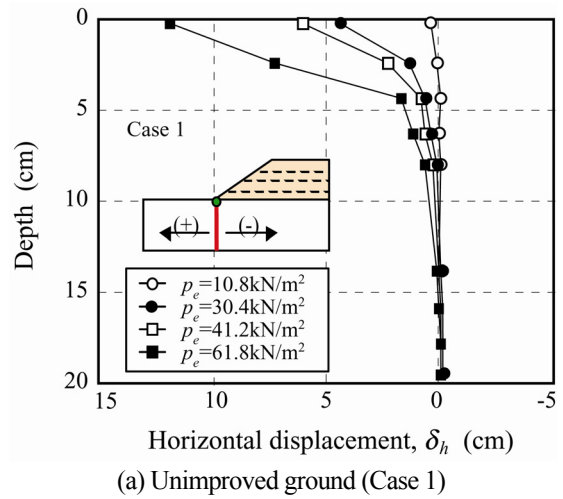
(a) Unimproved ground (Case 1), $p_e = 47.5$ kN/m^2
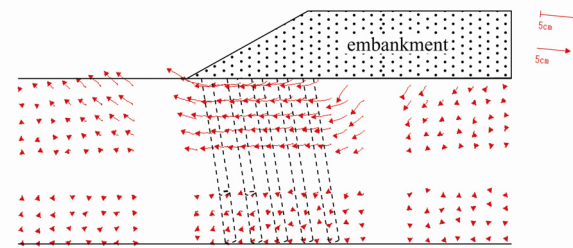
(b) Improved ground (Case 10), $p_e = 56.5$ kN/m^2

Fig. 33. Ground deformation
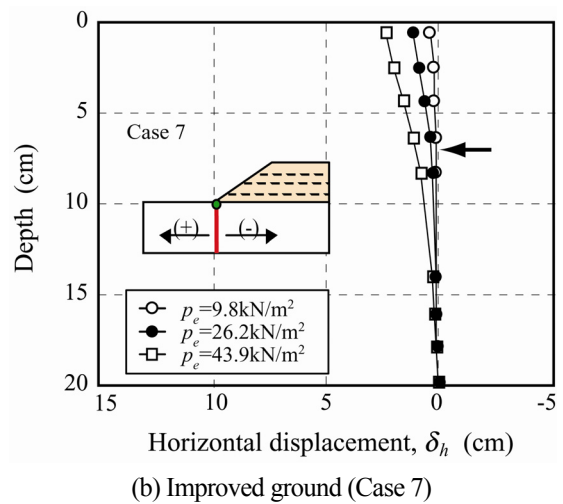
(5) Horizontal displacement distribution

In order to investigate the ground deformation in detail, the horizontal displacement distribution with depth measured at the toe of the embankment slope is shown in **Fig. 34** for the unimproved and improved ground, in which the horizontal displacement measured at various loading stages is plotted. In the unimproved ground (**Fig. 34(a)**), a relatively small displacement took place at a shallow depth at $p_e = 10.8$ kN/m^2. After that, an extremely large horizontal deformation took place with further embankment loading, especially at a shallow depth, while a small displacement took place at a deep layer. The difference in the magnitude of horizontal displacement clearly indicates that the ground failed with a slip circle failure pattern passing through the shallow layer.

In Case 7 (**Fig. 34(b)**), the improved ground, horizontal displacement at the toe of the embankment slope, corresponding to the forefront column, develops with increasing p_e, but its distribution is almost linear with depth throughout the embankment loading. In the figure, the location of the forefront column failure is also plotted as arrows. The horizontal displacement distribution is almost a linear shape even after the column fails. This phenomenon can also be seen in Case 10 (**Fig. 34(c)**), the improved ground with Th-column. The horizontal displacement at the bottom of the column is negligible. A similar displacement distribution can be seen in all the improved ground. As the front surface of the ground on which the target markers were placed corresponds to the intermediate point between the columns, the clay between the columns does not squeeze through but instead displaces together with the columns. These observations indicate that the improved area does not fail with a sliding failure pattern even after the columns fail, irrespective of the improvement width.
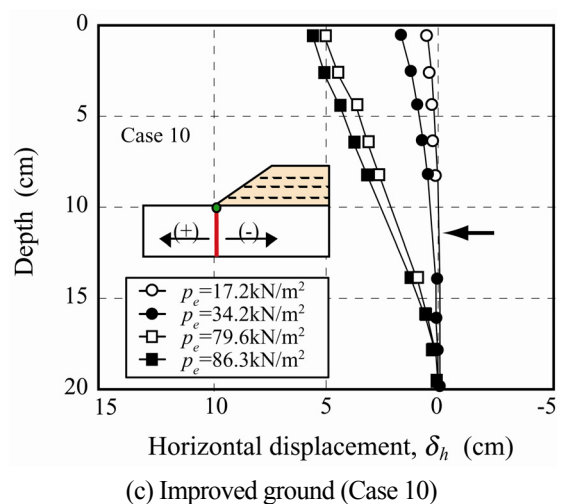
It can be concluded from **Figs. 33** and **34** that DM columns have the effect of changing the ground failure mode from slip circle failure to collapse failure.

(a) Unimproved ground (Case 1)

(b) Improved ground (Case 7)

(c) Improved ground (Case 10)

**Fig. 34**. Horizontal displacement distribution with depth

(6) Vertical stresses on top of columns

Figures 35(a) and **35(b)** show the vertical stress increment during the embankment loading, which was measured at the clay surface between the columns in Cases 7 and 10. It can be seen in the figures that the vertical stress at the clay surface monotonically increases with increasing p_e, and the magnitude of increment is almost of the same order, irrespective of column strength.

Figures 36(a) and **36(b)** show the vertical stress increment at the top of the c-line columns in Cases 7 and 10. The stress increment of the forefront and the second row column, close to the embankment edge, was quite small level during the loading, which could be due to that embankment height at the position didn't increase so much and the columns' top displaced horizontally beyond out of embankment. The comparatively small increment brings quite low stress concentration ratio which will discussed in **Fig. 37**. In the figure, the arrows beside the curves indicate the point in time of the column failure.

In Case 7, the vertical stress increased with increasing p_e and peaked in value at different embankment pressures for Tl-1c, Tl-2c and Tl-3c. As the embankment loading was terminated at a relatively low embankment pressure, Tl-4c and Tl-5c did not fail during the loading, while Tl-4b and Tl-5b failed at p_e of about 43.9 kN/m². A similar phenomenon can be seen in Case 10, where the vertical stress increment, σ_v', value at the top of the columns increased with increasing p_e and peaked at different embankment pressures depending upon the column location. The time of the peak stress does not coincide with the point in time of column failure, but instead the columns failed after the vertical stress peaked. A number of studies have been conducted on vertical stress on DM columns or sand compaction piles. Almost all the tests concluded that the decrease in vertical stress was triggered by the failure of DM columns or sand piles. However, the present study suggests that this conclusion might be incorrect.

Compared with the column strength, the vertical stress ratio at column failure is quite low, less than 0.3 for Case 7 and less than 0.1 for Case 10, which means that column failure was induced by bending moment rather than compressive stress.
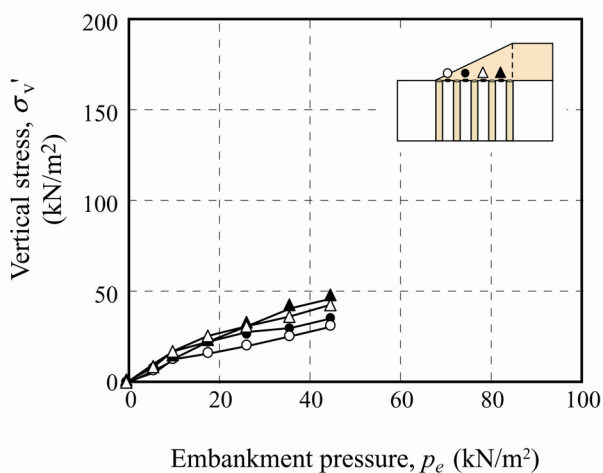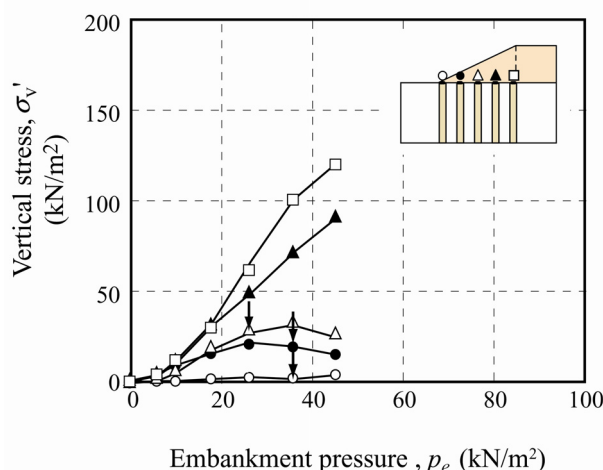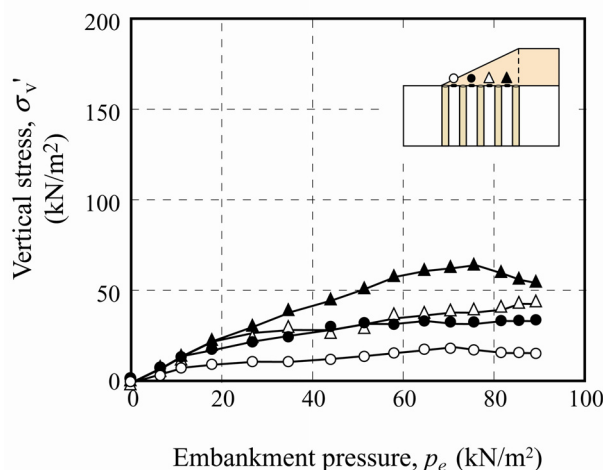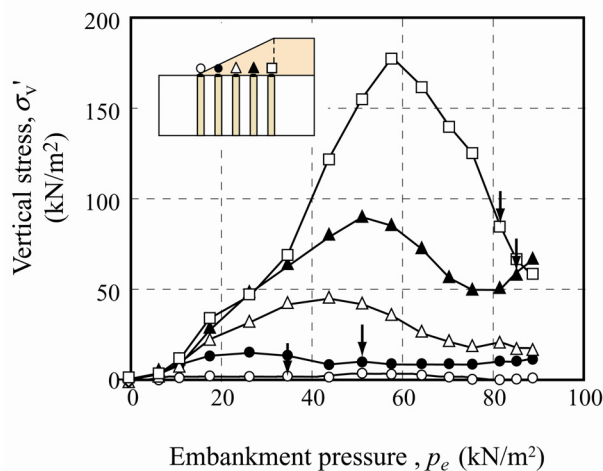

(b) Case 10

Fig. 35. Vertical stress at clay surface and embankment pressure curves

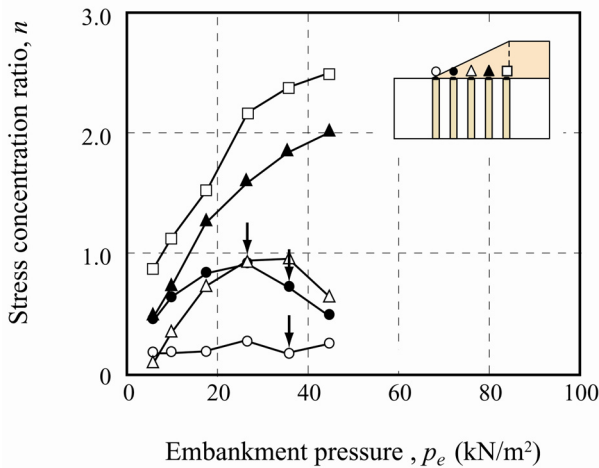

(a) Case 7

(a) Case 7

(b) Case 10

Fig. 36. Vertical stress at column top and embankment pressure curves

(7) Stress concentration ratio

It is well known that embankment pressure concentrates on the column due to its higher stiffness. **Figures 37(a)** and **37(b)** show the stress concentration ratio, n, in Cases 7 and 10, which is defined by the ratio of vertical stress increment at the top of the column against that at the clay surface between the columns. In Case 7, the n value temporally decreases at the first loading step but increases with increasing p_e and peaks in Tl-2c and Tl-3c columns. The n value of Tl-1c to Tl-3c was quite low value, lower than unity, because the stress increment at the top of column was quite low, as shown in Fig. 36. In Tl-4c and Tl-5c columns, the n value continues to increase with increasing p_e and has no peak. Although the n value varies in each column and embankment loading level, a high value is obtained at the rear side columns. In Case 10, the n value increases with increasing p_e and peaks at all the columns. The value and timing of the peak vary widely depending upon the column. Again, a high value is obtained at the rear side columns.

(a) Case 7
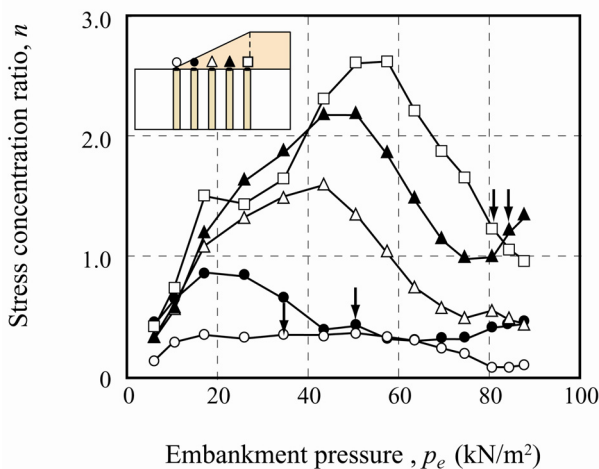
(b) Case 10

Fig. 37. Stress concentration ratio and embankment pressure curves

The magnitude of n is relatively low value less than about 2.5, irrespective of column strength. A similar phenomenon was observed in the other test cases. The n value is usually obtained by direct measurement of the stress, or back calculation of ground settlement in the field. Accumulated data shows the n value ranging from 10 to 20 (CDIT, 2002), which is considerably higher than in this study.

(8) Bending moment distribution of column

The development of the bending moment in the columns was measured in Cases 2 to 5, in which acrylic pipes were used as the model columns. The moment at three loading steps is plotted in **Figs. 38(a)** to **38(c)**. In **Fig. 38(a)**, the measured moments are plotted for Case 2 corresponding to (i) before the forefront column failure, (ii) at the forefront column failure and (iii) at the rearmost column failure in Case 9. The moments in Figs. 38(b) and 38(c) are measured in Cases 3 and 4 corresponding to the three steps in Cases 10 and 11, respectively.

In the improved ground with 3 column rows (**Fig. 38(a)**), the moment distribution before column failure, **Fig. 38(a)(i)**, increases with depth and shows a maximum value at a depth of −14 cm, irrespective of column location. A similar phenomenon can be seen at the forefront column failure, **Fig. 38(a)(ii)**. However, it is interesting that the largest bending moment developed in the rearmost column instead of in the forefront column that failed. At the rearmost column failure, **Fig. 38(a)(iii)**, the negative bending moment developed at a shallow layer in the rearmost column. In the improved ground with 5 column rows (**Fig. 38(b)**), the moment distribution before column failure, **Fig. 38(b)(i)**, increases gradually with depth and shows a maximum value at a depth of −14 cm, which is quite similar to **Fig. 38(a)(i)**. At the column failure, **Fig. 38(b)(ii)**, the bending moment that developed in the forefront column was not the largest value even when the column failed. At the rearmost column failure, **Fig. 38(b)(iii)**, a very large negative bending moment developed in the rearmost column at a depth of −6 cm. In the improved ground with 7 column rows, **Fig. 38(c)**, a large moment developed in the two forefront columns before column failure, **Fig. 38(c)(i)**. At the forefront column failure, **Fig. 38(c)(ii)**, a large positive moment developed in the three forefront columns at a deep layer, while a large negative moment developed in the rearmost column at a shallow layer. Again, it is of interest to note that the moment developed in the forefront column was not the largest even when the column failed. At the rearmost column failure, **Fig. 38(c)(iii)**, the moment that developed in the three forefront columns increased and a very large negative bending moment developed in the rearmost column.

The above results demonstrate that the column failure cannot be estimated by the magnitude of bending moment alone, but the moment distribution roughly corresponds to the column failure phenomenon especially in the forefront and rearmost columns.
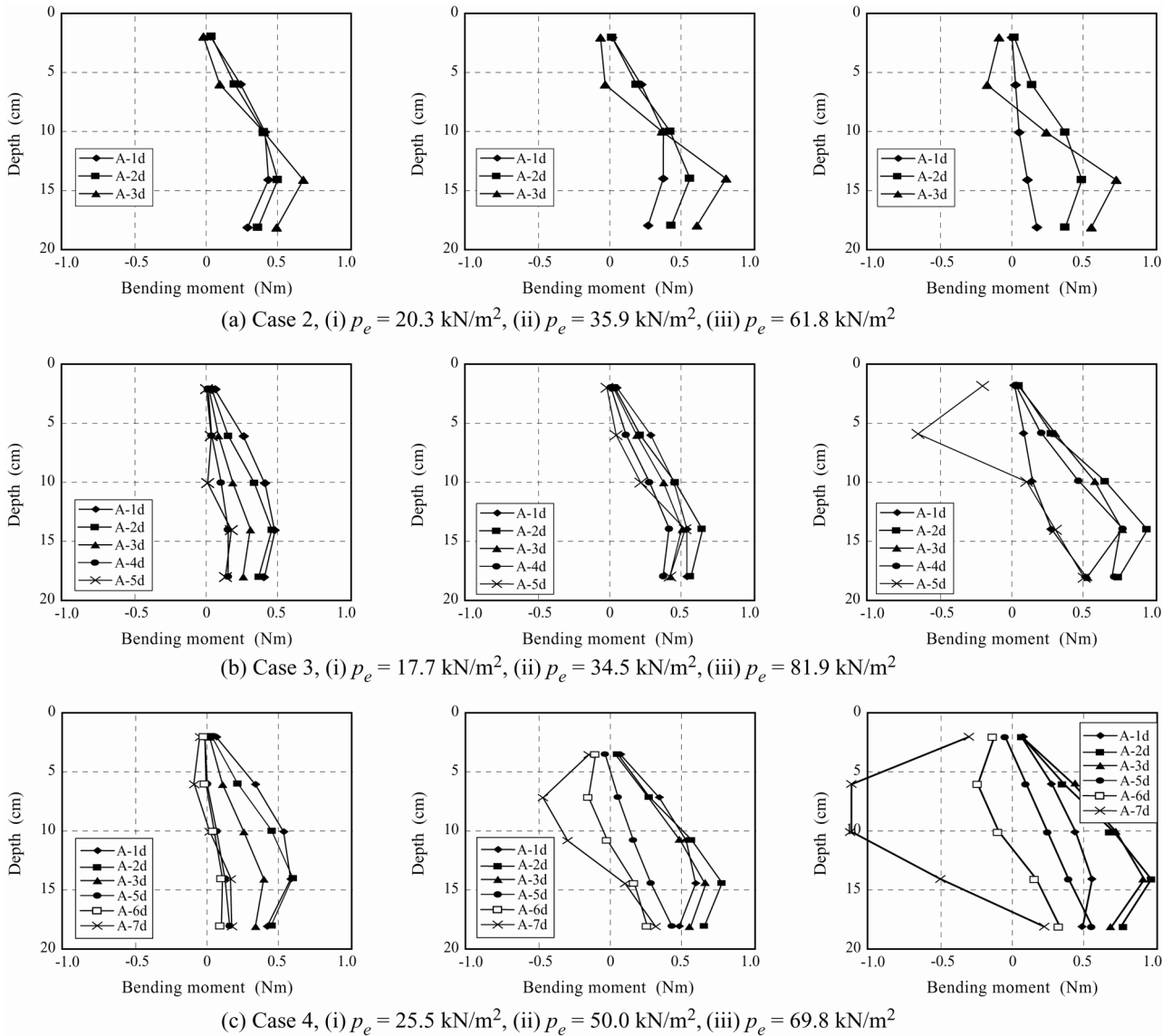
(a) Case 2, (i) p_e = 20.3 kN/m^2, (ii) p_e = 35.9 kN/m^2, (iii) p_e = 61.8 kN/m^2

(b) Case 3, (i) p_e = 17.7 kN/m^2, (ii) p_e = 34.5 kN/m^2, (iii) p_e = 81.9 kN/m^2

(c) Case 4, (i) p_e = 25.5 kN/m^2, (ii) p_e = 50.0 kN/m^2, (iii) p_e = 69.8 kN/m^2

Fig. 38. Bending moment distribution with depth

(9) Vertical stress / bending moment relationship

In order to investigate the failure criteria in detail, the relationship between bending moment and vertical stress in the model columns is plotted in **Fig. 39** for the improved ground with 3, 5 and 7 column rows. In the figure, the bending moment measured in A-columns (Cases 2 to 4) is plotted on the horizontal axis. In the figure, the measured moment is divided by the inertia to obtain the stress at the outer surface of column, σ, and then normalized with respect to the column strength, q_u. The vertical stress measured in Th-columns (Case 9 to 11) is plotted on the vertical axis, in which the vertical stress is normalized with respect to the column strength, q_u. The point in time of column failure is marked by an arrow in the figures to the corresponding stress path. The test conditions in these two test series are similar except for the column material: acrylic in Cases 2 to 4 and cement treated soil in Cases 9 to 11. Of course, the moment distribution might be influenced by the column failure in Cases 9 to 11. However, these trials can be

useful for qualitative understanding of the failure criteria of column. In the figure, two failure criteria are indicated by solid and broken lines. The solid line indicates that the compressive stress at the outer surface of the column induced by the combination of vertical stress and bending moment reaches the compressive strength, in which plus and negative value mean the counter clockwise and clockwise movements respectively. The broken line indicates that the induced tensile stress at the outer surface of column reaches the column tensile strength, σ_t.

In the improved ground with 3 column rows, **Fig. 39(a)**, all the stress paths move toward a positive moment. All the model columns failed under the combination of very low vertical stress and positive bending moment (counterclockwise direction). In the improved ground with 5 column rows, **Fig. 39(b)**, the three forefront columns show a stress path moving toward the positive moment and failure under the combination of relatively low vertical stress with positive bending moment. In the rearmost column, however, the vertical stress increases

with a very small increase in moment at the early stage of embankment loading, followed by a large increase in negative moment (clockwise direction) with decreasing vertical stress. The column failed under the combination of negative moment with vertical stress. The stress conditions under which the columns failed are close to the tensile strength criterion, which
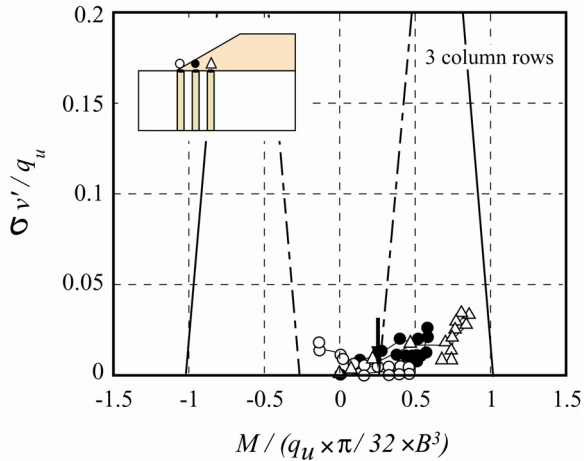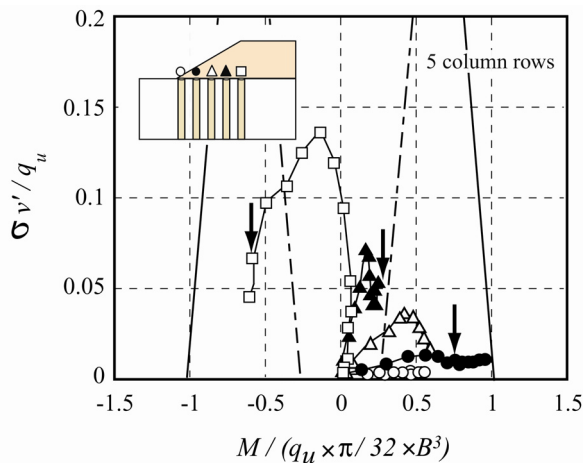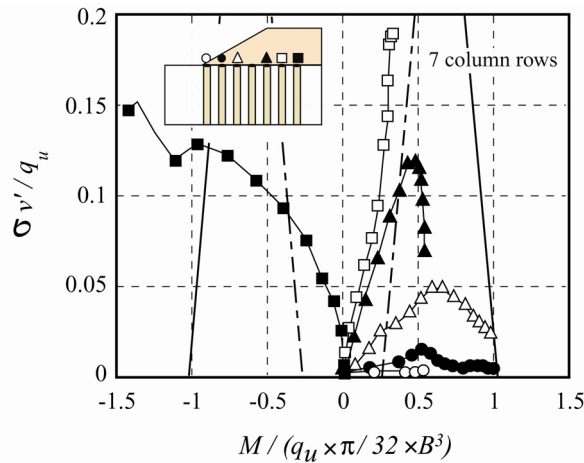
indicates that tensile stress might induce column failure. In the improved ground with 7 column rows (**Fig. 39(c)**), the two forefront columns show a stress path moving toward the positive moment and failure under the combination of relatively low vertical stress with positive moment, similar to the other cases. The rearmost column, Th-7, failed under the combination of a very large negative bending moment with relatively large vertical stress. The stress conditions under which Th-7 failed are beyond the tensile strength criterion, which indicates that compressive stress might induce column failure in Th-7. The other columns, Th-3, Th-4, Th-5 and Th-6, show a positive moment with vertical stress, but did not fail in the test.

4.2 Discussion

The following discussion on evaluation of unimproved and improved grounds are described in the prototype scale instead of the model scale.

(1) Slip circle failure for improved ground

The internal stability of DM improved ground was evaluated by the current design method first (PWRC, 2004), in which slip circle analysis with shear strength of the columns was performed. In the calculation, undrained shear strength is assumed as $q_u/2$ and fully mobilized simultaneously in all the columns. In the slip circle analysis, the embankment pressure at ground failure, $p_{ef,slip}$, is calculated by changing the embankment height until the safety factor becomes unity. The calculations are plotted in **Fig. 40** along improvement width, D, for various column strengths. The $p_{ef,slip}$ increases with increasing D, irrespective of column strength. In the figure, the model test results and the calculations with q_u values corresponding to the model tests are plotted together. It is found that the calculation overestimates the test results by about 3 to 5 times, especially in the case of high strength column, Cases 9 to 11.
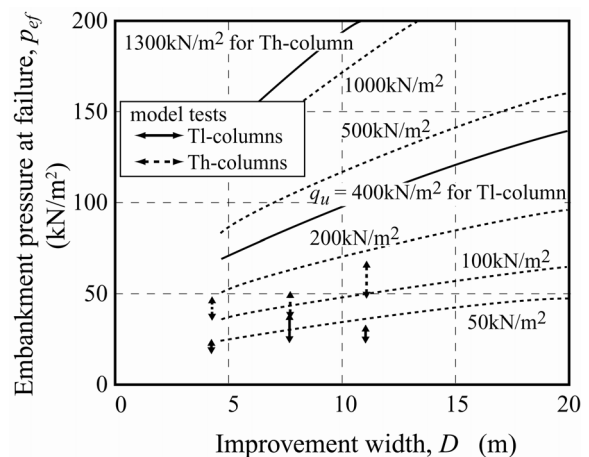

(a) Improved ground with 3 column rows

(b) Improved ground with 5 column rows

(c) Improved ground with 7 column rows

Fig. 39. Maximum bending moment and vertical stress curves

Fig. 40. Embankment pressure at ground failure and improvement width for slip circle failure

Figure 41 shows the relationship between the maximum depth of the critical slip circle, $z_{f,slip}$, and improvement width, D, which is calculated in the slip circle analysis. The $z_{f,slip}$ value increases gradually with increasing D, irrespective of column strength, but is much larger in higher column strength. In the figure, $z_{f,slip}$ values of the model tests are also plotted. Although the measured value in Case 9 differs slightly from the norm, it increases with increasing D and column strength. The calculations show larger values compared to the test results. As discussed above, the current design based on the slip circle analysis cannot reasonably evaluate the $p_{ef,slip}$ and $z_{f,slip}$ values.
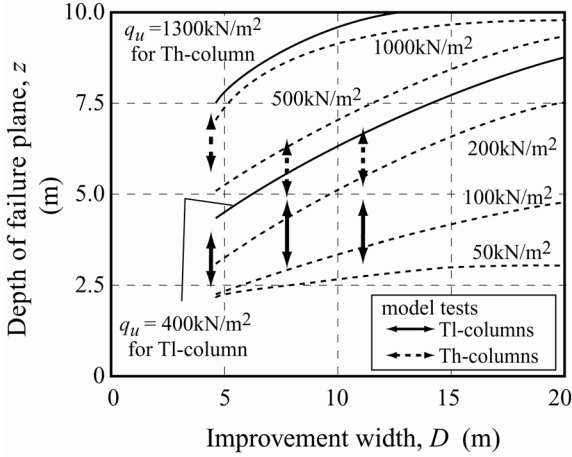
Fig. 41. Depth of failure plane and improvement width for slip circle failure

(2) Shear failure for improved ground

The internal stability of DM improved ground is evaluated by a simple calculation, in which the shear failure mode is assumed, as shown in **Fig. 42**. Full mobilization of DM column shear strength is assumed in the calculation. The formulation for the shear failure mode is expressed as Eqs. (18) to (23) for assumed depth of the shear failure plane, z, which is based on the load equilibrium of active and passive earth pressures acting on the side boundaries of the improved area and the shear strength mobilizing along the clay ground and DM columns. Rankin's theory of ultimate active and passive earth pressures are adopted in the calculation.
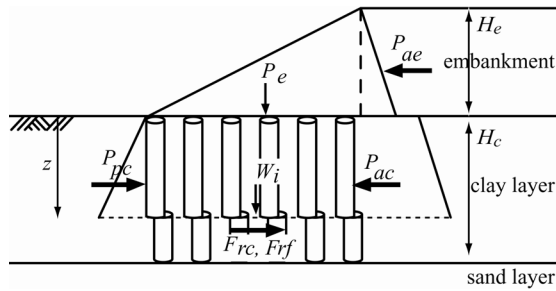

Fig. 42. Shear failure analysis

$$Fs = \frac{P_{pc} + F_{rf} + F_{rc}}{P_{ae} + P_{ac}} \tag{18}$$

$$P_{ae} = \gamma_e \cdot H_e \cdot \tan^2\left(\frac{\pi}{4} - \frac{\phi_e}{2}\right) \cdot \frac{H_e}{2} \tag{19}$$

$$P_{ac} = \left(2 \cdot \gamma_e \cdot H_e - 2 \cdot (2 \cdot c_{u0} + k \cdot z) + \gamma_c \cdot z\right) \cdot \frac{z}{2} \tag{20}$$

$$P_{pc} = \left(\gamma_c \cdot z + 2 \cdot (2 \cdot c_{u0} + k \cdot z)\right) \cdot \frac{z}{2} \tag{21}$$

$$F_{rf} = \frac{q_u}{2} \cdot a_s \cdot D \tag{22}$$

$$F_{rc} = (c_{u0} + k \cdot z) \cdot (1 - a_s) \cdot D \tag{23}$$

After substituting Eqs. (19) to (23) into Eq. (18), the following quadratic equation is obtained with respect to the embankment height, H_e, for assumed z. As the magnitude of the left-hand terms is negative when $H_e = 0$, two real number solutions are always obtained while the meaningful solution is the positive one.

$$\frac{\gamma_e}{2} \cdot \tan^2\left(\frac{\pi}{4} - \frac{\phi_e}{2}\right) \cdot H_e^2 + \gamma_e \cdot z \cdot H_e$$
$$- \left[\begin{array}{c} 2 \cdot (2 \cdot c_{u0} + k \cdot z) \cdot z \\ + \left\{\frac{q_u}{2} \cdot a_s + (c_{u0} + k \cdot z) \cdot (1 - a_s)\right\} \cdot D \end{array} \right] = 0 \tag{24}$$

The embankment pressure at ground failure, $p_{ef,shear}$ is calculated by the following equation:

$$p_{ef,shear} = \gamma_e \cdot H_{ef,shear} \tag{25}$$

Figure 43 shows the relationship between z and $p_{ef,shear}$, for $D = 7.7$ m and $a_s = 0.28$. In the figure, the relationship with various column strengths is plotted. In the case of $q_u = 50$ kN/m², the p_e value changes very slightly but shows a minimum value at $z = 3$ m. The relationship between p_e and z shows a concave shape in the case where q_u is lower than about 500 kN/m². However, when q_u equals or exceeds 500 kN/m², p_e monotonically decreases with z. The $p_{ef,shear}$ value, defined as a minimum value and shown by an arrow in the figure, increases with increasing q_u and z.

A series of similar calculations was carried out for various D values, and the relationship between $z_{f,shear}$ and D is shown in **Fig. 44** for various q_u values. The $z_{f,shear}$ value increases monotonically with increasing D, and with increasing q_u, indicating that shear failure takes place at the deep depth as D and/or q_u increases. The $z_{f,shear}$ value increases with increasing q_u, and reaches 10 m when q_u equals or exceeds 500 kN/m², which means that no column shear failure takes place. In the figure, the model test results are plotted together. The calculations give much larger $z_{f,shear}$ values compared to the tests.
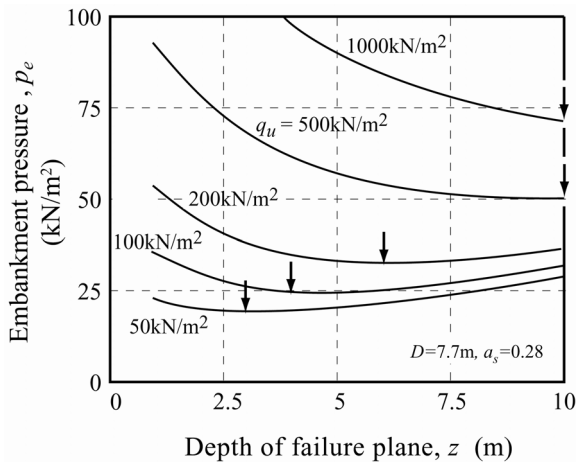
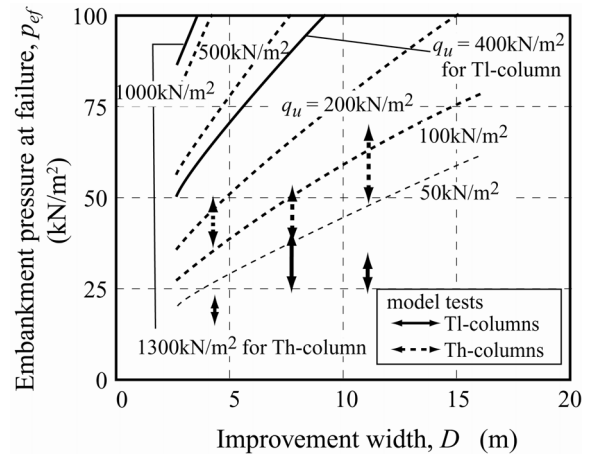**Fig. 43**. Assumed depth of failure plane and embankment pressure for shear failure mode

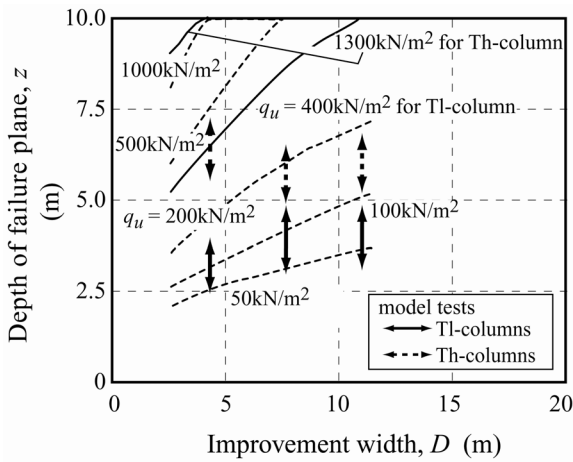**Fig. 45**. Embankment pressure at ground failure and improvement width for shear failure mode

Fig. 44. Depth of failure plane and improvement width for shear failure mode

Fig. 46. Resistance force components for shear failure mode

The $p_{ef,shear}$ is defined as the minimum value for each case, and is shown along D in **Fig. 45**. The figure shows that $p_{ef,shear}$ increases with increasing D and/or q_u. The model test results are also plotted in the figure. In comparison with the model test results, the calculated $p_{ef,shear}$ values are considerably higher. The overestimation is quite dominant as D increases.

In order to investigate the cause of overestimation in detail, the resistance force components in the calculation are shown in **Fig. 46**. The passive earth pressure component of resistance force, P_{pc}, increases with increasing q_u, which is due to the increase of $z_{f,shear}$. When the column strength becomes 1300 kN/m^2 (Cases 9 to 11), P_{pc} becomes constant, irrespective of D. The column strength component, F_{rf}, has a dominant role in the entire resistance load throughout D. Its degree increases with increasing q_u, and reaches about 65% of the entire resistance force in Case 11. According to **Fig. 45**, the column strength should be underestimated to the unrealistic value of 1/8 to 1/10 to evaluate the test results accurately.
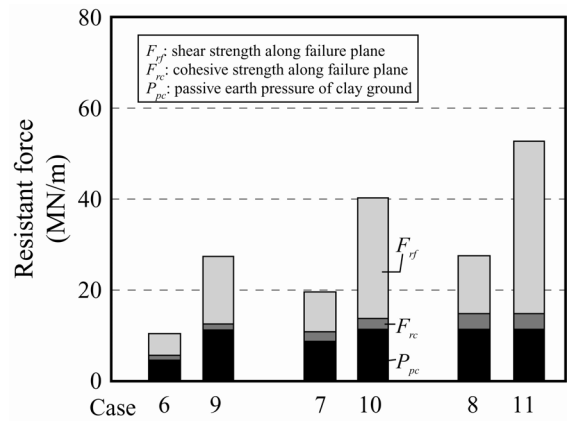
The magnitude and shape of the passive earth pressure distribution are greatly influenced by many factors such as adhesion of the retaining wall, movement of the wall, etc., which have not yet been clarified despite numerous research efforts made over the years. **Figures 47(a)** and **47(b)** show the effect of the mobilization degree of passive earth pressure on $p_{ef,shear}$ and $z_{f,shear}$. In **Fig. 47(a)**, the $p_{ef,shear}$ value decreases with decreasing mobilization degree, but still overestimates the model tests even when the degree decreases to 25% of the initial value. As the mobilization degree decreases, the $z_{f,shear}$ value increases due to the increasing relative column strength, as shown in **Fig. 47(b)**. This causes further discrepancy with the model tests.

According to the parametric calculations, the overestimation by the shear failure mode cannot be explained by the accuracy of soil parameters, but should be explained by the difference of failure pattern: shear failure pattern instead of bending failure pattern is assumed in the current design method.
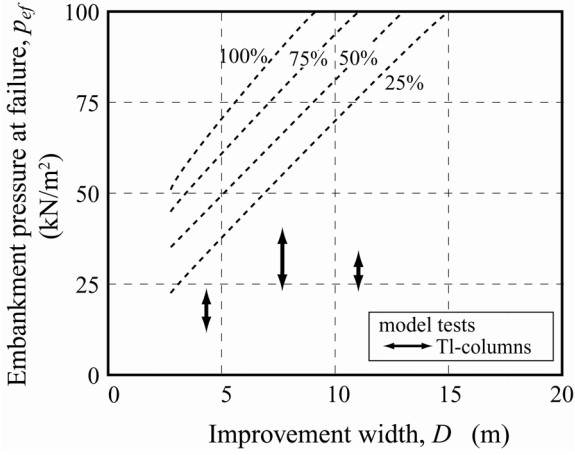
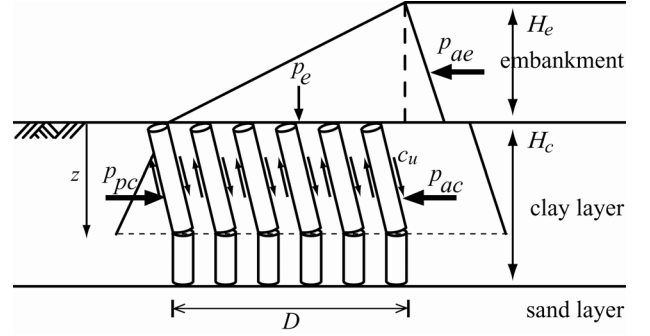(a) Embankment pressure at ground failure and improvement width
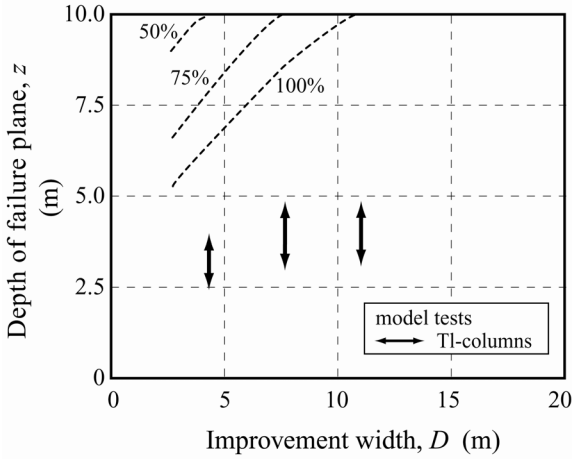
(b) Depth of failure plane and improvement width

Fig. 47. Effect of passive earth pressure mobilization degree on stability for shear failure mode

(3) Bending failure for improved ground

Here, a simple stability calculation is proposed. In the calculation, all the DM columns are assumed to fail simultaneously in bending failure mode and the improved area above a failure plane is assumed to deform as a simple shear, schematically shown in **Fig. 48**. However, the assumption of full mobilization of bending strength does not correspond to the model test results where the columns fail one by one. As described before, the DM columns are subjected to not only the bending moment but also the axial stress due to embankment loading. In the calculation, the columns are assumed to fail when the induced tensile stress reaches the ultimate bending strength, $\sigma_b = \alpha \, q_u$, as shown in **Fig. 49**, where α value is assumed as 0.28 according to **Fig. 9**. For the calculation, the moment equilibrium at the assumed failure plane, z, is analyzed as follows:

Fig. 48. Bending failure analysis
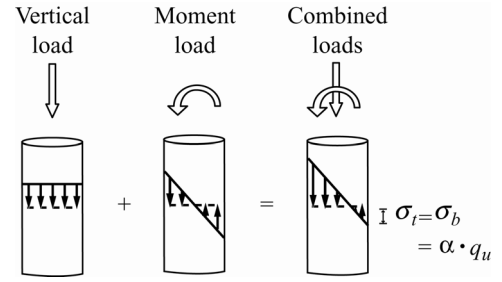
Fig. 49. Induced stress condition in DM column

The driving moments by the active earth pressure of the embankment, M_{ae}, and of the clay ground, M_{ac}, are expressed as Eqs. (26) and (27), respectively, where Rankin's theory on earth pressure is assumed.

$$M_{ae} = \gamma_e \cdot H_e \cdot \tan^2\left(\frac{\pi}{4} - \frac{\phi_e}{2}\right) \cdot \frac{H_e^2 + 3 \cdot H_e \cdot z}{6} \tag{25}$$

$$M_{ac} = \frac{z^2}{6} \cdot \left(3 \cdot \gamma_e \cdot H_e + \gamma_c \cdot z - 6 \cdot c_{u0} - 2 \cdot k \cdot z\right) \tag{26}$$

Similar to the shear failure calculation, the embankment shape is assumed as a trapezoid extending from the forefront to the rearmost DM column as shown in **Fig. 48**, for ease of parametric calculations. The resistance moment per unit breadth by the adhesion mobilizing on the side surface of DM columns, M_{rc}, by the weight of DM columns, M_{rt}, by the weight of embankment on DM columns, M_{re}, by the shear strength of clay between DM columns, M_{sc}, by the passive earth pressure of clay ground, M_{pc}, and by the bending failure of DM columns, M_{pb}, are expressed as Eqs. (28) to (33), respectively.

$$M_{rc} = B^2 \cdot z \cdot \frac{2 \cdot c_{u0} + k \cdot z}{2} \cdot N \cdot \frac{1}{S} \tag{28}$$

$$M_{rt} = \frac{\pi}{8} B^3 \cdot z \cdot \gamma_t \cdot N \cdot \frac{1}{S} \tag{29}$$

$$M_{re} = \frac{\pi}{8} B^3 \cdot H_e \cdot \gamma_e \cdot \frac{n}{1 + (n-1) \cdot a_s} \cdot N \cdot \frac{1}{S} \tag{30}$$
$$= \frac{\pi}{8} B^3 \cdot H_e \cdot \gamma_e \cdot \mu_s \cdot N \cdot \frac{1}{S}$$

$$M_{sc} = S \cdot (1 - a_s) \cdot \frac{2 \cdot c_{u0} + k \cdot z}{2} \cdot (N - 1) \cdot z \qquad (31)$$

$$M_{pc} = \frac{z^2}{6} \cdot (\gamma_c \cdot z + 4 \cdot c_{u0} + 2 \cdot k \cdot z) \qquad (32)$$

$$M_{pb} = \frac{\pi}{32} \cdot B^3 \cdot \sigma_b \cdot N \cdot \frac{1}{S}$$

$$= \frac{\pi}{32} \cdot B^3 \cdot \alpha \cdot q_u \cdot N \cdot \frac{1}{S} \qquad (33)$$

According to the moment equilibrium at the failure plane, the following equation can be satisfied:

$$M_{ae} + M_{ac} = M_{rc} + M_{rt} + M_{re} + M_{sc} + M_{pc} + M_{pb} \qquad (34)$$

After substituting Eqs. (28) to (33) into Eq. (34) and expanding the equation, the following cubic equation is obtained with respect to the embankment height, H_e.

$$-\frac{\gamma_e}{6} \cdot \tan(\frac{\pi}{4} - \frac{\phi_e}{2}) \cdot H_e^3 - \frac{\gamma_e}{2} \cdot \tan(\frac{\pi}{4} - \frac{\phi_e}{2}) \cdot z \cdot H_e^2$$

$$+ \{D \cdot (\frac{4}{\pi} \cdot a_s \cdot \frac{2 \cdot c_{u0} + k \cdot z}{2} + \frac{1}{2} \cdot a_s \cdot B \cdot \gamma_e \cdot \mu_s \cdot \frac{1}{S}$$

$$- (1 - a_s) \cdot \frac{2 \cdot c_{u0} + k \cdot z}{2}) - \frac{z^2}{2} \cdot \gamma_e \cdot \frac{1}{S} \} \cdot H_e$$

$$+ \{a_s \cdot B \cdot z \cdot \gamma_t \cdot \frac{1}{S} + \frac{z^2}{3} \cdot (6 \cdot c_{u0} + 2 \cdot k \cdot z)$$

$$\qquad\qquad\qquad\qquad\qquad\qquad\qquad (35)$$

$$+ \frac{\pi}{32} \cdot B^3 \cdot \alpha \cdot q_u \cdot N \cdot \frac{1}{S} \} = 0$$

Three solutions, either three real numbers or one real and two imaginary numbers, are obtained by Cardano's formula. The meaningful solution for this study should be a real number and positive value. As there are many variables in the equation, a solution, $H_{ef,bending}$, is numerically calculated for specific ground conditions and assumed bending failure plane, z. The embankment pressure at ground failure, $p_{ef,bending}$ is similarly calculated by Eq. (8).
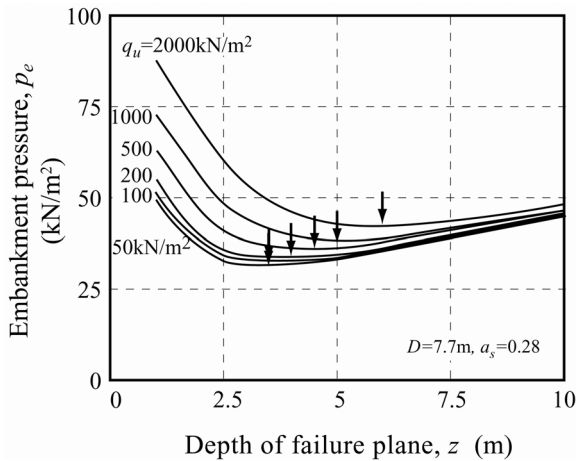

Fig. 50. Assumed depth of failure plane and embankment pressure for bending failure mode

Figure 50 shows the relationship between assumed depth of bending failure plane, z, and p_e for $D = 7.7$ m and $a_s = 0.28$. The relationship for various column strengths is plotted in the figure and shows a concave shape, irrespective of the q_u value. The $z_{f,bending}$ giving $p_{ef,bending}$, as shown by an arrow, increases slightly with increasing q_u. It can be seen that $p_{ef,bending}$ also increases slightly with increasing q_u.

A series of calculations was carried out for different improvement widths and column strengths, and the relationship between D and $z_{f,bending}$ is shown in **Fig. 51** for various q_u values. The z_f value increases monotonically with increasing D, and with increasing q_u. However, the effect of q_u is not so dominant compared to that in the shear failure pattern in **Fig. 44**. In the figure, the model test results are also plotted. The calculation gives a reasonable estimation of the depth of failure plane, slightly overestimated compared to the model tests for Cases 6 to 8, but underestimated for Cases 9 to 11.
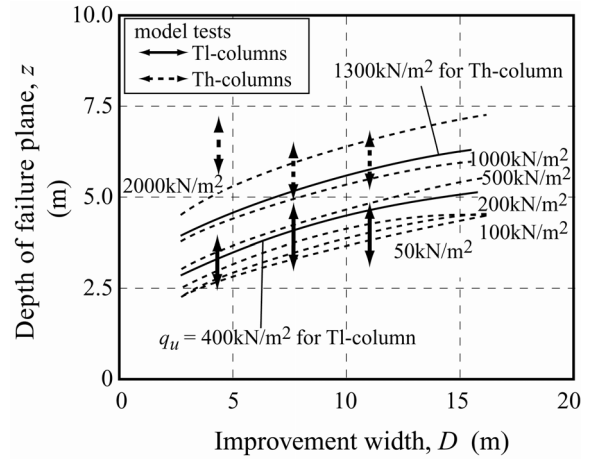

Fig. 51. Depth of failure plane and improvement width for bending failure mode

The $p_{ef,bending}$ value, shown along D in **Fig. 52**, increases with increasing D and q_u. However, the effect of q_u is relatively small. The model test results are also plotted in the figure. The calculations give a reasonable estimation compared to the model tests.

The resistance moment components for the bending failure mode, shown in **Fig.53**, are calculated by the proposed calculation. The passive earth pressure component of the resistance moment, M_{pc}, increases with increasing q_u due to increasing $z_{f,bending}$. The passive earth pressure component, M_{pc}, has a dominant role in the entire resistance load throughout D. Its degree increases with decreasing D and with increasing q_u. The component of the clay strength between the columns, M_{sc}, also has a dominant role. However, the column strength component, M_{pb}, has a relatively small role of about 10 to 15% of the whole resistance, which is quite a different phenomenon from the shear failure pattern as shown in **Fig. 46**. This indicates that the accuracy of evaluating $p_{ef,bending}$ is dominantly governed by the accuracy of estimating the passive earth pressure.
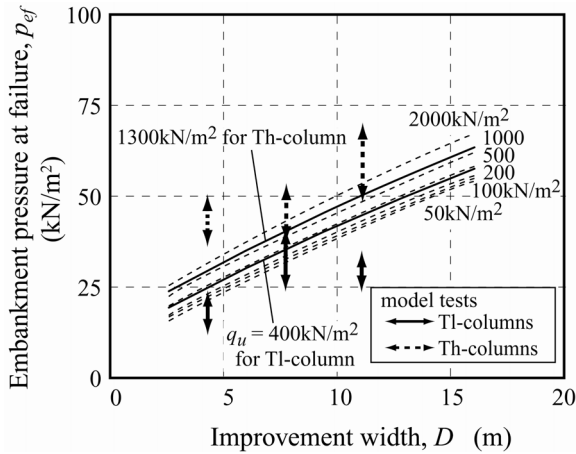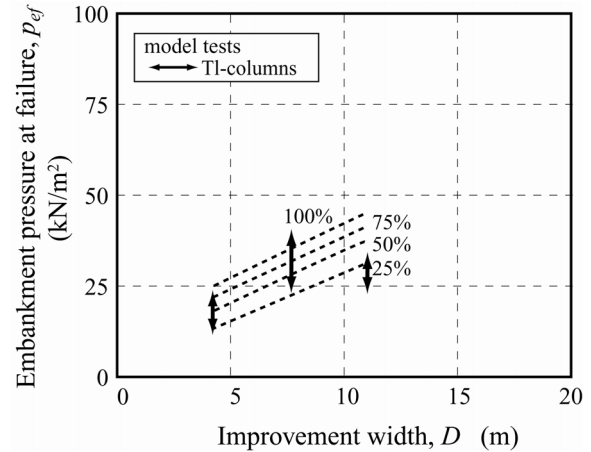
Fig. 52. Embankment pressure at ground failure and improvement width for bending failure mode

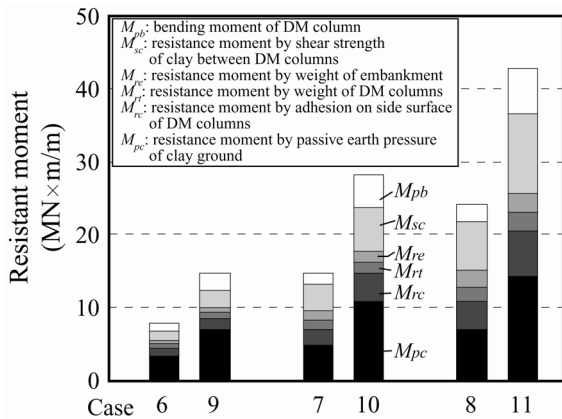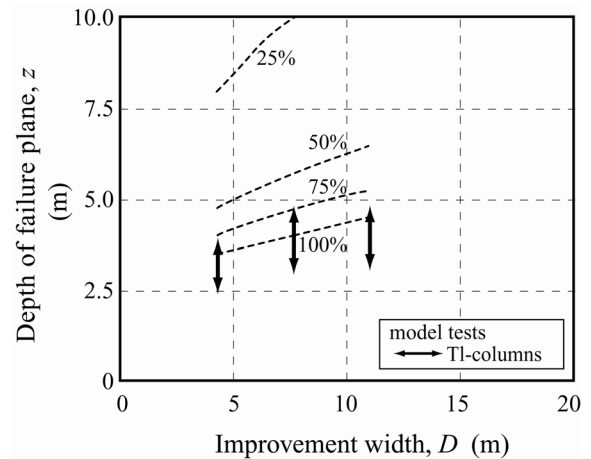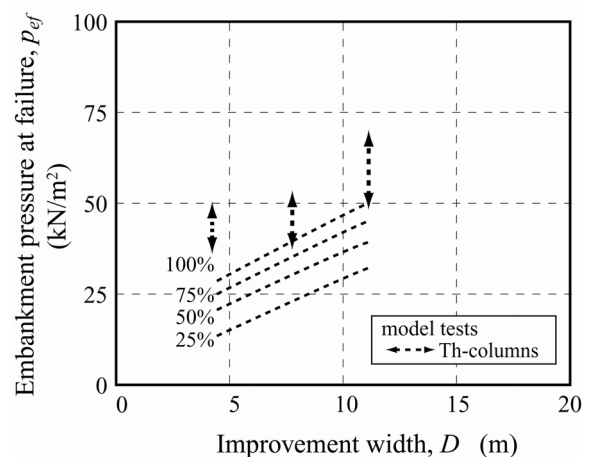(a) Embankment pressure at ground failure and improvement width
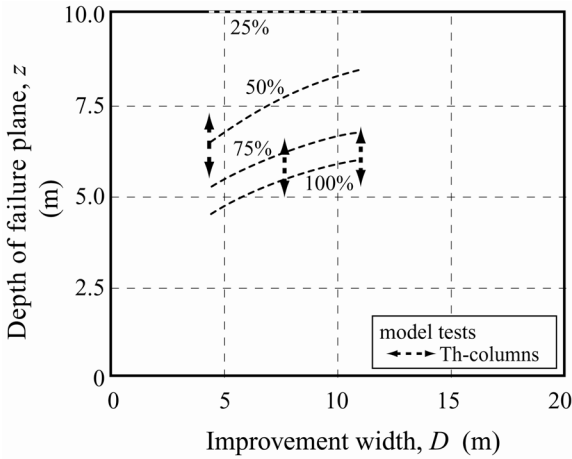

Fig. 53. Resistant moment components for bending failure mod

(b) Depth of failure plane and improvement width

Fig. 54. Effect of passive earth pressure mobilization degree for Cases 6 to 8

(a) Embankment pressure at ground failure and improvement width

The effect of passive earth pressure on $p_{ef,bending}$ is studied next. **Figures 54** and **55** show the effect of the passive earth pressure mobilization degree on $p_{ef,bending}$ and $z_{f,bending}$ for the improved ground with Tl- and Th-columns, respectively. In the calculation, the mobilization degree is changed to 75%, 50%, and 25% while its distribution shape is kept constant as a triangle. In can be seen in **Figs. 54(a)** and **55(a)** that the $p_{ef,bending}$ value decreases at about the same magnitude with decreasing the mobilization degree. In the case of Tl-column, **Fig. 54(a)**, the calculated $p_{ef,bending}$ value can be reasonably coincided with the model tests when the mobilization degree is about 25 to 75%. In **Fig. 54(b)**, the relationship between D and $z_{f,bending}$ is plotted, showing that the calculated $z_{f,bending}$ increases with decreasing passive earth pressure mobilization degree. A mobilization degree of about 100% gives a reasonable estimation compared to the model tests throughout of D. In the case of Th-column, **Fig. 55(a)**, on the other hand, the calculation underestimates the test data even the mobilization degree of 100%. the calculated $z_{f,bending}$ for Th-column, in **Fig. 55(b)** shows the mobilization degree of about 50 to 100% gives a reasonable estimation to the model tests.
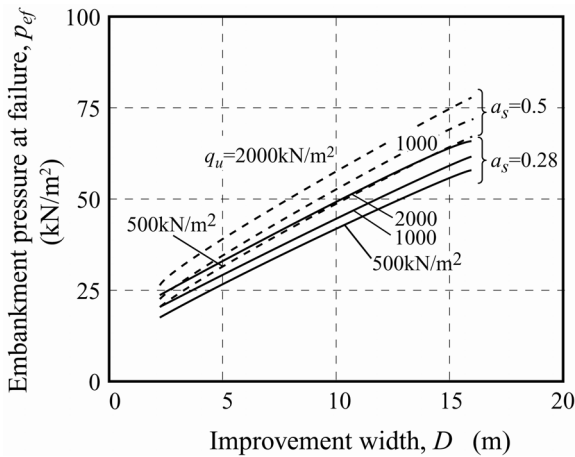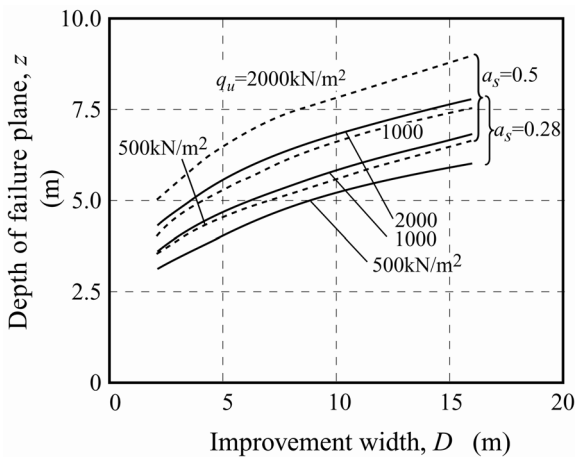
(b) Depth of failure plane and improvement width

Fig. 55. Effect of passive earth pressure mobilization degree

(4) Effect of improvement area ratio

Here, the effect of improvement area ratio on the stability is addressed. **Figure 56** shows the relationship between

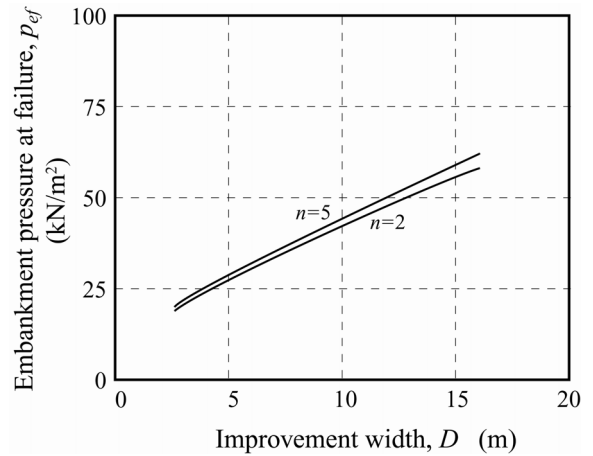(a) Embankment pressure at ground failure and improvement width

(b) Depth of failure plane and improvement width

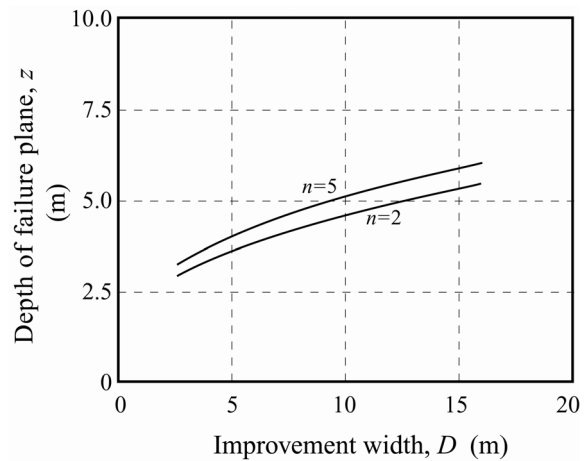**Fig. 56**. Effect of improvement area ratio for bending failure mode

$p_{ef,bending}$ and $z_{f,bending}$ and D, which is calculated for various column strengths. In can be seen that $p_{ef,bending}$ increases monotonically with increasing D, irrespective of a_s. The magnitude of $p_{ef,bending}$ in $a_s = 0.5$ is about 24% higher than that in $a_s = 0.28$. The effect on $z_{f,bending}$ (**Fig. 56(b)**), is not as large: the magnitude of $z_{f,bending}$ in $a_s = 0.5$ is about 20% higher than that in $a_s = 0.28$.

(5) Effect of stress concentration ratio

The calculated $p_{ef,bending}$ and $z_{f,bending}$ values for $n = 2$ and 5 are plotted in **Fig. 57** along D. The $p_{ef,bending}$ and $z_{f,bending}$ values increase with increasing stress concentration ratio, n, but the effect is quite small.

(a) Embankment pressure at ground failure and improvement width

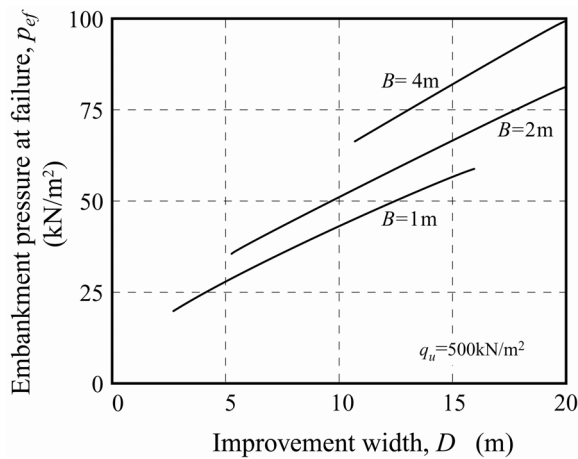(b) Depth of failure plane and improvement width

Fig. 57. Effect of improvement area ratio for bending failure mode
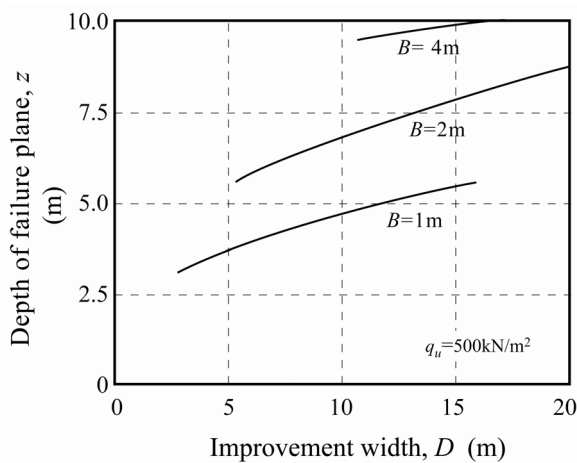
(6) Effect of DM column diameter

The effect of the DM column diameter, B, on internal stability is addressed in this section. **Figure 58(a)** shows the relationship between $p_{ef,bending}$ and D for $q_u = 500$ kN/m² with various B values. The $p_{ef,bending}$ value increases almost linearly with increasing D, irrespective of B. Comparing the effect of

column strength as shown in **Fig. 52**, the improvement effect of column diameter is greater on $p_{ef,bending}$ than the effect of column strength. However, the embankment pressure increases more rapidly with increasing B. According to Eqs. (28) to (33), M_{rc} increases with the power of two and M_{rt}, M_{re} and M_{pb} increase with the power of three with increasing B. These increases in the resistance moment bring about the embankment pressure increase with increasing DM column diameter. By increasing the column diameter, the depth of failure plane, $z_{f,bending}$, increases, as shown in **Fig. 58(b)**.

As the DM column diameter is dependent upon the machine and is about 1.0–1.5 m in Japan (CDIT, 2002), the calculation for D exceeding 2 m is not realistic. However, it becomes realistic when the columns are overlapped to create treated soil mass having a relatively large sectional area. According to literatures (e.g. Rathmayer, 1996), honeycomb type and wall type improved ground are proposed for improving the stability of embankment slope, where DM columns are overlapped. The calculation results confirm that such improved ground can considerably improve the internal stability.

(a) Embankment pressure at ground failure and improvement width

(b) Depth of failure plane and improvement width
Fig. 58. Effect of DM column diameter
for bending failure mode

4.4 Summary

The failure pattern of group column type DM improved ground subjected to embankment loading was investigated through a series of centrifuge model tests and a simple calculation. The major conclusions derived in this study are as follows:

1) The embankment pressure monotonically increases with increasing ground displacement without peaking even after many DM columns fail.

2) The embankment pressure at ground failure, which is defined as the forefront column failure, increases gradually with increasing improvement width.

3) The DM columns do not fail simultaneously but instead fail one by one in sequence from the forefront column toward the rearmost column in the case of small improvement width. When the improvement width becomes large, the forefront column fails first and then the second and third row columns fail. However, the rearmost column then fails due to large ground settlement.

4) The current design method cannot reasonably evaluate the embankment pressure and the depth of failure plane at ground failure of the model test results because a shear failure mode is assumed instead of a bending failure mode for the columns. The overestimation cannot be explained by estimating the accuracy of soil parameters.

5) A simple calculation based on the bending failure mode of the columns has relatively high applicability for evaluating the internal stability of the group column type improved ground.

6) The improvement area ratio has a dominant effect on the internal stability of the improved ground. The increasing DM column diameter has the effect of improving the internal stability of improved ground. The overlapping of DM columns is effective for increasing the internal stability.

7) The importance of simulating a suitable failure pattern of improved ground is demonstrated for accurately evaluating the internal stability.

5. EVALUATION OF STABILITY

5.1 Failure modes assumed in the current design method

In the current design method, two failure modes are assumed: sliding failure mode in external stability and slip circle failure mode in internal stability (PWRC, 2004), as shown in **Figs. 1(a)** and **1(b)**.

(1) Sliding failure mode

In the sliding failure mode, as shown in **Fig. 1(a)**, the DM columns and the clay between are assumed to show horizontal displacement on a stiff layer without any rearrangement of columns. The formulation for the failure mode is expressed as Eq. (36), which is based on the horizontal load equilibrium of active and passive earth pressures acting on the side boundaries of the improved area and the shear strength mobilizing at the bottom of the improved area. .

$$F_{S,sliding} = \frac{P_{pc} + \min\left[F_{rf}, F_{rt}\right] + F_{rc}}{P_{ae} + P_{ac}} \tag{36}$$

(2) Slip circle failure mode

In the slip circle failure mode, as shown in **Fig. 1(b)**, the improved ground consisted of the DM columns and the clay layer is assumed as a composite ground and to fail with circle shaped failure plane. The stability is evaluated by the slip circle analysis with an average shear strength of the improved ground, and the formulation is expressed as Eq. (37).

$$F_{s,slip\ circle} = \frac{M_r}{M_d} \tag{37}$$

5.2 Failure modes assumed in the proposed design method

According to the discussion in the previous sections, three more failure modes were proposed: collapse failure mode in external stability and shear failure and bending failure modes in internal stability, as shown in **Figs. 2(a)** to **2(c)**.

(1) Collapse failure mode

In the collapse failure mode, the DM columns and the clay between are assumed to deform as a simple shear as shown in **Fig. 2(a)** due to the imbalance between active and passive earth pressures acting on the side boundaries of the improved area. The formulation for the failure mode is expressed as Eq. (38), which is derived based on the moment equilibrium at the bottom of the columns.

$$F_{s,collapse} = \frac{M_{rc} + M_{rt} + M_{re} + M_{sc} + M_{pc}}{M_{ae} + M_{ac}} \tag{38}$$

(2) Shear failure mode

In the shear failure mode, the DM columns and the clay between are assumed to be sheared along a horizontal plane, as shown in **Fig. 2(b)**. The formulation for the failure mode is expressed as Eq. (39) for assumed depth of shear failure plane, z, which is based on the load equilibrium of active and passive earth pressures acting on the side boundaries of the improved area and the shear strength mobilizing along the clay ground and DM columns.

$$F_{s,shear} = \frac{P_{pc} + F_{rf} + F_{rc}}{P_{ae} + P_{ac}} \tag{39}$$

(3) Bending failure mode

In the bending failure mode, the improved area above an assumed failure plane are assumed to deform as a simple shear, as schematically shown in **Fig. 2(c)**. The formulation for the failure mode is expressed as Eq. (40), based on the moment equilibrium at the assumed failure plane, z.

$$F_{s,bending} = \frac{M_{rc} + M_{rt} + M_{re} + M_{sc} + M_{pc} + M_{pb}}{M_{ae} + M_{ac}} \tag{40}$$

5.3 Characteristics of current design method

(1) Ground condition studied

A trapezoid shape embankment on the column type DMM ground is studied for the current design procedure and the proposed procedure, as shown in **Fig. 59**. The ground condition here is referenced in the design manual on DMM (PWRC, 2004). The soil properties of the embankment, clay layer and sand layer are summarized in **Table 4**.
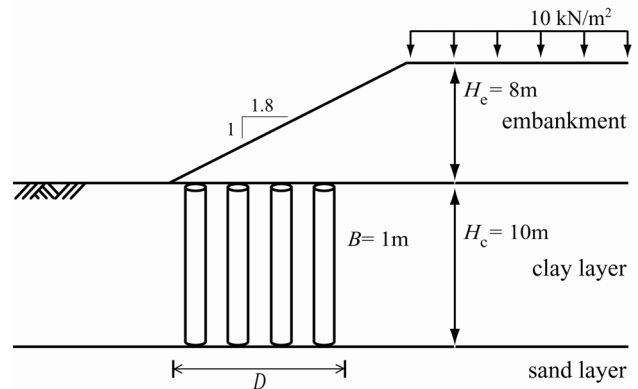

Fig. 59. Ground condition studied

Table 4. Soil properties of ground

Embankment	
Unit weight, γ	14 kN/m^3
Internal friction angle, ϕ	30
Clay layer	
Unit weight, γ	4 kN/m^3
Shear strength profile	10 + 1.5 z kN/m^2
Strength increment ratio, c_u/p	0.3
Sand layer	
Unit weight, γ	9 kN/m^3
Internal friction angle, ϕ	35
DM column	
Unit weight, γ	9 kN/m^3
Diameter, B	1 m
Strength ratio, σ_b/q_u	0.28
Improvement area ratio, a_s	50%

(2) Characteristics of slip circle analysis

A series of slip circle analyses was carried out to investigate the effect of column strength, $q_{u,column}$, and the improvement width, D, for the improvement area ratio, a_s, of 50%. The calculated safety factor, $F_{s,slip\ circle}$, is plotted along D in **Fig. 60(a)**. In the case of $q_{u,column}$ of 50 kN/m^2, $F_{s,slip\ circle}$ increases slightly with increasing D and reaches a constant value at D of about 25 m. A similar phenomenon can be seen in the case of $q_{u,column}$ of 100 and 200 kN/m^2; however, the increasing ratio rises as $q_{u,column}$ increases. In the case of $q_{u,column}$ of 500 kN/m^2, on the other hand, $F_{s,slip\ circle}$ climbs very quickly at D of about 2 m, and then increases gradually with increasing D to a constant value at D of about 35 m. The same relationship is found in the case of $q_{u,column}$ higher than 500 kN/m^2.

The depth of failure plane, $z_{f,slip\ circle}$, where the slip circle passes, is plotted in **Fig. 60(b)** for various $q_{u,column}$ values. The $z_{f,slip\ circle}$ for $q_{u,column}$ of 50 kN/m^2 increases linearly with increasing D to a constant value of 7.4 m,
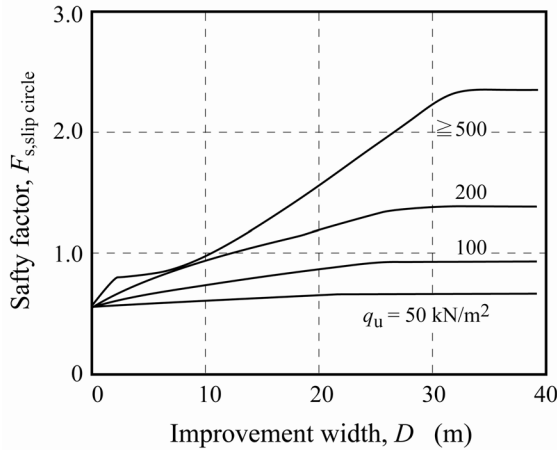
(a) Improvement width and $F_{s,slip\ circle}$
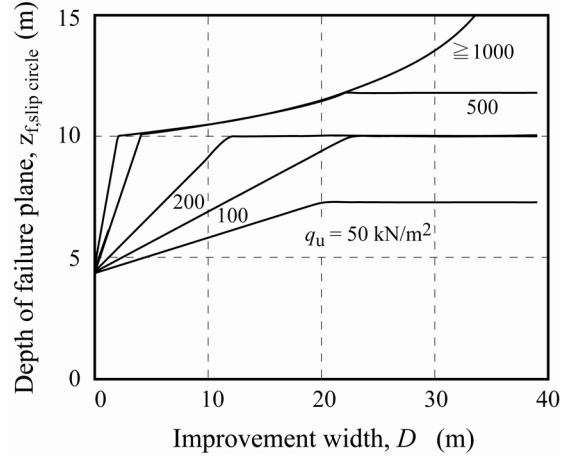
(b) Improvement width and depth of failure plane
Fig. 60. Slip circle analyses (a_s of 50%)

which means that the slip circle always passes through the improved area. A similar phenomenon can be seen in the case of $q_{u,column}$ of 100 and 200 kN/m^2, while the slip circle passes underneath the improved area for a large D value. In the case of $q_{u,column}$ of 500 kN/m^2 or higher, $z_{f,slip\ circle}$ continuously increases with increasing D, which indicates that the size of slip circle increases with increasing D and passes underneath the improved area.

Other slip circle calculations were carried out changing a_s and $q_{u,column}$, and the calculation results for D of 10 m are plotted in **Fig. 61**. In the figure, the average undrained shear strength of the improved area at its bottom, $c_{u,ave.}$, defined as Eq. (41), is plotted on the horizontal axis.

$$c_{u,ave.} = a_s \cdot \frac{q_{u,column}}{2} + (1 - a_s) \cdot c_{u,clay} \qquad (41)$$

$F_{s,slip\ circle}$ almost coincides and increases with increasing $c_{u,ave.}$ to a constant value at $c_{u,ave.}$ of about 150 kN/m^2 irrespective of the combination of a_s and $q_{u,column}$. This value is almost of the same order as the shear strength mobilized in the bottom sand layer, $\sigma_v * tan\ \phi_s$, where σ_v is the vertical stress on the sand layer and ϕ_s is the internal friction angle of the sand layer. This clearly shows that the slip circle passes through the improved area as long as the average shear strength of the improved area is lower than the shear strength mobilized in the sand layer. The column strength in the field is highly dependent upon the type and amount of binder to be mixed with the soil. The general Japanese practice is to set the design column strength at 400 to 500 kN/m^2 to assure uniformity in column strength. The magnitude of a_s is usually set at 50% or higher. As $c_{u,ave.}$ is about 200 kN/m^2 or higher, it can be concluded that the slip circle does not pass through the improved area but rather through the sand layer under practical conditions. This indicates that the slip circle analysis in the current design procedure for evaluating internal stability practically evaluates the sliding failure mode in the external

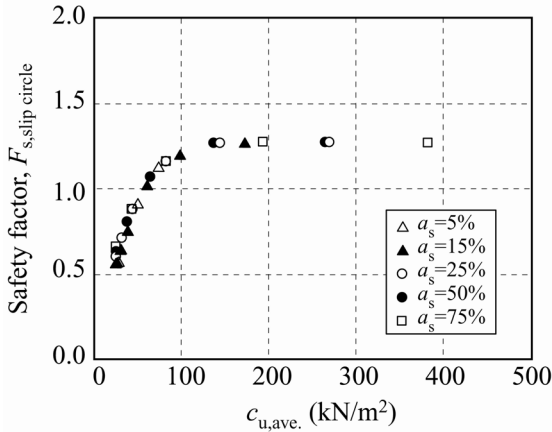stability. In many cases, column strength is not determined by the slip circle analysis.

Fig. 61. Average shear strength and $F_{s,\text{slip circle}}$ relation

5.4 Characteristics of sliding, collapse, shear and bending failure modes and comparison to slip circle Analysis

In investigating the sliding, collapse, shear and bending failure modes, the active earth pressure of the embankment is calculated by the Coulomb theory in which the maximum earth pressure is obtained by changing the assumed slip line passing through the embankment, as shown in **Fig. 62**. The active earth pressure of the clay layer is calculated by the Rankin theory with the mean overburden pressure of one at the right edge of improved area and one far from improved area. The passive earth pressure of the clay layer is calculated by the Rankin theory. Here, four parameters, column strength, improvement area ratio, diameter of column and stress concentration ratio, on the stability of the improved ground are investigated.
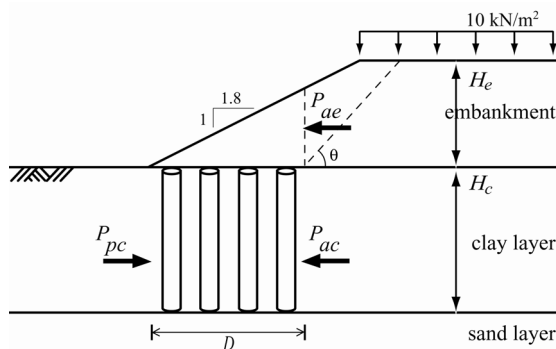

Fig. 62. Earth pressure calculation for sliding, collapse, shear and bending failure modes
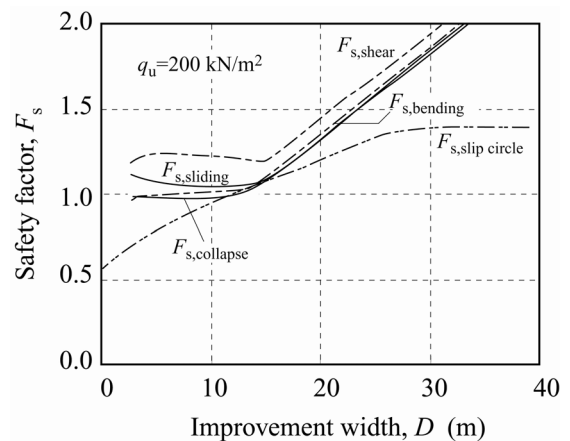
(1) Effect of column strength

Figure 63 shows the relationship between the improvement width, D, and safety factors for column strength, $q_{u,\text{column}}$, of 100, 200 and 500 kN/m² in the case of

improvement area ratio, a_s, of 50% and stress concentration ratio, n, of 3. In the case of $q_{u,\text{column}}$ of 100 kN/m², **Fig. 63(a)**, the safety factor for the sliding failure mode, $F_{s,\text{sliding}}$, and the shear failure mode, $F_{s,\text{shear}}$, almost coincide, and that for the collapse failure mode, $F_{s,\text{collapse}}$, and bending failure mode, $F_{s,\text{bending}}$, also almost coincide. $F_{s,\text{sliding}}$ and $F_{s,\text{shear}}$ decrease gradually and $F_{s,\text{collapse}}$ and $F_{s,\text{bending}}$ remain almost constant when D is smaller than about 15 m, because the active earth pressure acting on the improved area increases with the increase in embankment height with increasing D (see **Fig. 62**). However, when D exceeds about 15 m, all the safety factors increase linearly with increasing D. $F_{s,\text{sliding}}$ and $F_{s,\text{shear}}$ are lower than $F_{s,\text{collapse}}$ and $F_{s,\text{bending}}$ when D is larger than about 10 m. This indicates that the improved ground fails either by sliding or shear failure mode rather than by collapse or bending failure mode. As the depth of failure plane for the shear failure mode is 10 m at the bottom of the improved area, as later shown in **Fig. 64(a)**, it can be concluded that the sliding failure mode takes place instead of the shear failure mode. In the figure, $F_{s,\text{slip circle}}$ is also plotted. $F_{s,\text{slip circle}}$ increases almost linearly with increasing D, but $F_{s,\text{slip circle}}$ reaches a constant value at D of about 30 m, which is quite a different phenomenon from the other factors.
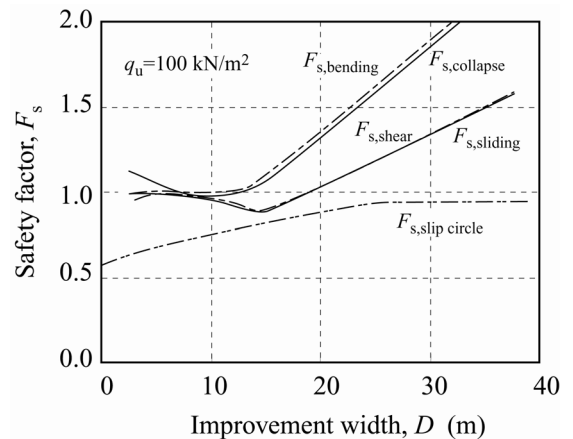
(a) $q_{u,\text{column}}$ of 100 kN/m²

(b) $q_{u,\text{column}}$ of 200 kN/m²
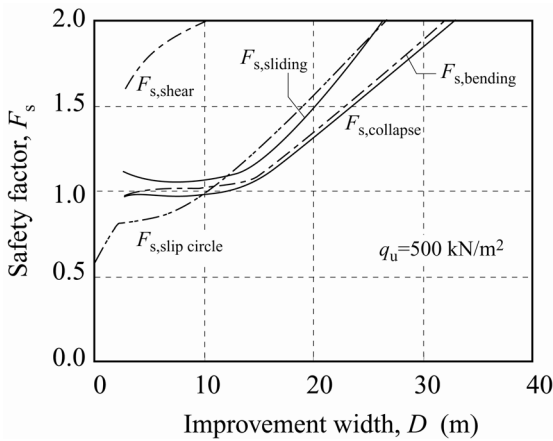
(c) $q_{u,column}$ of 500 kN/m²

Fig. 63. Effect of column strength on improvement width and safety factor relation

As $q_{u,column}$ increases, the magnitude of $F_{s,sliding}$ and $F_{s,shear}$ becomes higher. However, the magnitude of $F_{s,collapse}$ and $F_{s,bending}$ remains constant irrespective of D. In the case of $q_{u,column}$ of 200 kN/m², **Fig. 63(b)**, $F_{s,sliding}$, $F_{s,collapse}$ and $F_{s,bending}$ almost coincide and are lower than $F_{s,shear}$. This means that the improved ground fails by either sliding, collapse or bending failure mode. All the factors remain almost constant when D is smaller than about 15 m, but increase linearly when D exceeds about 15 m. $F_{s,slip circle}$ increases almost linearly and reaches a constant value at D of about 30 m.

In the case of $q_{u,column}$ of 500 kN/m², **Fig. 63(c)**, $F_{s,collapse}$ and $F_{s,bending}$ almost coincide and are more or less higher than $F_{s,sliding}$. However, $F_{s,shear}$ is considerably higher than the other three, a result of the role played by the shear strength of columns, F_{rf}, in Eq. (39). As later shown in Fig. 8, the failure depth for the bending failure mode is 10 m. These findings indicate that the improved ground fails by collapse failure mode. $F_{s,slip circle}$ continuously increases with increasing D, which is quite a different phenomenon from that described in **Figs. 63(a)** and **63(b)**.

It can be concluded that the failure mode of the improved ground is highly dependent upon the column strength: the sliding failure mode when $q_{u,column}$ is of a relatively low order of 100 kN/m² and the collapse failure mode when $q_{u,column}$ is of a relatively high order of 500 kN/m². This phenomenon is confirmed irrespective of the improvement area ratio.

Drawing a comparison, the magnitude of $F_{s,slip circle}$ is always the lowest in the case of $q_{u,column}$ of 100 and 200 kN/m², but not in the case of $q_{u,column}$ of 500 kN/m². As described above, the current design method has two criteria: the sliding failure mode in the external stability and the slip circle calculation in the internal stability. Regarding the ground conditions studied, the current

design method gives the lowest safety factor in the case of relatively low column strength of the order of 100 or 200 kN/m², but an overestimation in the case of relatively high column strength of the order of 500 kN/m².

Figures 64(a) to **64(c)** show the relationship between D and failure depth, z_f, for various $q_{u,column}$ values. In the case of $q_{u,column}$ of 100 kN/m², **Fig. 64(a)**, $z_{f,shear}$ and $z_{f,bending}$ increase with increasing D, and reach a constant value of 10 m at D of about 5 m and 15m, respectively. This indicates that neither bending failure mode nor shear failure mode takes place after that. As $q_{u,column}$ increases, the magnitude of $z_{f,shear}$ increases, while $z_{f,bending}$ remains constant, as shown in **Figs. 64(b)** and **64(c)**. In the case of $q_{u,column}$ of 200 kN/m², when D exceeds about 5 m, $z_{f,bending}$ and $z_{f,shear}$ become 10 m. This means that neither bending failure mode nor shear failure mode takes place in the practical improvement width. The $z_{f,slip circle}$ increases almost linearly with increasing D irrespective of $q_{u,column}$. Its magnitude increases rapidly with increasing $q_{u,column}$.
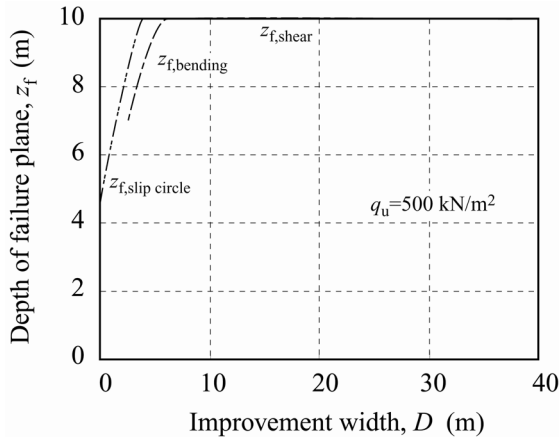
In the case of $q_{u,column}$ of 500 kN/m², $z_{f,slip circle}$ reaches 10 m at quite a small D value of about 3 m. This indicates that the slip circle analysis does not evaluate the internal stability under practical conditions.
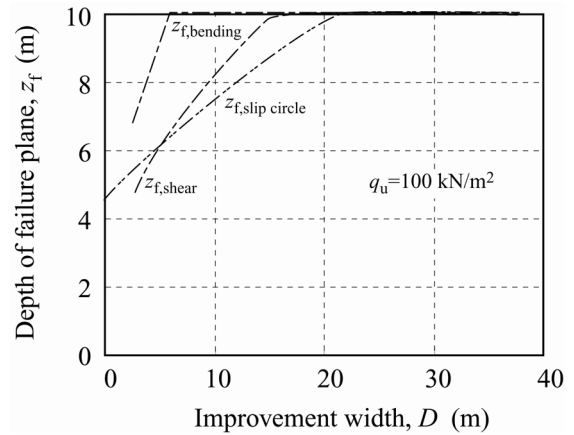

(a) $q_{u,column}$ of 100 kN/m²
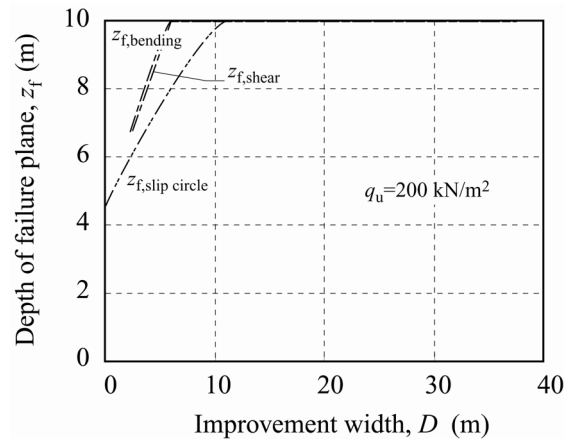
(b) $q_{u,column}$ of 200 kN/m²

(c) $q_{u,column}$ of 500 kN/m^2

Fig. 64. Effect of column strength on improvement width and depth of failure plane relation

The required improvement width should be determined so as to ensure that the safety factor for all the failure modes is higher than the allowable F_s value. Here, the allowable F_s value is simply assumed as 1.25, which is the value adopted in the slip circle analysis in the current design method (PWRC, 2004).

Figure 65 shows the required improvement width, $D_{req.}$ along with $q_{u,column}$. The $D_{req.}$ for the shear failure mode, $D_{req.,shear}$, decreases very rapidly with increasing $q_{u,column}$ and reaches zero at $q_{u,column}$ of about 300 kN/m^2, which means that the shear failure mode can not be a critical factor under practical conditions. The $D_{req.}$ for the slip circle, $D_{req.,slip circle}$, decreases rapidly with increasing $q_{u,column}$ and reaches an almost constant value when $q_{u,column}$ is about 500 kN/m^2. The $D_{req.}$ values for the collapse failure mode, $D_{req.,collapse}$, and bending failure mode, $D_{req.,bending}$, almost coincide and decrease very slightly with increasing $q_{u,column}$. The $D_{req.}$ should be adopted as the maximum value among all the failure modes, and be determined for the slip circle failure mode when $q_{u,column}$ is
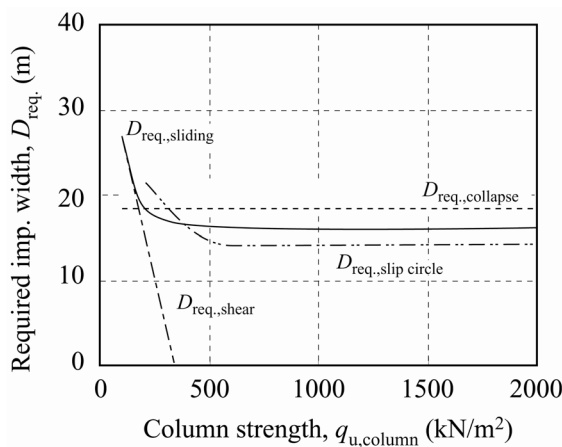

Fig. 65. Column strength and required improvement width relation

lower than about 300 kN/m^2 and for the collapse failure mode when $q_{u,column}$ exceeds about 300 kN/m^2. The effect of the column strength on the $D_{req.}$ is highly dominant when $q_{u,column}$ is lower than about 300 kN/m^2, but is negligible when $q_{u,column}$ exceeds about 300 kN/m^2.

(2) Effect of improvement area ratio

As discussed above, the failure mode of the improved ground is highly dependent upon the column strength: sliding failure mode for relatively low column strength and collapse failure mode for high column strength. Here, the effect of improvement area ratio is discussed for two separate cases of column strength.

For $q_{u,column}$ of 100 kN/m^2, **Figure 66** shows the effect of the improvement area ratio, a_s, on the relationship between D and F_s. In the case of a_s of 25%, **Fig. 66(a)**, $F_{s,collapse}$ and $F_{s,bending}$, and $F_{s,sliding}$ and $F_{s,shear}$ almost coincide throughout D. All the safety factors decrease slightly when D is lower than about 15 m, but increase linearly with increasing D for further D value. The increasing ratio of $F_{s,collapse}$ and $F_{s,bending}$ is larger than that of $F_{s,sliding}$ and $F_{s,shear}$, because the resistant moment components, M_{rt} and M_{re}, increase very rapidly (see Eqs. (38) and (40)). In the

(a) a_s of 25%

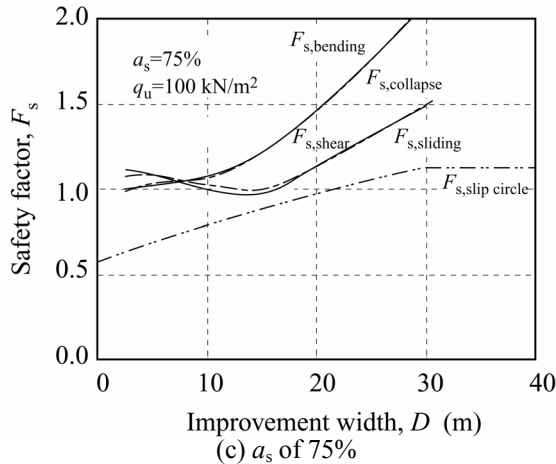

(b) a_s of 50%

(c) a_s of 75%
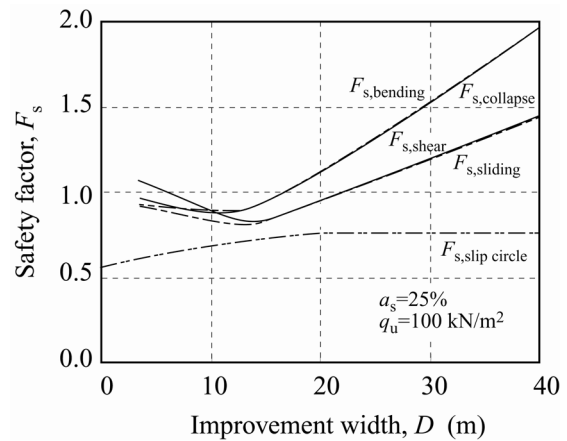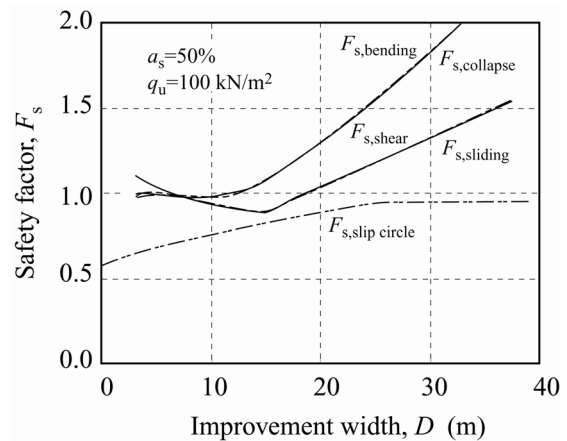
Fig. 66. Effect of improvement area ratio on improvement width and safety factor relation ($q_{u,column}$ of 100 kN/m²)

figure, $F_{s,slip\ circle}$ is plotted together. It can be seen that $F_{s,slip\ circle}$ increases almost linearly and reaches a constant value at D of about 20 m. It can also be seen that $F_{s,slip\ circle}$ is the lowest throughout D. Even with increasing a_s, **Figs. 66(b)** and **66(c)**, $F_{s,collapse}$ and $F_{s,bending}$, and $F_{s,sliding}$ and $F_{s,shear}$ still almost coincide throughout D, and $F_{s,slip\ circle}$ increases with increasing D to a constant value, which is a similar phenomenon to the case of a_s of 25%.

Comparing the figures, the magnitude of all the factors becomes higher with increasing a_s. As $F_{s,sliding}$ is always lower than $F_{s,collapse}$ for a wide range of D, it can be concluded that the improved ground fails by sliding failure mode rather than by collapse failure mode. It was found that $F_{s,slip\ circle}$ is the lowest throughout D irrespective of a_s. It can be concluded that the current design method, slip circle analysis, gives a reasonable evaluation.

In order to investigate the effect in more detail, $F_{s,sliding}$ and $F_{s,collapse}$ are plotted in **Fig. 67** along with a_s for D of 15 m and 20 m, in which the F_s value is close to the allowable F_s value of 1.25. $F_{s,sliding}$ increases slightly with increasing a_s irrespective of D, while $F_{s,collapse}$ increases
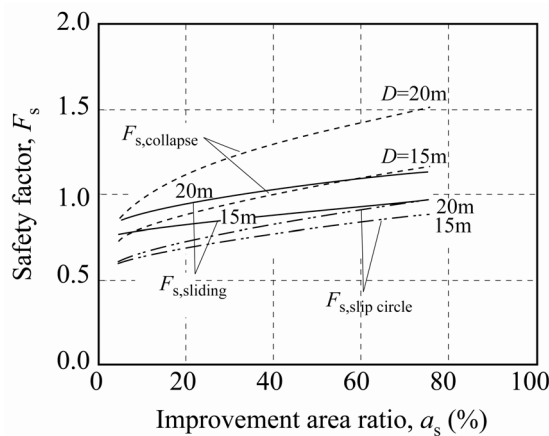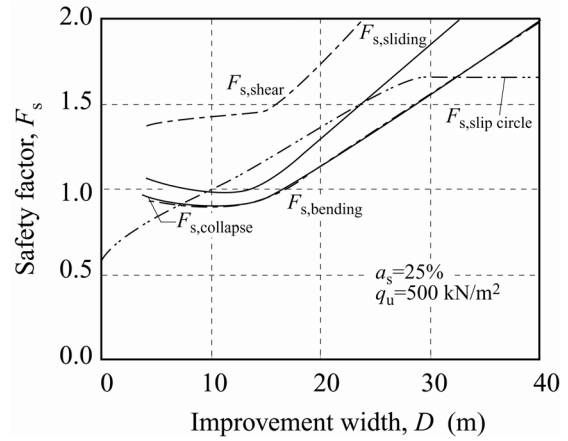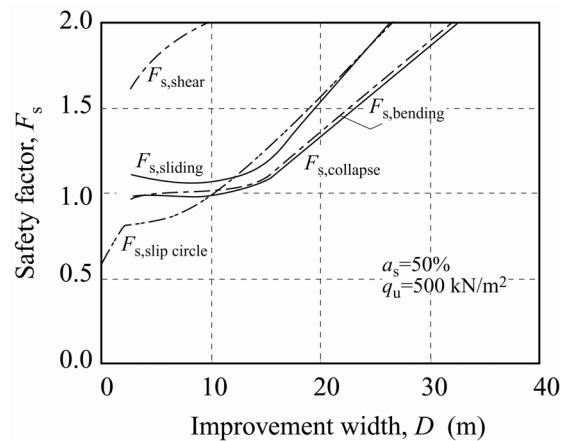

Fig. 67. Improvement area ratio and safety factor relation ($q_{u,column}$ of 100 kN/m²)

more rapidly compared with $F_{s,sliding}$. In the figure, $F_{s,slip\ circle}$ is also plotted. Drawing a comparison, $F_{s,slip\ circle}$ gives the lowest value, and increases slightly with increasing a_s.
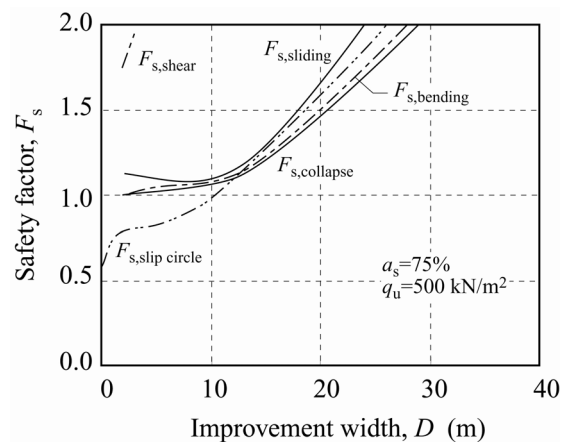
Figure 68 shows the relationship between D and F_s for $q_{u,column}$ of 500 kN/m². In the case of a_s of 25%, **Fig. 68(a)**, $F_{s,collapse}$ and $F_{s,bending}$ almost coincide throughout D and

(a) a_s of 25%

(b) a_s of 50%

(c) a_s of 75%

Fig. 68. Effect of improvement area ratio on improvement width and safety factor relation ($q_{u,column}$ of 500 kN/m²)

increase with increasing D. $F_{s,sliding}$ is slightly higher than the above two factors, but $F_{s,shear}$, on the other hand, is much higher than the other three. $F_{s,slip\ circle}$ increases almost linearly with increasing D and reaches a constant value at D of about 30 m. It was found that $F_{s,slip\ circle}$ is higher than $F_{s,collapse}$ and $F_{s,bending}$ for a wide range of D.

With increasing a_s, **Figs. 68(b)** and **68(c)**, the magnitude of all the factors becomes higher, while $F_{s,shear}$ shows quite a high increase compared to the others. The magnitude of $F_{s,slip\ circle}$ also becomes higher as a_s increases and still gives a higher value than $F_{s,collapse}$ and $F_{s,bending}$. It is of interest to note that the difference in magnitude between $F_{s,slip\ circle}$ and $F_{s,collapse}$ becomes smaller with increasing a_s, which means that the failure mode tends to change from collapse failure mode to sliding failure mode.

Figure 69 shows $F_{s,sliding}$ and $F_{s,collapse}$ values along with a_s for D of 15 m and 20 m. $F_{s,sliding}$ and $F_{s,collapse}$ increase rapidly at first and then more slowly with increasing a_s irrespective of D. In the figure, $F_{s,slip\ circle}$ is also plotted along with a_s. Drawing a comparison, $F_{s,slip\ circle}$ is higher than $F_{s,collapse}$ irrespective of D and a_s. This indicates that the current design method gives an overestimation.
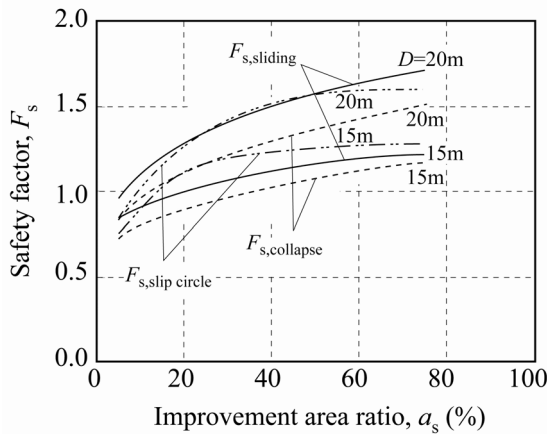

Fig. 69. Improvement area ratio and safety factor relation ($q_{u,column}$ of 500 kN/m^2)

Figures 70(a) and **70(b)** show $D_{req.}$ for ensuring F_s of 1.25 along with a_s for $q_{u,column}$ of 100 and 500 kN/m^2, respectively. In the case of $q_{u,column}$ of 100 kN/m^2, **Fig. 70(a)**, as $F_{s,slip\ circle}$ is always lower than unity irrespective of D, $D_{req.,slip\ circle}$ can not be obtained. $D_{req.,sliding}$ and $D_{req.,collapse}$ decrease with increasing a_s, while $D_{req.,sliding}$ is always larger than $D_{req.,sliding}$. $D_{req.}$ is determined by the criteria of the sliding failure mode.

In the case of $q_{u,column}$ of 500 kN/m^2, **Fig. 70(b)**, $D_{req.,sliding}$ and $D_{req.,collapse}$ decrease with increasing a_s. $D_{req.,slip\ circle}$ decreases rapidly at first and then more slowly with increasing a_s. The $D_{req.,collapse}$ is always the largest throughout a_s.
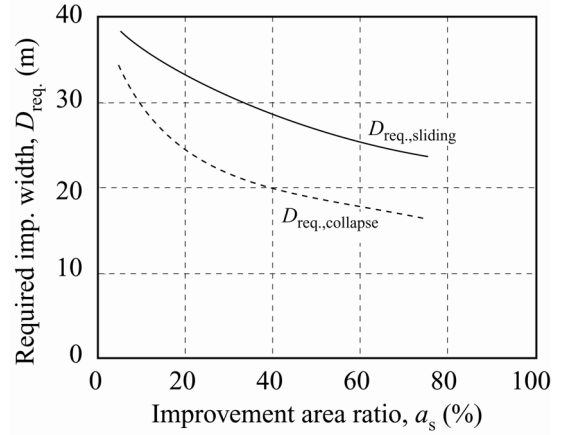
(a) $q_{u,column}$ of 100 kN/m^2
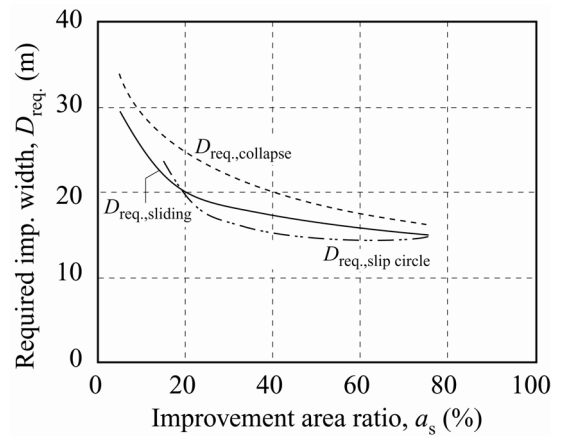
(b) $q_{u,column}$ of 500 kN/m^2

Fig. 70. Improvement area ratio and required improvement width relation

(3) Effect of column diameter

Similar to the previous discussion, the effect of column diameter, B, is discussed here for the two separate column strengths. For the case of the column strength of 100 kN/m^2, **Figure 71** shows the effect of the column diameter, B, on the relationship between D and F_s, while a_s remains constant at 50%. In the case of B of 0.5 m, **Fig. 71(a)**, $F_{s,collapse}$ and $F_{s,bending}$, and $F_{s,sliding}$ and $F_{s,shear}$ almost coincide when D is larger than about 10 m. All the factors decrease slightly when D is lower than 15 m; however, they increase linearly with increasing D when D exceeds about 15 m. $F_{s,collapse}$ and $F_{s,bending}$ increase more rapidly and are higher than $F_{s,sliding}$ and $F_{s,shear}$. $F_{s,slip\ circle}$ increases at first and then reaches a constant value at D of about 25 m. A similar phenomenon can be seen in the case of B of 1 m, **Fig. 71(b)**. In the case of B of 2 m, **Fig. 71(c)**, $F_{s,collapse}$ and $F_{s,bending}$ continuously increase with increasing D and are always higher than $F_{s,sliding}$ and $F_{s,shear}$. Comparing the figures, the magnitude of $F_{s,collapse}$ and $F_{s,bending}$ becomes much higher with increasing B, because the resistant moment component from the weight of the embankment,

M_{re}, increases very rapidly (see Eqs. (38) and (40)). The magnitude of $F_{s,sliding}$ and $F_{s,shear}$, on the other hand, remains constant irrespective of B. It can be concluded that the improved ground fails by sliding failure mode irrespective of B. It was found that $F_{s,slip\ circle}$ is the lowest throughout D irrespective of B.
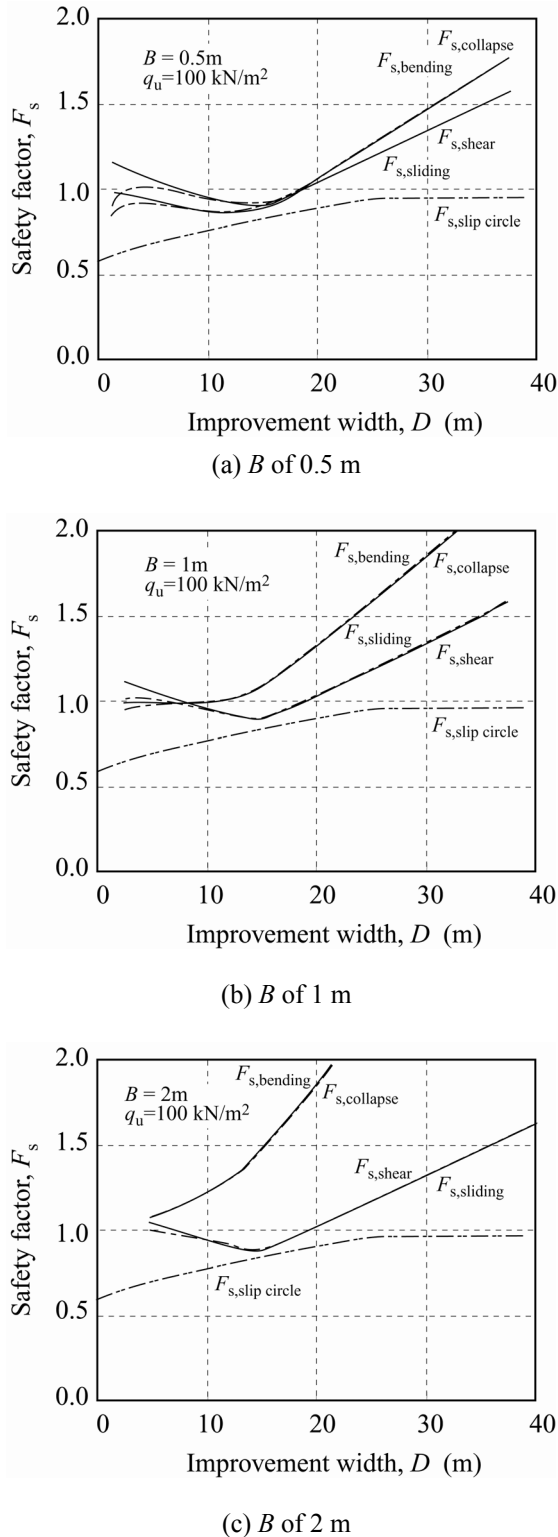

(a) B of 0.5 m

(b) B of 1 m

(c) B of 2 m

Fig. 71. Effect of column diameter on improvement width and safety factor relation ($q_{u,column}$ of 100 kN/m²)

Figure 72 shows $F_{s,sliding}$, $F_{s,collapse}$ and $F_{s,slip\ circle}$ along with B where D of 15 m and 20 m in order to discuss the effect in detail. $F_{s,sliding}$ remains a constant value irrespective of B, because the resistant forces are not influenced by B but rather by a_s. $F_{s,collapse}$, on the other hand, increases very rapidly with increasing B irrespective of D. $F_{s,slip\ circle}$ remains constant irrespective of B and is the lowest throughout B irrespective of D. This confirms that the current design method gives a reasonable safety factor value.
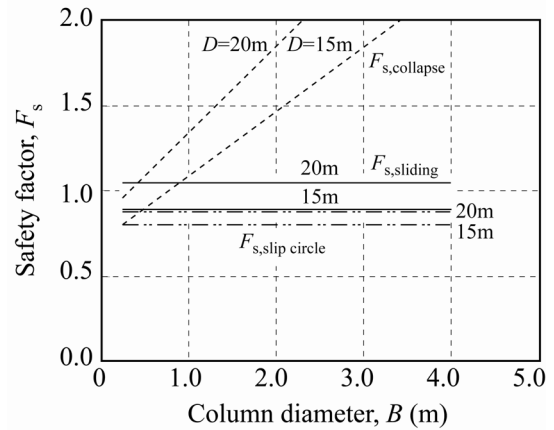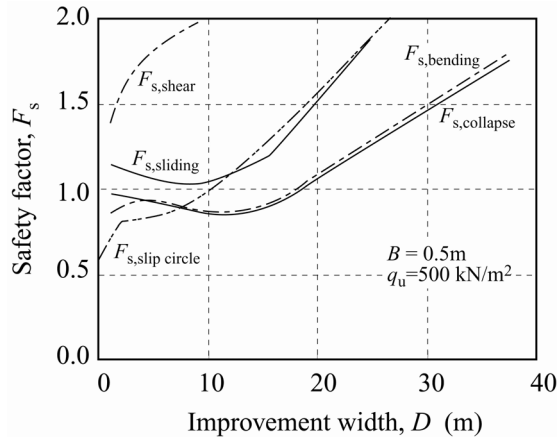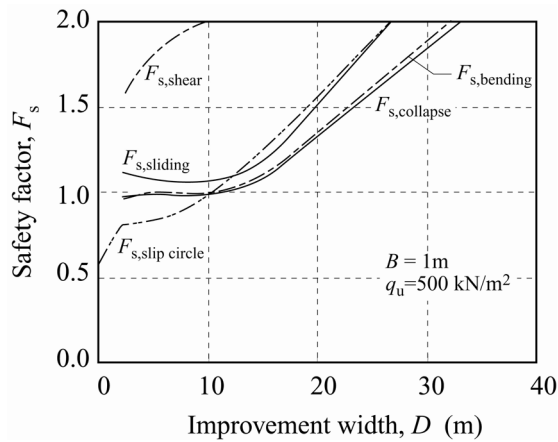

Fig. 72. Column diameter and safety factor relation ($q_{u,column}$ of 100 kN/m²)

Figure 73 shows the effect of column diameter for $q_{u,column}$ of 500 kN/m². In the case of B of 0.5 m, **Fig. 73(a)**, $F_{s,collapse}$ and $F_{s,bending}$ almost coincide throughout D; however, $F_{s,sliding}$ and $F_{s,shear}$ differ greatly in magnitude and are much higher than the above two safety factors. This is due to the resistant force due to the undrained shear strength of column, F_{rc}, in the shear failure mode (see Eq. (39)). $F_{s,collapse}$ and $F_{s,bending}$ decrease slightly with increasing D when D is lower than 15 m; however, they increase linearly with increasing D when D exceeds about 15 m. As the magnitude of $F_{s,collapse}$ and $F_{s,bending}$ is always lower than that of $F_{s,sliding}$ and $F_{s,shear}$, it can be concluded that the improved ground fails by collapse failure mode throughout D. The magnitude of $F_{s,slip\ circle}$ is much higher than that of $F_{s,collapse}$ and $F_{s,bending}$, and is close to $F_{s,sliding}$ for a wide range of D.

With increasing B, the magnitude of $F_{s,collapse}$ and $F_{s,bending}$ increases rapidly throughout D, because of the increase in resistant moment component from the weight of the embankment, M_{re}. The magnitude of $F_{s,sliding}$, on the other hand, remains constant irrespective of B. In the case of B of 1 m, **Fig. 73(b)**, $F_{s,collapse}$ and $F_{s,bending}$ become close to $F_{s,sliding}$, but are still lower than $F_{s,sliding}$. However, when B of 2 m, **Fig. 73(c)**, $F_{s,collapse}$ and $F_{s,bending}$ become higher than $F_{s,sliding}$. It is of interest to note that the failure mode changes from collapse failure mode to sliding failure mode with increasing B.

(a) B of 0.5 m

(b) B of 1 m
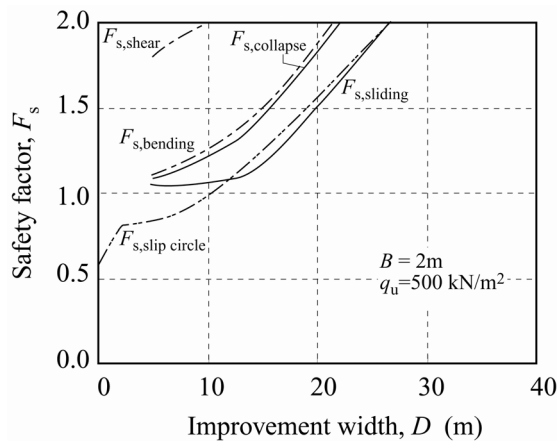
(c) B of 2 m

Fig. 73. Effect of column diameter on improvement width and safety factor relation ($q_{u,column}$ of 500 kN/m²)

Figure 74 shows $F_{s,sliding}$, $F_{s,collapse}$ and $F_{s,slip\ circle}$ along with B where D of 15 m and 20 m. According to the above discussion, $F_{s,sliding}$ remains constant throughout B, while $F_{s,collapse}$ increases almost linearly with increasing B.

$F_{s,collapse}$ is smaller than $F_{s,sliding}$ as long as B is lower than about 1.5 m, but is higher when B exceeds about 1.5 m. $F_{s,slip\ circle}$ remains constant throughout B, and is higher than $F_{s,sliding}$ and $F_{s,collapse}$ when B is smaller than about 1.5 m, but lower when B is larger than about 1.5 m. This indicates that the current design method gives an overestimation when B is smaller than about 1.5 m.
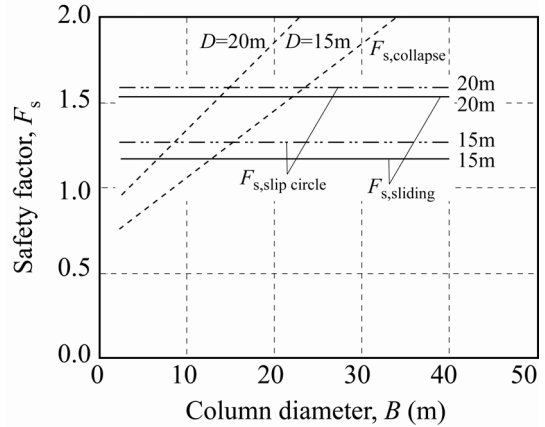

Fig. 74. Column diameter and safety factor relation ($q_{u,column}$ of 500 kN/m²)

Figure 75 shows the relationship between B and $D_{req.}$. In the case of $q_{u,column}$ of 100 kN/m², **Fig. 75(a)**, $D_{req.,collapse}$ and $D_{req.,bending}$ almost coincide and decrease rapidly with increasing B. However, $D_{req.,sliding}$ and $D_{req.,shear}$ remain constant throughout B. The figure shows that $D_{req.}$ is determined by the criteria of the sliding failure mode, and remains almost constant irrespective of B.

A similar phenomenon can be seen in the case of $q_{u,column}$ of 500 kN/m², as shown in **Fig. 75(b)**. $D_{req.,collapse}$ and $D_{req.,bending}$ decrease rapidly with increasing B. However, $D_{req.,sliding}$ and $D_{req.,shear}$ also almost coincide and remain constant irrespective of B. $D_{req.,collapse}$ and $D_{req.,bending}$ intersect with $D_{req.,sliding}$ and $D_{req.,shear}$ at B of about 1.2 m. In the case of B smaller than about 1.2 m, $D_{req.}$ decreases rapidly with increasing B, but remains constant when B exceeds about 1.2 m.
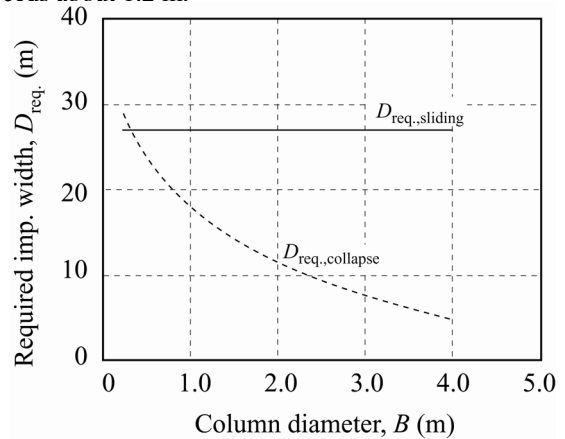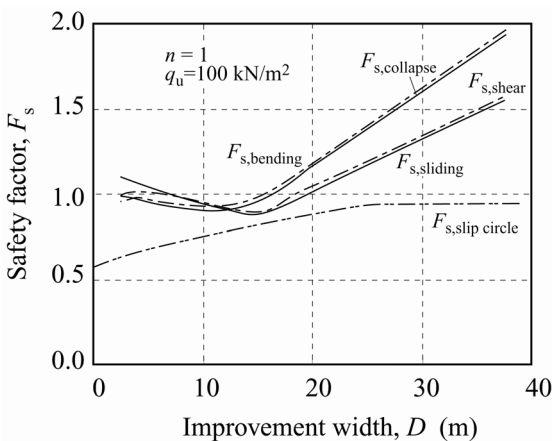

(a) $q_{u,column}$ of 100 kN/m²
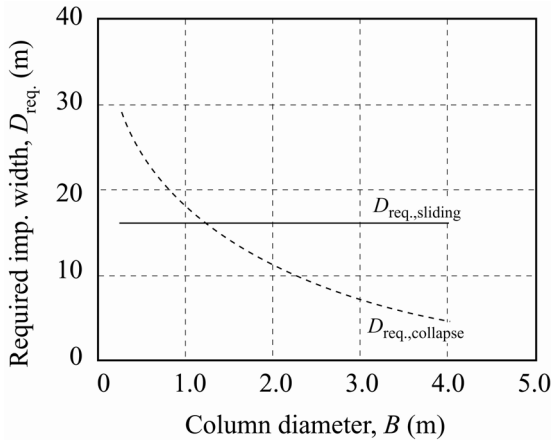
(b) $q_{u,column}$ of 500 kN/m^2

**Fig. 75**. Column diameter and required improvement width relation

(4) Effect of stress concentration ratio

The stress concentration ratio, n, is one of the key parameters in the design and is usually assumed as 3 to 5 in the current design method for evaluating consolidation settlement. However, accumulated field data is very scattered and depends upon many factors such as original and improved ground conditions, loading conditions and type of measurement, so a definitive value for the ratio has not yet been obtained. The slip circle analysis is not influenced by the magnitude of n value, but the collapse and bending failure modes are influenced. Here, the effect of stress concentration ratio is discussed for two separate cases.

Figure 76 shows the effect of n for the case of column strength of 100 kN/m^2. In the case of n of 1, **Fig. 76(a)**, $F_{s,collapse}$ and $F_{s,bending}$, and $F_{s,sliding}$ and $F_{s,shear}$ almost coincide throughout D. All the factors remain almost constant or decrease slightly when D is lower than about 15 m, but increase linearly with increasing D for further D value. In the figure, $F_{s,slip circle}$ is also plotted. $F_{s,slip circle}$ increases almost linearly with increasing D, but reaches a constant value at D of about 25 m.

(a) n of 1
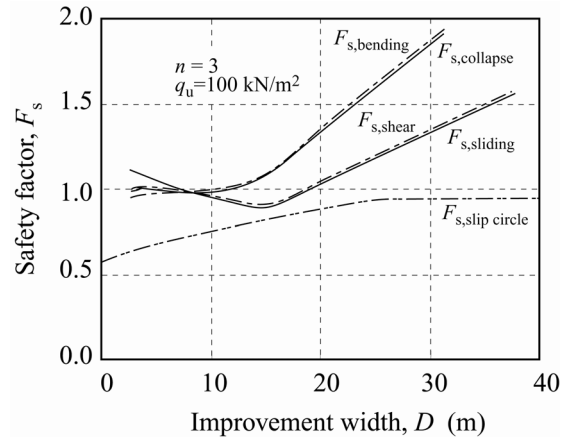
(b) n of 3
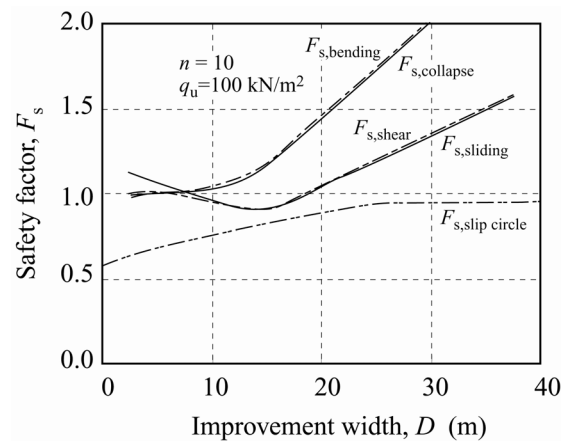
(c) n of 10

Fig. 76. Effect of stress concentration ratio on improvement width and safety factor relation ($q_{u,column}$ of 100 kN/m^2)

The magnitude of $F_{s,collapse}$ and $F_{s,bending}$ becomes larger with increasing n, **Figs. 76(b)** and **76(c)**, because of the increase in resistant moment component from the weight of the embankment, M_{re} (Eqs. (38) and (40)). The magnitude of $F_{s,sliding}$ and $F_{s,shear}$, on the other hand, remain almost constant irrespective of n. The shear resistance mobilized on the bottom of columns, F_{rf}, increases with increasing n, as in Eq. (22). However, the resistant force from the undrained shear strength of column, F_{rt}, is lower than F_{rf} except underneath the slope edge even when n of 1. This means that the shear strength mobilized on the bottom of the improved area remains almost constant irrespective of n and consequently, $F_{s,sliding}$ and $F_{s,shear}$ remain almost constant. As $F_{s,sliding}$ and $F_{s,shear}$ are lower than $F_{s,collapse}$ and $F_{s,bending}$ irrespective of n in the case of D larger than 10 m, it can be assumed that the improved ground fails by sliding failure mode.

$F_{s,sliding}$ and $F_{s,collapse}$ are plotted in **Fig. 77** along with n where D of 15 m and 20 m. $F_{s,sliding}$ remains constant throughout n irrespective of D, while $F_{s,collapse}$ increases

rapidly at first and then only slightly with increasing n. In the figure, $F_{s,slip\ circle}$ is also plotted, and it remains constant irrespective of n. In a comparison, $F_{s,slip\ circle}$ gives the lowest value, which confirms that the current design method gives a reasonable magnitude of safety factor.
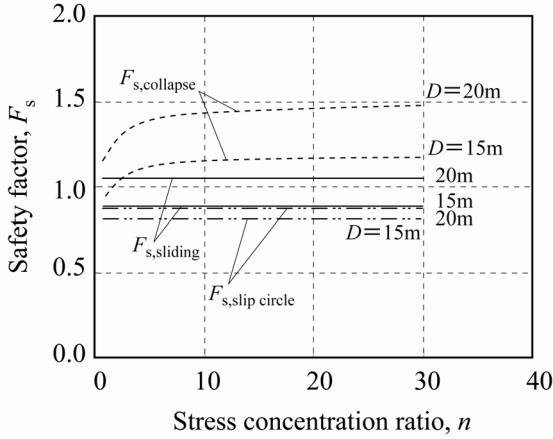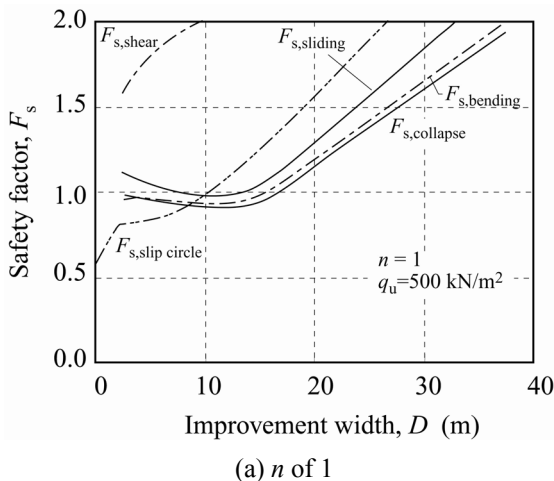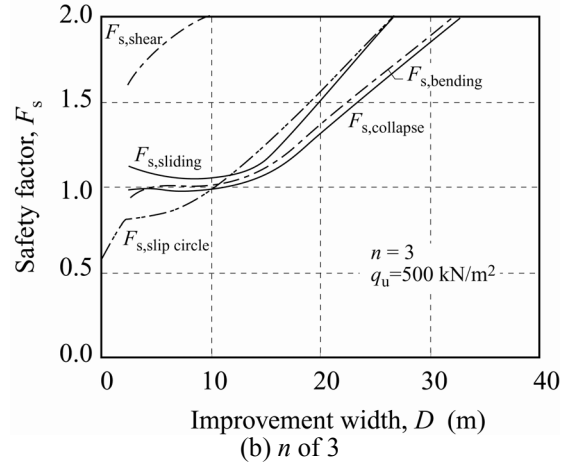

Fig. 77. Stress concentration ratio
and safety factor relation
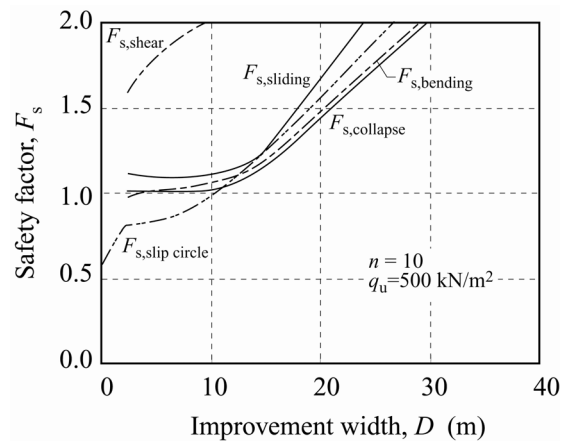($q_{u,column}$ of 100 kN/m²)

Figure 78 shows the effect of n for $q_{u,column}$ of 500 kN/m². In the case of n of 1, **Fig. 78(a)**, $F_{s,collapse}$ and $F_{s,bending}$ almost coincide irrespective of D. $F_{s,sliding}$ is slightly higher than the above two factors and increases with D when D exceeds about 15 m. $F_{s,shear}$, on the other hand, is much higher than the above three safety factors and increases with increasing D. A similar phenomenon can be seen in the other n values (see **Figs. 78(b)** and **78(c)**). Comparing the figures, the magnitude of $F_{s,collapse}$, $F_{s,bending}$ and $F_{s,sliding}$ become higher with increasing n. For $F_{s,sliding}$, the shear resistance mobilized on the bottom of columns, F_{rf}, increases with increasing n, but is still lower than F_{rt}. Therefore, $F_{s,sliding}$ increases with increasing n. As $F_{s,collapse}$ is always the lowest irrespective of n, it can be assumed that the improved ground fails by collapse failure mode rather than by sliding failure mode.

(a) n of 1

(b) n of 3

(c) n of 10
Fig. 78. Effect of stress concentration ratio
on improvement width and safety factor relation
($q_{u,column}$ of 500 kN/m²)

$F_{s,sliding}$ and $F_{s,collapse}$ are plotted in **Fig. 79** along with n where D of 15 m and 20 m. $F_{s,sliding}$ and $F_{s,collapse}$ increase rapidly at first and then only slightly with increasing n irrespective of D. It can be seen that $F_{s,collapse}$ is lower than $F_{s,sliding}$ irrespective of n and D. $F_{s,slip\ circle}$ remains constant and is still higher than $F_{s,collapse}$ irrespective of n and D, which confirms that the current design method gives an overestimation of the safety factor.

Figure 80 shows $D_{req.}$ along with n. As $F_{s,slip\ circle}$ is always lower than unity irrespective of D in the case of $q_{u,column}$ of 100 kN/m², **Fig. 80(a)**, $D_{req.,slip\ circle}$ can not be obtained. $D_{req.,sliding}$ remains constant throughout n, while $D_{req.,collapse}$ decreases rapidly but soon reaches an almost constant value when n exceeds about 10. $D_{req.}$ should be the maximum value for all the failure modes, which remains constant irrespective of the n value. In the case of $q_{u,column}$ of 500 kN/m², **Fig. 80(b)**, $D_{req.,collapse}$ and $D_{req.,sliding}$ decrease and reach a constant value, while $D_{req.,slip\ circle}$ remains constant throughout n. $D_{req.}$ should be determined as $D_{req.,collapse}$, which is influenced by the n value as long as n is lower than about 5.
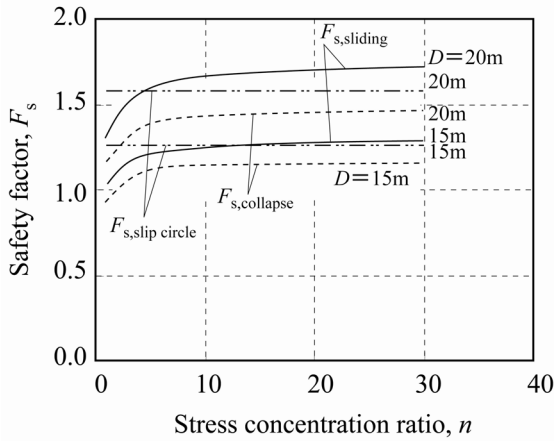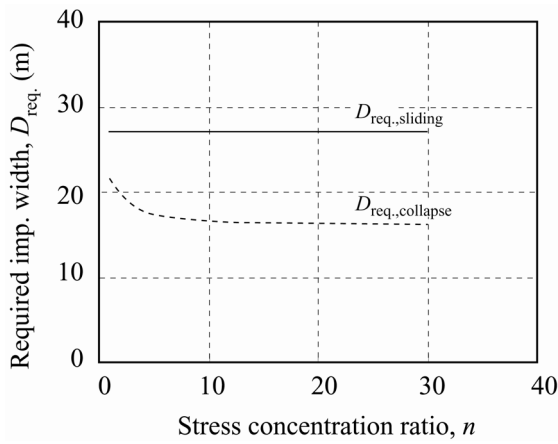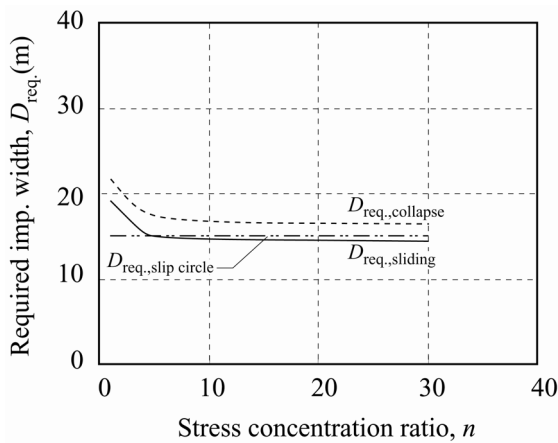
Fig. 79. Stress concentration ratio
and safety factor relations
($q_{\text{u,column}}$ of 500 kN/m^2)

(a) $q_{\text{u,column}}$ of 100 kN/m^2

(b) $q_{\text{u,column}}$ of 500 kN/m^2
Fig. 80. Stress concentration ratio
and required improvement width relation

5.5 Possibility of safety margin

As discussed above, the current design method, which consists of calculating the slip circle failure mode and the sliding failure modes, gives a reasonable evaluation as long as the improved ground is expected to fail by sliding failure mode, but gives an overestimation when the ground is expected to fail by collapse failure mode. This conclusion is quite reasonable and emphasizes the importance of simulating appropriate failure modes for evaluating the stability of improved ground. The failure pattern is highly influenced by column strength and diameter of column, and the collapse failure pattern takes place under practical ground and improvement conditions in Japan, where the column strength and improvement area ratio are usually set at 400 to 500 kN/m^2 and around 50%, respectively. However, as far as the author knows, few cases have been reported where ground failure or considerably large ground deformation took place in the group column type improved ground. This indicates that a sort of safety margin, which is not taken into account in the current design method, might compensate for the discrepancy. Here, the effect of three possible factors is investigated to determine if they could serve as a safety margin: ground consolidation due to embankment weight, underestimation of ground strength profile, and effect of surface crust.

(1) Effect of ground consolidation

The embankment is usually constructed step by step to assure its stability during the process, which usually takes a couple of months to complete. Some degree of consolidation takes place in the clay layer during the construction, increasing the ground strength and in turn increasing the stability of the improved ground. However, this effect is seldom taken into account in the practical design for evaluating the stability of the improved ground. An additional series of calculations was carried out to investigate the effect. As the consolidation of the clay layer close to the permeable layer proceeds faster, the consolidation degree for the upper 1 m of the clay layer is changed in the calculations for ease of parametric calculations.

Figure 81 shows the relationship between D and $F_{\text{s,collapse}}$ for various degrees of consolidation in the case of $q_{\text{u,column}}$ of 500 kN/m^2. The magnitude of $F_{\text{s,collapse}}$ increases at almost the same rate throughout D as the degree of consolidation increases, but its increment is relatively small even at 100% consolidation. In the figure, $F_{\text{s,slip circle}}$ for the original ground strength profile is also plotted. $F_{\text{s,slip circle}}$ is still higher than $F_{\text{s,collapse}}$ for a wide range of D.
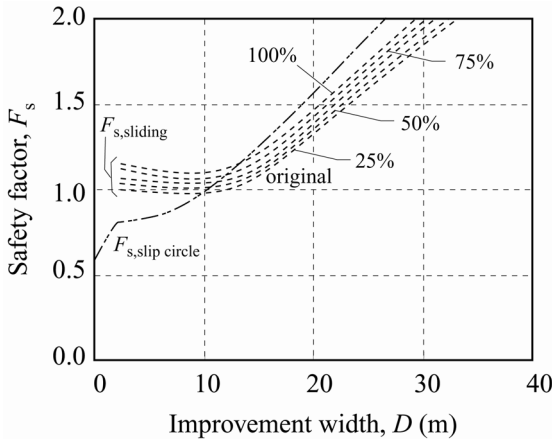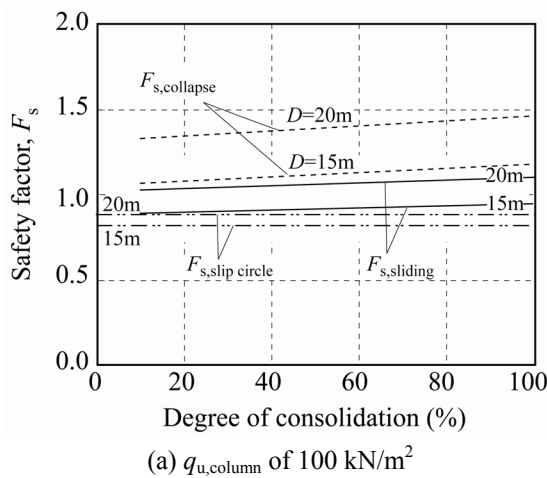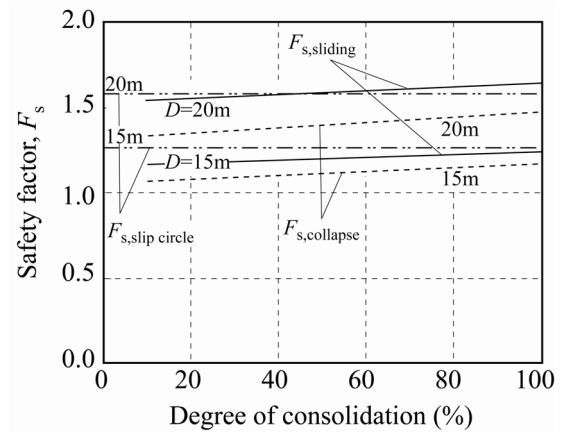
Fig. 81. Effect of degree of consolidation and improvement width and safety factor relation ($q_{u,column}$ of 500 kN/m^2)

(b) $q_{u,column}$ of 500 kN/m^2

Fig. 82. Degree of consolidation and safety factor relation

In order to investigate the effect in detail, **Figure 82** shows $F_{s,sliding}$ and $F_{s,collapse}$ along with the degree of ground consolidation where D of 15 m and 20 m. In the figure, the slip circle calculation for the original ground strength profile is plotted as a double chain straight line parallel to the horizontal axis. In the case of $q_{u,column}$ of 100 kN/m^2, **Fig. 82(a)**, $F_{s,sliding}$ and $F_{s,collapse}$ increase only slightly with increasing degree of consolidation irrespective of D. $F_{s,slip\ circle}$ for the original ground strength profile is always the lowest. In the case of $q_{u,column}$ of 500 kN/m^2, **Fig. 82(b)**, $F_{s,collapse}$ and $F_{s,sliding}$ increase slightly with increasing degree of consolidation, and $F_{s,collapse}$ is lower than $F_{s,sliding}$ and $F_{s,slip\ circle}$. The degree of consolidation achieved within the construction period, assuming three months, can be estimated less than 20 %, provided that the consolidation coefficient of the clay, c_v, is 1 cm^2/day. This reveals that the effect of ground consolidation on stability is quite small and can not compensate for the overestimation in the case of $q_{u,column}$ of 500 kN/m^2.

(2) Effect of ground soil condition

The measured shear strength profile is usually highly scattered in the field even if the sampling and field and laboratory tests are carried out with the best care. In addition, the shear strength of the clay ground is sometimes reduced by the induced disturbance effect in the sampling and testing stages. In the design stage, the mean or relatively lower strength profile is usually adopted as the design value based on the safe-side design concept. This provides that 'real ground strength' is higher than the designed value.

Figure 83 shows the parametric calculations for the case of $q_{u,column}$ of 500 kN/m^2, in which the shear strength of the clay layer increases: the strength at the ground surface and the strength increment ratio with depth change simultaneously. In the figure, $F_{s,collapse}$ is plotted along with D for various strength profiles. The magnitude of $F_{s,collapse}$ increases at almost the same rate throughout D as the ground strength increases. $F_{s,slip\ circle}$ for the original ground strength profile remains higher than $F_{s,collapse}$ for a wide
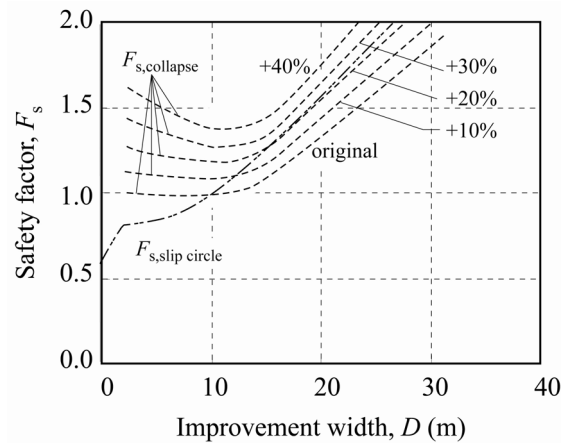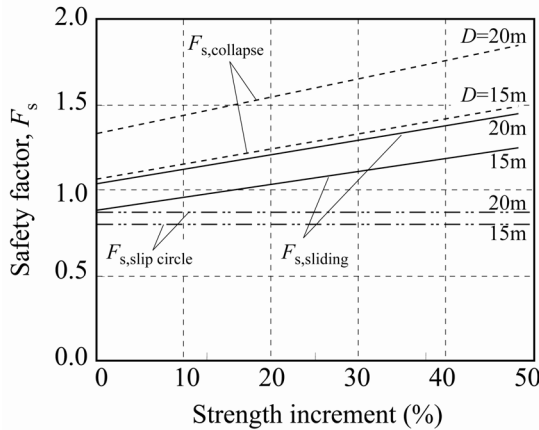

(a) $q_{u,column}$ of 100 kN/m^2

Fig. 83. Effect of ground strength increment on improvement width and safety factor relation ($q_{u,column}$ of 500 kN/m^2)
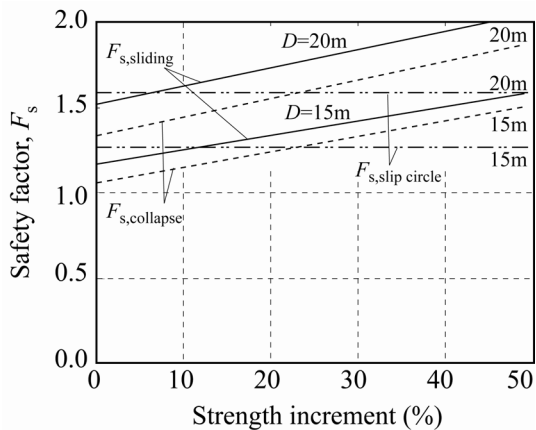
range of D as long as the strength increase is lower than 20%. However, $F_{s,slip\ circle}$ becomes lower than $F_{s,collapse}$ when the ground strength becomes 30% higher.

Figure 84 shows $F_{s,sliding}$ and $F_{s,collapse}$ along the percentage of ground strength increment where D of 15 m and 20 m. In the figure, the slip circle calculation for the original ground strength profile is plotted as a double chain line. In the case of $q_{u,column}$ of 100 kN/m^2, **Fig. 84(a)**, $F_{s,sliding}$ and $F_{s,collapse}$ increase almost linearly with increasing strength profile, and $F_{s,sliding}$ is always lower than $F_{s,collapse}$ irrespective of D. $F_{s,slip\ circle}$ is always the lowest. In the case of $q_{u,column}$ of 500 kN/m^2, **Fig. 84(b)**, $F_{s,sliding}$ and $F_{s,collapse}$ increase almost linearly, which is a similar phenomenon to the case of $q_{u,column}$ of 100 kN/m^2. $F_{s,collapse}$ is lower than $F_{s,slip\ circle}$ when the strength increment is lower than about 25%, but is higher when the ground strength increases to above 25%.

According to published reports (Watabe and Tsuchida, 2001), a 25% difference between the design strength and 'real strength' is possible. It is concluded that this effect can serve as a sort of safety margin to compensate for the overestimation.

(5) Effect of surface crust

Some deposits often have a dried crust at the surface where the strength is far higher than that of normally consolidated deposits. Many engineers have pointed out that construction would be more economical if the strength of this part could be taken into account. Bauer et al. (1973) and Nakase et al. (1987) investigated the effect of the crust on the bearing capacity of foundations. However, the effect of the crust is seldom taken into account in the practical design stage, based on the safe-side concept.

Here, the effect of the surface crust on the stability is discussed. In the calculations, the strength of the crust, $c_{u,crust}$, changes while its thickness remains constant at 1 m (see **Fig. 85**). **Figure 86** shows the relationship between $F_{s,collapse}$ along with D for $q_{u,column}$ of 500 kN/m^2. The magnitude of $F_{s,collapse}$ increases rapidly with increasing $c_{u,crust}$ throughout D, and becomes higher than $F_{s,slip\ circle}$ when $c_{u,crust}$ becomes 50 kN/m^2 for a wide range of D.
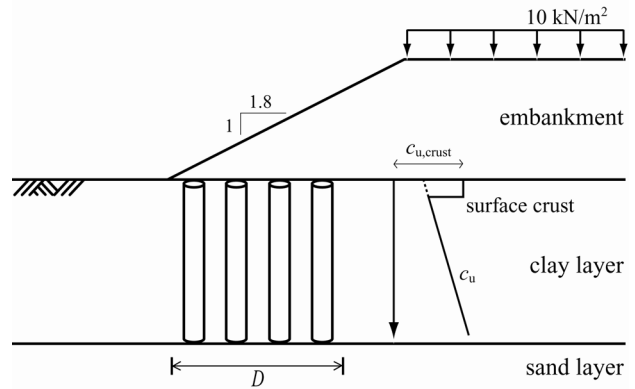
Fig.85. Strength profile for calculating the surface crust effect

(a) $q_{u,column}$ of 100 kN/m^2
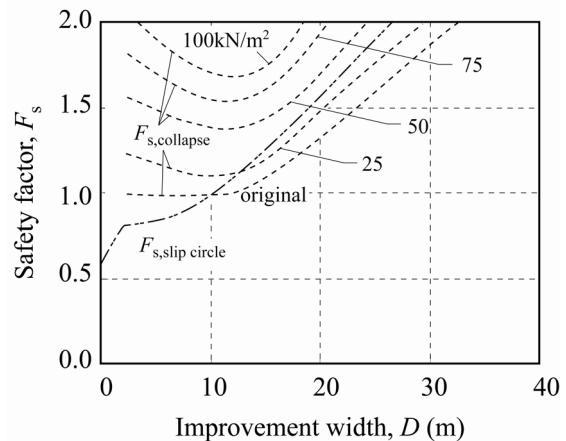
Fig. 86. Effect of surface crust on improvement width and safety factor relation ($q_{u,column}$ of 500 kN/m^2)

(b) $q_{u,column}$ of 500 kN/m^2

Fig. 84. Strength increment and safety factor relation

Figure 87 shows $F_{s,sliding}$ and $F_{s,collapse}$ along with $c_{u,crust}$ where D of 15 m and 20 m. In the case of $q_{u,column}$ of 100 kN/m^2, **Fig. 87(a)**, $F_{s,sliding}$ and $F_{s,collapse}$ increase with

increasing $c_{u,crust}$, but the latter increases more rapidly. $F_{s,sliding}$ is always lower than $F_{s,collapse}$ throughout $c_{u,crust}$ irrespective of D. In the figure, $F_{s,slip\ circle}$ is also plotted as a double chain line and is always the lowest. In the case of $q_{u,column}$ of 500 kN/m^2, **Fig. 87(b)**, it is of interest to note that $F_{s,collapse}$ becomes higher than $F_{s,sliding}$ when $c_{u,crust}$ exceeds about 30 and 45 kN/m^2 where D of 15 m and 20 m, respectively. This means that the failure mode changes to sliding failure mode with increasing $c_{u,crust}$. $F_{s,sliding}$ and $F_{s,collapse}$ become higher than $F_{s,slip\ circle}$ when $c_{u,crust}$ becomes higher than about 35 kN/m^2, which is close to $c_{u,crust}$ when the failure pattern changes to sliding failure mode.

Few reports are available on depth and strength of surface crust. Bauer et al. (1973) reported the depth of desiccated crust of about 3.7 m and shear strength of about 100 to 250 kN/m^2, which are quite high values compared to those in the calculations. This is a convincing argument that the effect of the surface crust could serve as a safety margin compensating for the overestimation in the current design method.
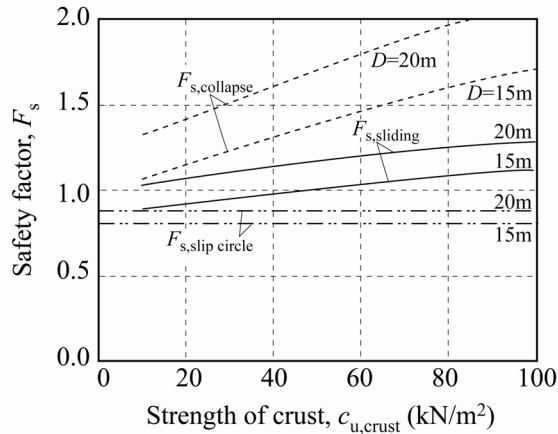
(a) $q_{u,column}$ of 100 kN/m^2
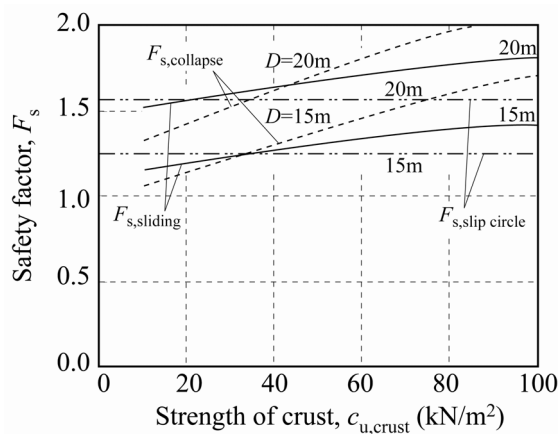
(b) $q_{u,column}$ of 500 kN/m^2
Fig. 87. Strength of crust and safety factor relation

5.6 Summary

A parametric calculations on evaluation of stability of column type DM improved ground was carried out to investigate the characteristics of the current design method and the proposed design method and the applicability of the current design method to evaluation of stability of DM improved ground. The major conclusions derived in this study are as follows:

1) The failure pattern of the column type improved ground is highly dependent upon column strength and column diameter. The improved ground fails by shear failure mode in the case of relatively low column strength of the order of 100 kN/m^2 and by collapse failure mode in the case of relatively high column strength of the order of 500 kN/m^2 for a column diameter of 1 m.

2) The slip circle calculation, which is used for evaluating the internal stability in the current design method, in fact evaluates the external stability of the improved ground with increasing column strength of the order of 500 kN/m^2. This means that there are no criteria for determining the required column strength from the viewpoint of stability analysis.

3) The effect of the improvement area ratio is dominant, where the safety factors for the sliding and collapse failure modes increase rapidly with increasing improvement area ratio.

4) The effect of the column diameter is also dominant, where the safety factor for the collapse failure mode increases with increasing column diameter, but that for the sliding failure mode is not influenced. It is of interest to note that the failure mode changes from sliding failure mode to collapse failure mode with increasing column diameter.

5) The effect of the stress concentration ratio on the safety factors is relatively small, where the safety factors for the collapse and sliding failure modes increase slightly as long as the ratio is lower than about 5.

6) The current design method, slip circle analysis, provides reasonable agreement with the proposed design as long as the column strength is a relatively low value where the improved ground is expected to fail by shear failure mode. However, when the column strength increases where the improved ground is expected to fail by collapse failure mode, the current design method overestimates compared to the proposed method.

7) The effect ground consolidation due to embankment weight, underestimation of ground strength and effects of surface crust are investigated to determine if they could serve as an unwritten safety margin. According to the results, the surface crust

has a large effect on the stability. The failure mode changes from collapse failure mode to sliding failure mode when the strength of the crust is a relatively high value. The surface crust and the underestimation of ground strength can serve as a safety margin to compensate for the overestimation in the current design method.

Concluding remarks

Failure patterns of the column type DM improved ground were investigated by a series of centrifuge model tests, FEM analyses and simple calculations, in which the improved ground is subjected to embankment loading. The major conclusions derived in this study are described in each session summary. According to the research, the current design method might overestimate the external and internal stabilities, because failure patterns assumed are different from real behavior. The current design method, slip circle analysis, provides reasonable agreement with the proposed design as long as the column strength is a relatively low value where the improved ground is expected to fail by shear failure mode. However, when the column strength increases where the improved ground is expected to fail by collapse failure mode, the current design method overestimates compared to the proposed method. This paper demonstrates the importance of simulating the adequate failure modes in each failure pattern for evaluating the test results.

NOTATIONS

a_s : Improvement area ratio
D : Improvement width (m)
B : Diameter of DM column (m)
$c_{u,ave}$: Average undrained shear strength of DM columns and clay between (kN/m^2)
c_{u0} : undrained shear strength at ground surface (kN/m^2)
D : improvement width (m)
F_{rc} : Cohesive strength of clay along failure plane (kN/m^2)
F_{rf} : Shear strength of DM column along failure plane (kN/m^2)
F_{rt} : Shear strength of DM column (kN/m^2)
F_s : Safety factor
H_c : Thickness of clay ground (m)
H_e : Height of embankment (m)
H_t : Height of DM column (m)
k : Undrained shear strength increasing ratio with depth (kN/m^3)
M_{ac} : Driving moment by active earth pressure of clay ground (kN×m)
M_{ae} : Driving moment by active earth pressure of embankment (kN×m)
M_d : Driving moment (kN×m)
M_{rc} : Resistance moment by adhesion on side surface of DM columns (kN×m)

M_{rt} : Resistance moment by weight of DM columns (kN×m)
M_{re} : Resistance moment by weight of embankment on DM columns (kN×m)
M_{sc} : Resistance moment by shear strength of clay between DM columns (kN×m)
M_{pb} : Bending moment of DM column (kN×m)
M_{pc} : Resistance moment by passive earth pressure of clay ground (kN×m)
M_r : Resistance moment (kN×m)
n : Stress concentration ratio
N : Number of DM column rows
P_{ac} : Active earth pressure of clay ground (kN/m^2)
P_{ae} : Active earth pressure of embankment (kN/m^2)
P_{pc} : Passive earth pressure of clay ground (kN/m^2)
q_u : Unconfined compressive strength of DM column (kN/m^2)
S : spacing of DM column (m)

$$= \frac{B}{2} \cdot \sqrt{\frac{\pi}{a_s}}$$

z : Assumed depth of shear failure plane (m)
α : Bending strength ratio to unconfined compressive strength
γ_c : Unit weight of clay ground (kN/m^3)
γ_e : Unit weight of embankment (kN/m^3)
γ_t : Unit weight of DM column (kN/m^3)
ϕ_e : Internal friction angle of embankment (degree)
ϕ_s : Internal friction angle of sand layer (°)
μ_s : Stress concentration coefficient
σ_b : Bending strength (kN/m^2)
σ_v : Vertical stress (kN/m^2)

REFERENCES

1) Bauer, G.E., Scott, J.D. and Shields, D.H. (1973): The deformation properties of a clay crust, *Proc. of the 8th International Conference on Soil Mechanics and Foundation Engineering*, Vol. 1.1, pp. 31-38.
2) Broms, B.B. (2004): "Lime and lime/cement columns," Ground Improvement, 2nd edition, edited by M.P. Moseley and K. Kirsch, Spon Press, pp. 252-330.
3) Coastal Development Institute of Technology (2002): "The Deep Mixing Method - Principle, Design and Construction," A.A. Balkema Publishers, 123p.
4) Hashizume, H., Okochi, Y., Dong, J., Horii, N., Toyosawa,

Y. and Tamate, S. (1998): Study on the behavior of soft ground improved using deep mixing method, *Proc. of the International Conference on Centrifuge 98*, pp. 851-856.

5) Holm, G. (1999): Keynote lecture - Applications of dry mix methods for deep soil stabilization, *Proc. of the International Conference on Dry Mix Methods for Deep Soil Stabilization*, pp.3-13.

6) Japan Society of Civil Engineers (2002): Standard Specifications for Concrete Structures-2002, Method of test for flexural strength of concrete (JIS A 1106-1999), pp.291-294 (in Japanese).

7) Karastanev, D., Kitazume, M., Miyajima, S. and Ikeda, T. (1997): Bearing capacity of shallow foundation on column type DMM improved ground, *Proc. of the 14th International Conference on Soil Mechanics and Foundation Engineering*, Vol. 3, pp. 1621-1624.

8) Kawasaki, T., Niina, A., Saitoh, S., Suzuki, Y. and Honjyo, Y. (1981): Deep mixing method using cement hardening agent, *Proc. of the 10th International Conference on Soil Mechanics and Foundation Engineering*, Vol. 3, pp. 721-724.

9) Kitazume, M., Nakamura, T. and Terashi, M. (1991): Reliability of clay ground improved by the group column type DMM with high replacement, *Report of the Port and Harbour Research Institute*, Vol. 30, No. 2, pp. 305-326 (in Japanese).

10) Kitazume, M. and Maruyama, K. (2005): Collapse failure of group column type deep mixing improved ground under embankment, *Proc. of International Conference on Deep Mixing - Best Practice and Recent Advances*, Vol. 1.2, pp. 245-254.

11) Kitazume, M. and Maruyama, K. (2006): External Stability of Group Column Type Deep Mixing Improved Ground under Embankment Loading, *Soils and Foundations*, Vol. 46, No. 3, pp.323-340.

12) Kitazume, M. and Maruyama, K. (2007): Internal Stability of Group Column Type Deep Mixing Improved Ground under Embankment Loading, *Soils and Foundations*, Vol. 47, No. 3, pp.437-455.

13) Kitazume, M. and Miyajima, S. (1995): Development of PHRI Mark II geotechnical centrifuge, *Technical Note of the Port and Harbour Research Institute*, No. 817, 33p.

14) Kitazume, M., Ikeda, T., Miyajima, S. and Karastanev, D. (1996): Bearing capacity of improved ground with column type DMM, *Proc. of the 2nd International Conference on Ground Improvement Geosystems*, Vol. 1, pp. 503-508.

15) Kitazume, M., Yamamoto, M. and Udaka, Y. (1999): Vertical bearing capacity of column type DMM ground with low improvement ratio, *Proc. of the International Conference on Dry Mix Methods for Deep Soil Stabilization*, pp. 245-250.

16) Kitazume, M., Okano, K. and Miyajima, S. (2000): Centrifuge model tests on failure envelope of column type DMM improved ground, *Soils and Foundations*, Vol. 40, No. 4, pp. 43-55.

17) Kivelo, M. (1998): Stabilization of embankments on soft soil with lime/cement columns, *Ph.D. Thesis, Royal Institute of Technology*, Sweden, 170p.

18) Miyake, M., Akamoto, H. and Wada, M. (1991): Deformation characteristics of ground improved by a group of treated soil, *Proc. of the International Conference on Centrifuge 1991*, pp. 295-302.

19) Nakase, A., Kimura, T., Saitoh, K., Takemura, J. and Hagiwara, T. (1987): Behaviour of soft clay with a surface crust, *Proc. of the 8th Asian Regional Conference on Soil Mechanics and Foundation Engineering*, Vol. 1, pp. 401-404.

20) Public Work Research Center (2004): Design and construction manual on deep mixing method for inland construction, 326p. (in Japanese).

21) Rathmayer, H. (1996): Deep mixing method for soft subsoil improvement in the Nordic countries, Grouting and Deep Mixing. *Proc. of the 2nd International Conference on Ground Improvement Geosystems*, 2: 869-877. Balkema.

22) Terashi, M., Tanaka, H. and Okumura, T. (1979): Engineering properties of lime-treated marine soils and deep mixing method, *Proc. of the 6th Asian Regional Conference on Soil Mechanics and Foundation Engineering*, pp. 191-194.

23) Terashi, M., Tanaka, H., Mitsumoto, T., Niidome, Y. and Honma, S. (1980): Fundamental properties of lime- and cement-treated soils (2nd Report), *Report of the Port and Harbour Research Institute*, Vol. 19, No. 1, pp. 33-62 (in Japanese).

24) Terashi, M. and Tanaka, H. (1983): Bearing capacity and consolidation of ground improved by a group of treated soil columns, *Report of the Port and Harbour Research Institute*, Vol. 22, No. 2, pp. 213-266 (in Japanese).

25) Watabe, Y. and Tsuchida, T. (2001): Comparative study on undrained shear strength of Osaka bay pleistocene clay determined by several kinds of laboratory tests, *Soils and Foundations*, Vol. 41, No. 5, pp.47-59.